AMERICAN UNIVERSITY OF BEIRUT

FINITE ELEMENT SIMULATION OF ULTRASONIC AND BOREHOLE ACOUSTIC MEASUREMENTS OF FRACTURED AND ANISOTROPIC RESERVOIRS

by
HAWRAA MAHMOUD KAREEM

A thesis
submitted in partial fulfillment of the requirements
for the degree of Master of Engineering
to the Baha and Walid Bassatne Department of
Chemical Engineering and Advanced Energy
of the Maroun Semaan Faculty of Engineering and Architecture
at the American University of Beirut

Beirut, Lebanon
February 2021

AMERICAN UNIVERSITY OF BEIRUT

FINITE ELEMENT SIMULATION OF ULTRASONIC AND BOREHOLE ACOUSTIC MEASUREMENTS OF FRACTURED AND ANISOTROPIC RESERVOIRS

by

HAWRAA MAHMOUD KAREEM

Approved by:

Maalouf, Elsa, PhD; University of Texas at Austin; Assistant Professor; Advisor
B.W. Bassatne Department of Chemical Engineering and Advanced Energy

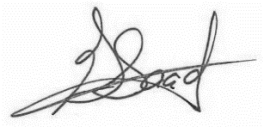

Saad, George, PhD; University of Southern California; Associate Professor;
Member of Committee
Civil and Environmental Engineering

Dr. Elsa Maalouf on behlaf of Dr. Kassem Ghorayeb 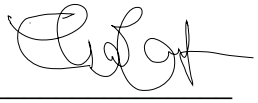

Ghorayeb, Kassem, PhD; Paul Sabatier University; Assistant Professor
Member of Committee
B.W. Bassatne Department of Chemical Engineering and Advanced Energy

Date of thesis defense: [February 18, 2021]

AMERICAN UNIVERSITY OF BEIRUT

THESIS RELEASE FORM

Student Name:	Kareem	Hawraa	Mahmoud
	Last	First	Middle

I authorize the American University of Beirut, to: (a) reproduce hard or electronic copies of my thesis; (b) include such copies in the archives and digital repositories of the University; and (c) make freely available such copies to third parties for research or educational purposes:

- ☐ As of the date of submission
- ☒ One year from the date of submission of my thesis.
- ☐ Two years from the date of submission of my thesis.
- ☐ Three years from the date of submission of my thesis.

Signature 08.04.2021

ACKNOWLEDGEMENTS

I would like to express my deepest appreciation for my advisor Dr. Elsa Maalouf who supported me along the whole journey. Without her guidance and persistent help, this work would not have been possible. I am extremely grateful and indebted for her expert, sincere and valuable encouragement extended to me.

I would like to thank my committee members, Dr. George Saad and Dr. Kassem Ghorayeb for their support and constructive feedback.

I would also like to extend my deepest gratitude to my engineer friends, Mahmoud Khadijeh, Mohammad Abdo and Mohammad Al Husseini for the support and help.

A special thanks to the IT department at AUB for their technical support.

Finally, I would also like to express my extreme sincere gratitude to my family, friends and beloved ones for their continuous support.

I acknowledge the financial support.

ABSTRACT
OF THE THESIS OF

Hawraa Mahmoud Kareem for Master of Engineering
Major: Chemical and Petroleum Engineering

Title: Finite Element Simulation of Ultrasonic and Borehole Acoustic Measurements of Fractured and Anisotropic Reservoirs

Unconventional shale rocks are characterized by low porosity and low permeability that impacts the flow of fluids and the production of gas form these reservoirs. The presence of natural fractures in shale formations enhances the reservoir conditions for developing large-scale fracture networks during hydraulic fracturing, which represents a key factor for shale gas development. Therefore, accurate identification of natural fractures in shale reservoirs improves reservoir stimulation and production.

The estimation of fractures density is usually obtained by first measuring the elastic properties of reservoir rocks using ultrasonic measurements on cores (small scale). When the number of cores is limited or cores are not available, the elastic properties are obtained using borehole acoustic measurements (sonic well logs) which are available continuously in a well (large scale). The measured elastic properties of the rock are then used to estimate the crack (fracture) density using effective medium theories (EMT).

The aim of this thesis is to determine the range of applicability of different EMT models to estimate the elastic properties of fractured shale formations using the finite element method (FEM). The Barnet shale formation properties are used in the modeling. The shale rock includes equidistant horizontal fractures modeled as ellipsoids and approximated as octahedrons. The fractures are either dry or filled with a calcite or a weak material, have an aspect ratio of 0.1 and a volume concentration that varies from 1% to 8% equivalent to a crack density up to 30%. The elastic properties of the rock are calculated using ultrasonic measurements and are compared with three effective medium models: the Hudson 1st and 2nd orders, the self-consistent approximation (SCA) and the differential effective medium theory (DEM).

Ultrasonic results show that octahedrons can be used to approximate the ellipsoids with a relative error below 4% and that using octahedrons enhances the performance of FEM simulations by 40%. The comparison of the elastic properties of the Barnet shale measured using the FEM and calculated using the EMT show that the difference increases as the volumetric concentration of cracks increases. Moreover, the calculated

elastic properties of the Barnet shale with cracks filled with calcite are better approximated by the SCA and DEM models compared to the Hudson model while the dry or weak cracks are better approximated by the Hudson and SCA models.

In the last chapter, we describe a model to obtain sonic logs of a fractured formation measured by an acoustic tool in a fluid filled borehole, which can be used to correlate ultrasonic and borehole measurements.

TABLE OF CONTENTS

ILLUSTRATIONS

Figure

TABLES

Table

CHAPTER I

INTRODUCTION

Reservoir rocks are classified as conventional and unconventional and are characterized by their ability to store fluids (hydrocarbon pore volume) and potential for the fluids to flow (permeability). In a conventional reservoir, the geological formation is porous and permeable and the hydrocarbons (oil and gas) deposits have a well-defined areal extent. These factors facilitate production and eliminate the need of extensive well stimulation processes to enhance production. However, in an unconventional reservoir, the fluid flow and hydrocarbon production are impacted by the low porosity and low permeability of the formation. In such formations, the oil and gas deposits are very diverse, difficult to characterize and dispersed over large areas. In an unconventional reservoir additional extraction or conversion technology such as well stimulation (i.e., hydraulic fracturing) are needed for the production to be economical (J. Gale, 2014).

Today, most of the easy-to-drill, conventional reservoirs are depleted. Therefore, a majority of hydrocarbon production in the US is obtained from shale unconventional reservoirs. The most common method used to enhance production from unconventional reservoir is to couple horizontal drilling with hydraulic fracturing (Fink, 2020).

A deep-well injection of a fracturing fluid is used in hydraulic fracturing by which the release and collection of natural gas from unconventional shale plays is facilitated. The process of fracking involves drilling a well and pumping a fracturing fluid with a specific chemical composition (a mixture of water, proppants such as sand and other additives) under high pressure into the formation (Figure 1 (a)) (Smith & Montgomery, 2015). The reservoir begins to fracture once it is fully saturated and

cannot absorb more fluid. The induced fractures increase the reservoir permeability by creating conductive pathways for the hydrocarbons to flow toward the wellbore as shown in Figure 1(b). The proppants are added to keep the fractures open so that the hydrocarbon fluids are recovered and the proppants remain in the well.

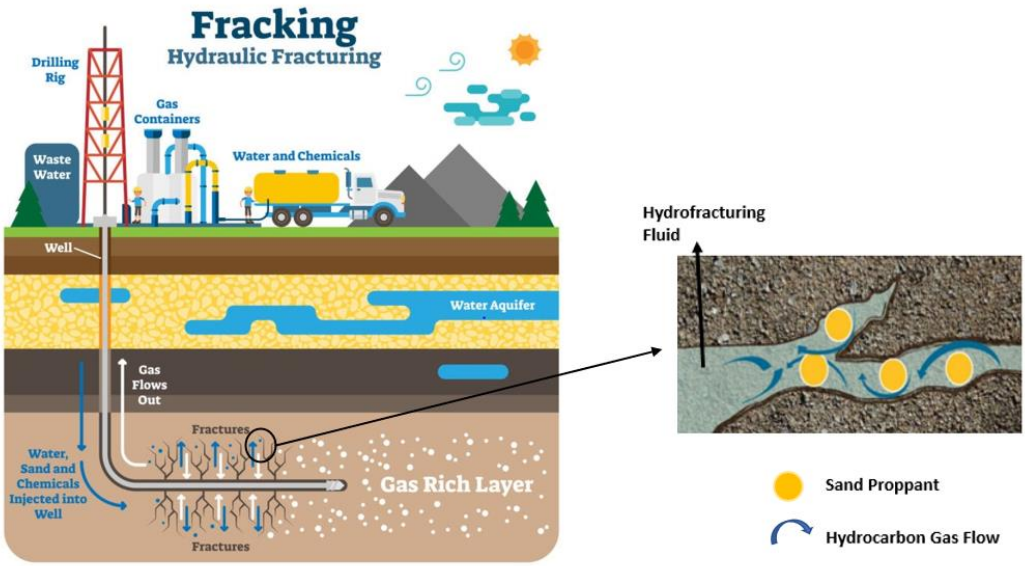

(a) **(b)**

Figure 1 Illustration of (a) hydraulic fracturing for unconventional reservoirs and (b) hydrocarbon gas flow through induced fractures (OILMAN, 2018)

A. Role of Natural Fractures – Motivation

In addition to the induced fractures, most shales include natural fractures (J. Gale, 2014). The presence of natural fractures in geological formations influences both the formation mechanical and hydraulic properties (Sarout, Cazes, Delle Piane, Arena, & Esteban, 2017). Natural fractures greatly affect the rock stiffness and provides space for fluid accumulation and migration. Moreover, natural fractures enhance the reservoir conditions for developing large-scale fracture networks during hydraulic fracturing, which represents a key factor for shale gas development and exploration (J. F. Gale,

Reed, & Holder, 2007). For example, shale layers that include horizontal fractures provide the storage space for free gas which could be the sweet spot for shale gas hydraulic fracturing (Liu, Yao, Liu, & Elsworth, 2017). The detection and prediction of natural fractures is therefore essential for oil and gas exploration and production (Pérez, Grechka, & Michelena, 1999) but also for earthquake prediction (Crampin & Zatsepin, 1997), CO2 sequestration (Crampin & Zatsepin, 1997) , mining engineering (Grenon & Hadjigeorgiou, 2012), underground waste storage, water resource management and seismology (Ding, Wang, Di, & Li, 2019).

B. Natural Fractures Detection Using Effective Medium Theories (EMT)

Detecting and characterizing natural fractures is critical to guarantee safe drilling and production, and to better develop and optimize hydraulic fractures operations in unconventional shale formations (A. Li et al., 2020). Fractures are characterized by spatial distribution, geometrical properties (aspect ratio and shape), crack density, volumetric concentration and fluid saturation. These characteristics yield an effective value for the elastic properties of the rock.

One method to determine the crack density of a naturally fractured reservoir is to compare measured elastic properties of the fractured rocks to estimated values obtained using effective medium theories (EMT) models. The EMT of cracked solids are applicable to different material science problems, where a cracked solid is represented as a homogeneous material with effective elastic properties and effective density. Figure 2 shows that a heterogenous cracked medium composed of a background material defined by $\boldsymbol{V_{p1}, V_{s1}, \rho_1}$ embedded with cracks defined by $\boldsymbol{V_{p2}, V_{s2}, \rho_2}$ is approximated as a homogenous medium defined using effective

properties V_p, V_s, ρ after applying the EMT on the elastic properties of the heterogenous medium**.** The estimation of crack density using EMT is achieved by matching the measured elastic properties of the fractured reservoir with the effective medium theories (EMT) estimations.

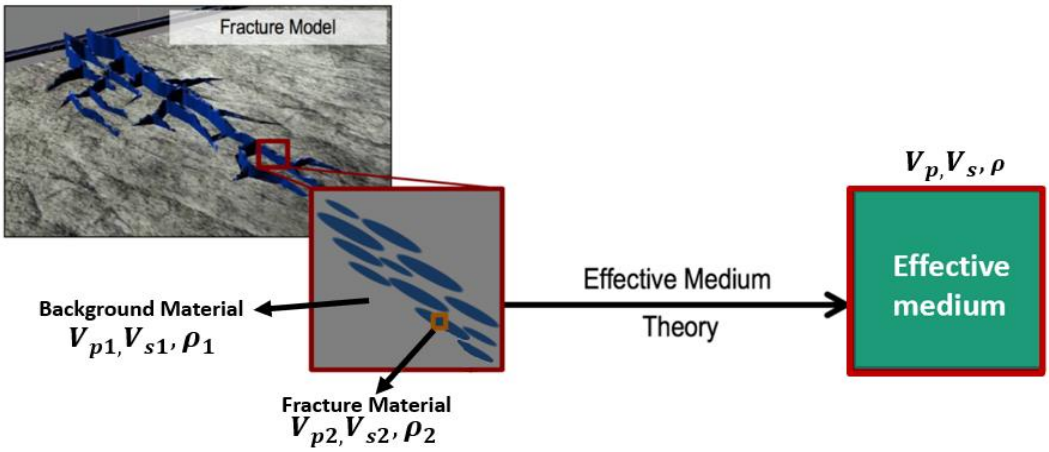

Figure 2 Effective medium theory. The fracture model illustration is taken from Heagy (2018)

The effective elastic properties of fractured formations are measured using two dynamic procedures: Ultrasonic measurement on cores and acoustic borehole measurement (sonic logs). The EMT models depend on the value of crack density. Therefore, when material properties of the rock matrix and inclusions are known and the crack aspect ratio is assumed from SEM images, minimization models (inversion techniques) are applied to determine the value of crack density that provide the best fit between the EMT and the measured effective elastic properties.

C. Problem Statement

EMT are straightforward and easy to use for the characterization of fractures. However, EMT include assumptions regarding the crack geometry, crack-crack interaction and the wave propagation. All EMT assume idealized crack shapes (e.g., ellipsoids inclusions) where cracks are isolated with respect to fluid flow. Commonly used EMT theories are idealistic and cannot always be used to accurately represent individual elements of complex formations such as organic vertical transversely isotropic (VTI) shales.

The main objective of this work is to evaluate the accuracy of EMT for different fracture characteristic using finite element simulations of core ultrasonic measurements. The EMT assumed are the Hudson 1^{st} and 2^{nd} orders, the self-consistent approximation (SCA) and the differential effective medium theory (DEM).

D. Thesis Objective

The aim of this work is to determine the accuracy of different EMT models in estimating the elastic properties of fractured VTI Barnet shale formations acquired using accurate FEM ultrasonic models.

The prediction accuracy of each EMT model is estimated by determining the crack density (or volume concentration) threshold at which the estimation of elastic properties using EMT is no longer valid. Among the different methods that estimate the effective properties for fractured rock, the following commonly used EMT models are considered in this work:

- Hudson's 1^{st} and 2^{nd} models.
- Self-consistent approximation (SCA).

- Differential effective medium (DEM).

The assumed rock is a VTI Barnet shale core with horizontally aligned ellipsoidal cracks that are homogenously distributed throughout the core. The inclusions are assumed to be dry, weak or calcite filled. Natural calcite filled fractures present in Barnett shales act as planes of weakness that can reactivate during hydraulic fracturing by opening up to fracturing fluids and providing a network of fractures connected to the wellbore. Studying calcite filled fractures is very important since their presence enhances the permeability of fractured reservoirs and allows for optimal stimulation conditions.

In the FEM, the cracks are approximated as octahedrons to decrease the simulation time and optimize the meshing procedure for FEM simulations. Results show that the model accurately estimate the wave propagation obtained from dynamic ultrasonic measurements acquired at high frequencies.

The advantage of using numerical simulation compared to experimental work is the following:

- Selection of any geophysical model and material properties.
- Testing multiple cases of inclusion shape and distributions.
- Testing different values of rock aspect ratio and crack density.
- Using small crack aspect ratio.
- Precise results by suppressing the effect of noise and reflections at the boundaries.
- Studying the effect of the following properties: aspect ratio of inclusions, central frequency, crack density, background and inclusion material properties, distance

between cracks for the same crack density, fracture inclination angle, spatial distribution of inclusions, inclusions shape and intersection of fractures.

- Used to validate experimental work.
- These models can be used in future work for quantitative core analysis and logging interpretation as they are helpful tools for reservoir characterization.

This thesis also introduces effective well logging numerical models used to measure the elastic properties of fractured formations and that can be used to calibrate the ultrasonic measured data.

E. Thesis Outline

This thesis is divided into five chapters. Chapter 1 presents the scope of work, the motivation and objectives.

In Chapter 2, a literature review is conducted on the Barnet shale formations to describe the elastic properties and the fracture network. Dynamic acquisition models (core analysis and well logging) used to estimate elastic properties are presented. Then, the EMT models (theory, applications and limitations) are presented with previous numerical and experimental work that are used to evaluate the accuracy and application conditions of EMT models.

In Chapter 3, the methodology used to perform the high frequency ultrasonic numerical models is presented along with the input parameters and processing technique. The EMT mathematical equations are presented and the calculation of the RMS errors needed to select the EMT method that best fits with numerical estimations is also shown. The model aims to provide a link between the rock properties (porosity,

lithology and fluid saturation) and the elastic attributes (velocities for VTI Barnet shale formations).

Chapter 4 is divided into two sections:

- In section 1, the ultrasonic numerical examples along with results are presented and discussed.
- In section 2, we introduce well logging numerical models as alternative to ultrasonic models used to measure the elastic properties.

Core analysis represents the high frequency ultrasonic models and well logging represent the low frequency sonic log models.

CHAPTER II

LITERATURE REVIEW

A. Shale Formations

Organic shale formations are source rocks that have the tendency to generate hydrocarbons. Examples of shale formations include Barnet, Marcellus, Vaca Muerta, Baxter and New Albany. Unconventional shale is composed of various minerals including quartz, clays, calcite, dolomite and contains kerogen (J. F. Gale, Laubach, Olson, Eichhubl, & Fall, 2014). Moreover, they contain natural fractures (cracks) and pores that are saturated with hydrocarbon or water (Figure 3 (a)). In case clays and kerogen are laminated and the cracks are horizontally distributed, the shale formation is then modeled as a vertical transverse isotropic (VTI) formation (Figure 3 (b)).

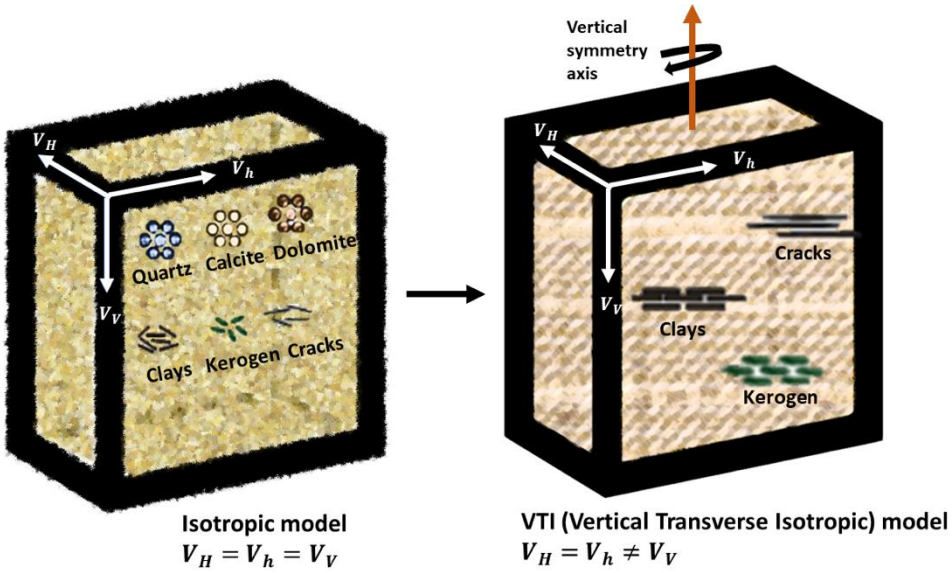

(a) **(b)**

Figure 3 VTI shale formation

A VTI rock has a vertical axis of rotational symmetry; i.e., the elastic properties of the rock are considered uniform within a horizontal layer but vary vertically from one layer to the other.

B. Natural Fractures in Shale Formations

1. Fractures' Type (Structural vs. Nonstructural)

Natural fractures in shale formations are categorized as structural and nonstructural fractures (Figure 4). Structural fractures include regional high-angle shear, torsional, extensional and low-angle slip fractures, while nonstructural fractures include bedding, dissolution and diagenetic contraction fractures. Some structural shear fractures are filled with minerals and have relatively large openings. High-angle torsional fractures are usually filled with quartz and calcite. The most nonstructural fractures in shales are bedding fractures that are rarely filled with minerals (A. Li et al., 2020).

(a) **(b)** **(c)** **(d)** **(e)** **(f)**

Figure 4 (a) Unfilled bedding fractures, (b) filled bedding fractures and (c) dissolution fractures are examples of nonstructural fractures and (d) high-angle shear fracture, (e)

high-angle extensional fracture and (f) high-angle torsional fracture are examples of structural fractures in shale cores (Grenon & Hadjigeorgiou, 2012)

2. Fractures' Infill Material (Open vs. Sealed)

J. F. Gale et al. (2007)studied four Barnett shale fractured cores and showed that fractures have a narrow opening size (< 0.05 mm), sealed with calcite and distributed in echelon arrays (Figure 5) (J. F. Gale et al., 2007).

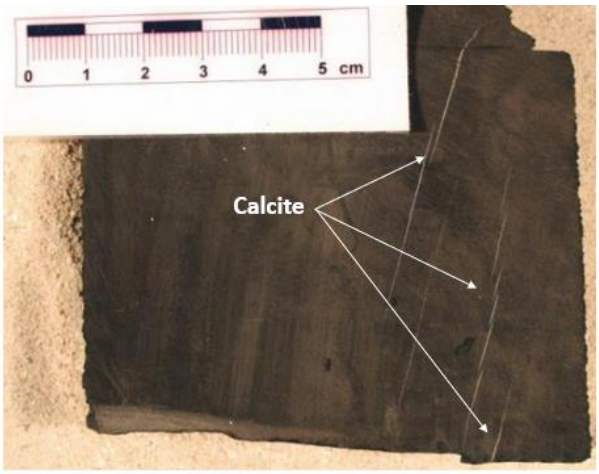

Figure 5 Echelon fractures in a Barnet shale Core (J. F. Gale et al., 2007)

Few wide fractures may be open when the fracture population follows a power law size distribution (J. F. Gale et al., 2007). A distribution of sealed and open bedding parallel fractures in different shale plays is shown in Figure 6 (J. Gale, 2014).

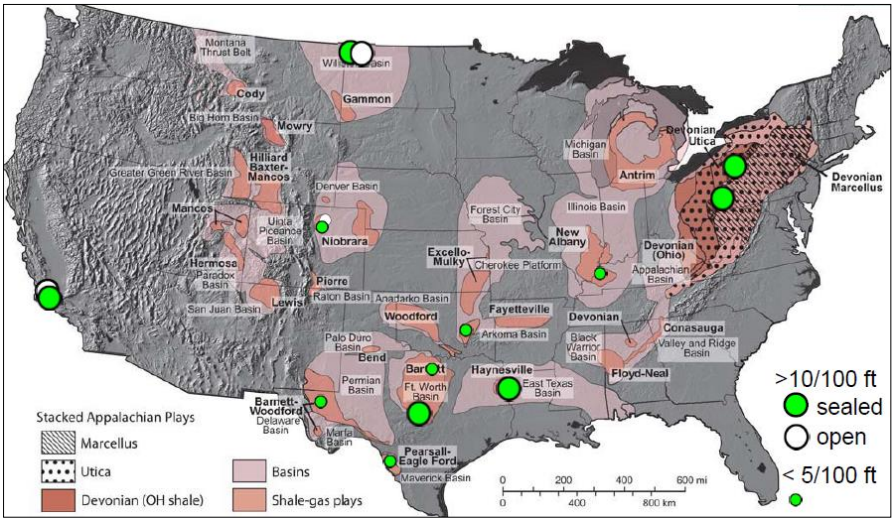

Figure 6 Open and sealed bedding fractures distribution in different shale formations in the Horn River and Neuquen Basins (J. Gale, 2014)

J. F. Gale et al. (2014) showed that for an Austin chalk shale outcrop scanline, only the largest fractures with a kinematic aperture > 11 mm are open. They also related the cumulative frequency and average spacing of fractures to the kinematic aperture and stated that similar large fractures in widely spaced clusters may be present in the Barnett Shale.

Figure 7 highlights the presence of calcite infill in Barnett shale located in narrow sealed fractures, while large open fractures obtained from large cluster are also shown.

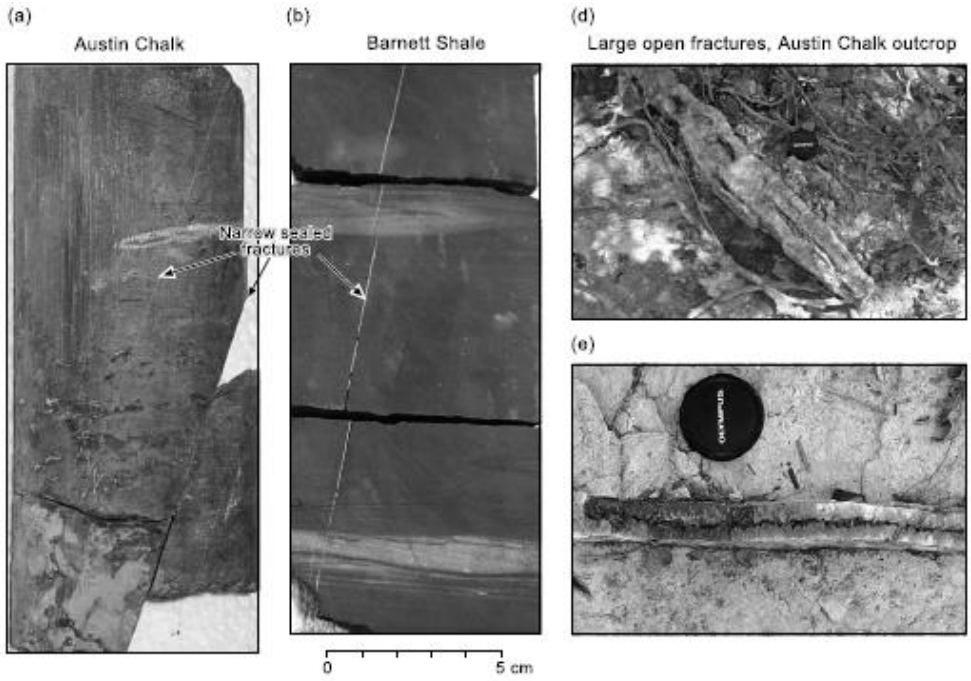

Figure 7 (a, b) Similarities between fractures in Austin Chalk and Barnett Shale (image from (Papazis, 2005)). (d, e) Open fractures from the large fracture cluster (J. F. Gale et al., 2007)

Julia et al. (2017) showed that the narrow fractures in four Barnet shale cores are all sealed, thus they cannot enhance the permeability nor contribute to reservoir storage (J. F. Gale et al., 2007). However, narrow sealed fractures are advantageous because they can reactivate during hydraulic fracture treatments. Large open fractures exist in clusters that are separated by several hundred feet and play a major role in enhancing the permeability locally through conducting the hydraulic fracturing fluid by great distances, but they might cause problems during hydraulic fracturing treatment represented by possible aseismically propagation of cracks (J. Gale, 2014).

3. Fractures' Distribution

In a shale formation, fractures are either aligned or randomly distributed (J. F. Gale et al., 2007). Aligned fractures that result in a vertical transverse isotropic medium (VTI) are expected because of the strong discrepancy in stress vectors. However, randomly distributed fractures might also exist. A random distribution results in zero anisotropy and the overall formation is considered as isotropic rock.

4. Fractures' Quantification

The quantification of fractures in rocks is either quantitative by measuring the intensity (frequency) of fractures or semi-quantitative by measuring the abundance of fractures. Fracture intensity is the number of fractures per unit length, area or volume and is acquired over a large sample relative to fracture size. Fracture clustering and sampling limitation in the subsurface makes it challenging to quantify fracture intensity. When fracture intensity is not available, fractures are quantified by measuring the fracture abundance. Fracture abundance is the number of fractures (N) per 100 ft of a vertical core and includes all fractures that have a length larger than 30 μm. Three fracture abundance categories are determined: many (N>10 per 100 ft), several (N:5-10 per 100 ft) or few (N<5 per 100 ft) (J. Gale, 2014).

5. Core Sampling

Fracture quantification depends on the origin of cores, i.e., on the well location and the layer from which the core was extracted. Cores might be taken from layers that are either rich or poor in fractures. Thus, core analysis must be interpreted with care since the extracted cores might represent a small fraction of the formation where large

fractures are not observed and small micro-fractures are induced by drilling, core removal or handling processes (J. F. Gale et al., 2007).

6. Fractures' Dimensions and Aspect Ratio

J. F. Gale et al. (2014) performed an analysis on different fractured cores taken from Woodford, Barnett, Marcellus, Baxter, New Albany and Austin Chalk formations. The number of fracture inclusions varied between 1 and 100 depending on the size of the core and on the inclusions' kinematic aperture that varies from 0.03 mm to 100 mm. Fracture kinematic aperture is measured orthogonal to the fracture walls and includes cement and opening. Fracture height varied between a few mm up to 600 cm. J. F. Gale et al. (2014) showed that for a Barnet shale core with 50 fractures, the aspect ratio (width/length) of fractures varies between 0.00025 and 0.0005 (Z. Guo & Li, 2015). The examination of a 33.5 m core extracted from T.P.Sims well for a Barnet shale formation shows that there exist 1 set of 74 sealed fractures with a kinematic aperture that varies between 0.05 mm and 0.265 mm resulting in a maximum aspect ratio of 0.0003 (J. F. Gale et al., 2007). Barnett shale tight formations are characterized by a low porosity of 5% to 6% with an average water saturation of 25% (Boak & Kleinberg, 2020).

C. Hydraulic Fracturing and Induced Fractures in Shale Formations

1. Hydraulic Fracturing: Definition

Hydraulic fracturing is a reservoir stimulation method that was first applied in 1947 on a vertical well in the Hugoton field, Kansas by inducing a simple two-wing fracture to improve gas production (Fink, 2020).

Hydraulic fracturing of a tight reservoir enhances its permeability by inducing a network of highly conductive fractures in the area surrounding the stimulated wellbore (Economides & Nolte, 1989). Hydraulic fracturing enhances not only the conductivity and permeability of the reservoir, but also increases the surface area charged for hydrocarbon production. This technique is used to boost both conventional and nonconventional reservoirs and can be applied for vertical and horizontal wells.

An advanced technique known as multistage fracturing is used in horizontal wells to increase the hydrocarbon productivity (Figure 8). Multistage fracturing allows the placement of fractures at specific places within the horizontal borehole. A perforated pipe gun is sent to the drilled section and explosives are then fired from the gun through the perforations and into the shale to create fractures. The fracturing fluid is pumped into the fractures (Figure 8 (a)) to crack and expand them for the hydrocarbon to be extracted more easily. The most common fluids used in traditional hydraulic fracturing processes are linear or crosslinked guars. These fluids are pumped at high pressure into the wellbore and are used to open or propagate fractures. Proppants are transported to the fractures by the mean of fracturing fluids so that a thin layer is formed between the different fracture faces to keep the induced fractures open when the hydraulic fracturing process is terminated. The fluid is then pumped out and the fracturing gun is moved in reverse down the wellbore. An isolation plug is used in between stages to activate the target area and separate it from the area below it that has been previously fractured. The fracturing and plugging processes are repeated along the entire length of the wellbore to maximize potential hydrocarbon extraction efficiency. At the end of the fracturing process, the polymers present in between the fractures are broken by using chemical breakers (diverters) so that highly conductive fractures are provided. After completed

all the fractures, the plugs are drilled out and the hydrocarbon is able to flow (Figure 8 (b)). The hydrocarbon is pumped up the wellbore to the surface facility for extraction and processing (Barati & Liang, 2014).

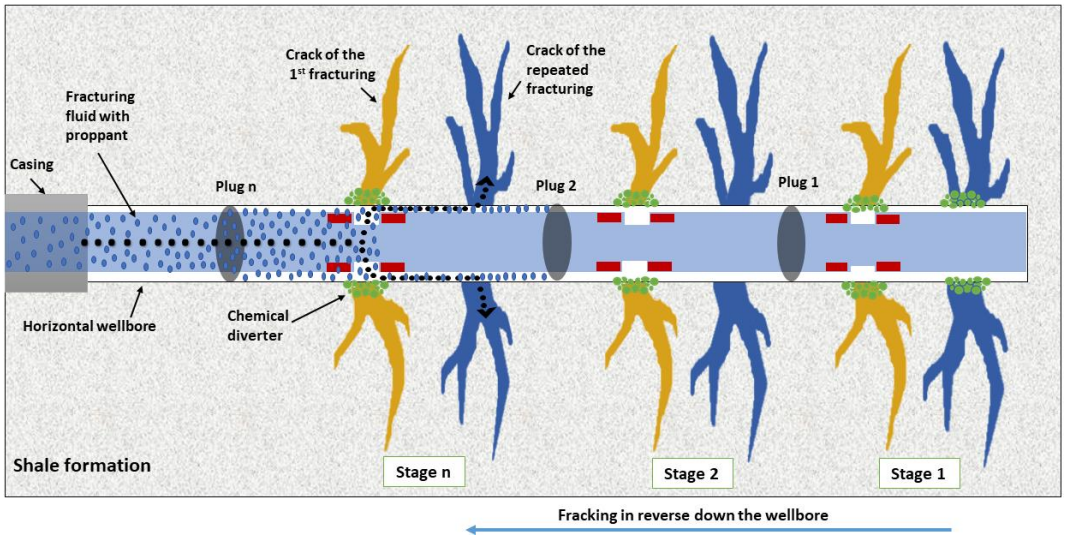

(a)

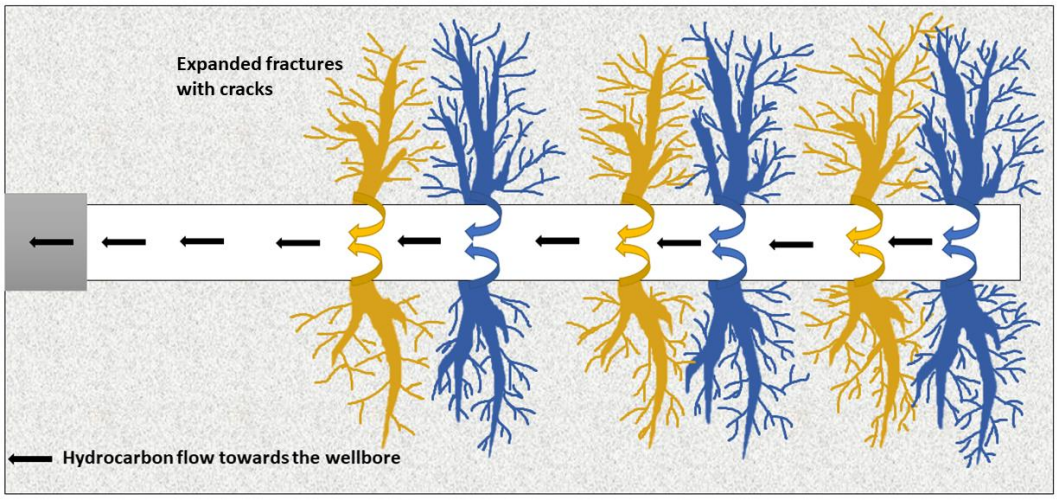

(b)

Figure 8 (a) Illustration of multistage fracturing in a horizontal well followed by (b) hydrocarbon flow from the highly fractured network

This increases the ability of the oil and gas industry to have economical and feasible drilling processes in such unconventional tight shale reservoirs. As a result the hydrocarbon cumulative production is increased in a shorter time frame (Economides & Nolte, 1989).

2. Effect of Open and Calcite Filled Fractures on Hydraulic Fracturing Operations

The effect of fractures on hydraulic fracturing, permeability, and production depends on whether the fractures are open or sealed. In many reservoirs, the propagation of hydraulic fractures is blocked once a natural open fracture is encountered (NR Warpinski & Teufel, 1987). However, for the Barnett shale natural fractures support hydraulic fracturing propagation which improves the producibility of the reservoirs (Norman Warpinski, Kramm, Heinze, & Waltman, 2005). Microseismic monitoring has shown that natural fractures in the Barnett shale formation have the tendency to reactivate during hydraulic fracturing by opening and producing a complex network of fractures (Fisher et al., 2004). Natural fractures in Barnett shales are not a barrier during hydraulic fracturing because of the low tensile strength at the contact between the shale wall rock and the calcite fracture fill. This low tensile strength is due to the absence of crystallographic continuity between the calcite cement grains and the wall rock grains. Therefore, crystal bonds do not exist between the calcite cement and the wall rock (J. F. Gale et al., 2007) which contrasts with quartz cement fill in fractures of tight-gas sandstones (A. Li et al., 2020). Thus, calcite cement grains are not embedded within the fracture wall grains and act as planes of weakness that are activated during hydraulic fracturing operations (J. F. Gale et al., 2007).

Figure 7 and Figure 9 show failure of the core at the weak boundaries of the shale. Although the failure is caused by core-handling damage, the same failure is expected to occur during a hydraulic fracture treatment because of the elevated fluid pressures used.

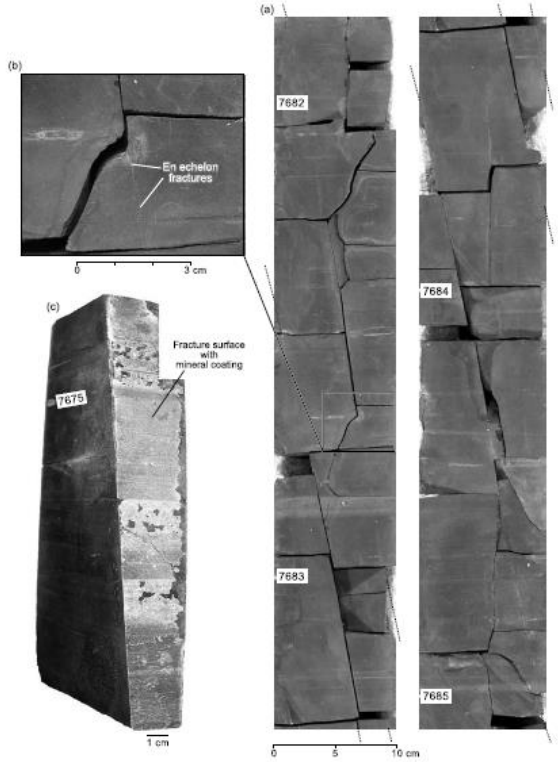

Figure 9 Natural fractures in the T. P. Sims core sealed with calcite and arranged in an echelon arrays at (a) meter and (b) centimeter scales. (c) Broken fracture surface showing calcite mineralization. The numbers on the core are depths in feet (A. Li et al., 2020)

Natural fractures that encounter induced hydraulic fractures are reactive to fracturing fluids and provide a network of fractures connected to the wellbore leading to an optimal stimulation of the well. Therefore, horizontal fractures exploration and detecting the natural fracture system in shale reservoirs is very important since they can

provide a storage space for free gas and they represent sweet spot for shale gas hydraulic fracturing (Liu et al., 2017).

D. Fracture Detection Methods: Acquisition, Inversion and Inference

Fractures are abundant in the subsurface and represent regions of anomalous physical properties. Fractures induce some anisotropy in the physical and elastic properties of the formation rock. This anisotropy represents an important feature for fracture detection using effective elastic properties.

1. Scales of Fracture Detection Methods: Acquisition Step

Fracture detection is usually done remotely through different geophysical fracture detection methods that are classified into three different scales (Council, 1996):

- First scale: large scales including surface soundings.
- Second scale: intermediate scales including borehole-to-borehole and surface-to-borehole soundings.
- Third scale: small scales associated with measurements made on rocks immediately adjacent to a borehole or tunnel.

Fracture detection methods ranges from simple outcrop analogs to more advanced and sophisticated seismic and electromagnetic soundings (Council, 1996).

- Outcrop analysis is based on a simple extrapolation of surface observations. Such methods take into consideration multiple parameters such as fracture timing relative to burial, stress history, diagenesis of host rock, fracture cementation, lithology comparison with the subsurface and distance of outcrops

from the reservoir. Outcrop analogs have a poor ability to detect fractures in the interwell volume but may add supporting information (J. Gale, 2014).

- Seismic and electromagnetic soundings methods include the following (Council, 1996):
  - Surface methods: seismic reflection (e.g., Analysis of P and S waves).
  - Electrical and Electromagnetic methods (e.g., Ground penetration radar, Tiltmeters and Geological observations).
  - Borehole reflection methods **(**e.g., Cross-Hole seismic reflection, Coupled inversion of transmission and reflection data).
  - Single hole methods (e.g., Core inspection, Conventional well logs and Borehole imaging logs).
  - Acoustic waveforms logging methods.
  - High resolution flowmeter methods.
  - Fluid flow monitoring using geophysical methods.

2. Selection of the Best Fracture Detection Method: Acquisition Step

Methods that have a high depth of investigation into the subsurface (e.g., well logging) cannot provide a full analysis and determination of fractures locations and distributions, while methods with shorter ranges (e.g., core analysis) provide better resolutions (Sarout et al., 2017).

The usefulness of each method depends on the distance from which the fractures are to be detected.

- For great detection distance, seismic methods that rely on shear waves splitting are used.

- For moderate detection distance, directional borehole methods are used.
- For detection within the borehole, scanned methods including formation micro scanner (FMS) and the televiewer methods are used.
- For actual flow characterization within a fractured rock system, methods such as high-resolution flowmeter and radar difference tomography are used.

3. Inversion and Inference Methodologies of the Acquired Data

The objective from these multiple geophysical fracture detection methods (listed in section D) is to detect and characterize fractures (Council, 1996).

- Fracture physical properties of interest include fracture's size and aspect ratio, shape, density, volumetric concentration, orientation, fluid and mineral content.
- The raw data acquired in the form of voltage (displacement or travel time) from any detection method is processed into a form appropriate to use in inversion techniques so that elastic rock properties including seismic, ultrasonic and well logging effective velocities of the rock can be estimated.
- The inversion technique relies on oversimplified theories that are sometimes computationally intensive. However, the validity, resolution, and uniqueness of such methods are well studied. Examples of post processing techniques include: First arrival detection for ultrasonic measurements, Slowness-Time Coherence (STC) and Matrix pencil processing techniques for well logs measurements.
- However, inference of fracture parameters (including single fracture characteristic such as the fracture size or even lumped parameters such as the crack density) form the inverted rock properties is negotiable and opened to

large debates. The term inference is used to emphasize that it is less reliable than inversion.

- This inference (deduction) of fracture parameters is usually guided by different theories such as the effective medium theories (EMT) that may rely on strong assumptions and idealizations of different fracture parameters such as fracture geometry. Even though in cases where the inversion is correct, it still has uncertainty with respect to fluid flow for example. Few deduction methods (e.g., dual porosity method) can provide a direct interpretation of the inferred fracture characteristics in terms of fracture flow. The interpretation is less accurate from both inference and inversion.

4. Optimization of Inference Techniques

A major development has been done regarding acquisition and inversion techniques applied to measure the effective elastic properties of the rock. Progress is still needed in the inference process to better estimate fracture properties from the measured properties. Suggestions to optimize the inference technique include the following (Council, 1996):

- The deduction method must heavily rely on supportable assumptions and avoid unsupportable ones.
- Different inference methods that estimate different fractures lumped parameters can be combined to constrain fracture properties.
- More data must be processed in the inversion step. Examples include processing the entire signal of seismic data and not just the first breaks in addition to

performing better experiments using broader-band sources and downhole sources.

- Perform more work to study the accuracy of the theories used during the deduction process.
- The need to better learn how to deduce the elastic properties and how to interpret the hydraulic properties (e.g., rock permeability) from the inferred fracture parameters.

E. Acquisition Techniques: Well Logging vs. Core Analysis

The elastic properties of a reservoir rock are acquired using well logging and core analysis.

1. Well Logging

Well logs have been used extensively since 1957 to measure the petrophysical properties of formations. Sonic logs in conjunction with other acquisition techniques represent the basic tools to examine the mechanical integrity of reservoir rocks and formations that surround them (Thomas W. Engler).

a. Sonic Logs

In petroleum industry, a well is drilled in a formation and a logging tool is inserted in the drilled well (borehole) (Figure 10 (a)). The acoustic tool operates by sending a sound pulse from a transmitter. The wave travels through the fluid (mud) in the borehole and the surrounding solid formation and is detected receivers at the tool. Figure 10 (b) shows the different trajectories of the pulse before reaching the receivers where it either (1) propagates through the borehole fluid, (2) reflects back to the

borehole fluid at the fluid-solid interface or (3) is transmitted into the solid and refracted back to the fluid. The sonic logs record the time *t* required by a sound wave to travel a given distance of the formation; the interval transit time (or slowness) measured is given in s/m (or μs/ft). Therefore, the slowness or travel time per foot traveled through the formation, Δt is given by (Glover)

$$\Delta_t = \frac{10^6}{V}, \quad (1)$$

where Δt is in microseconds per foot, and the velocity V is in feet per second. The velocity depends on the formation properties including fracture distribution, connectivity and density, hence, the measured slowness indicates the formation.

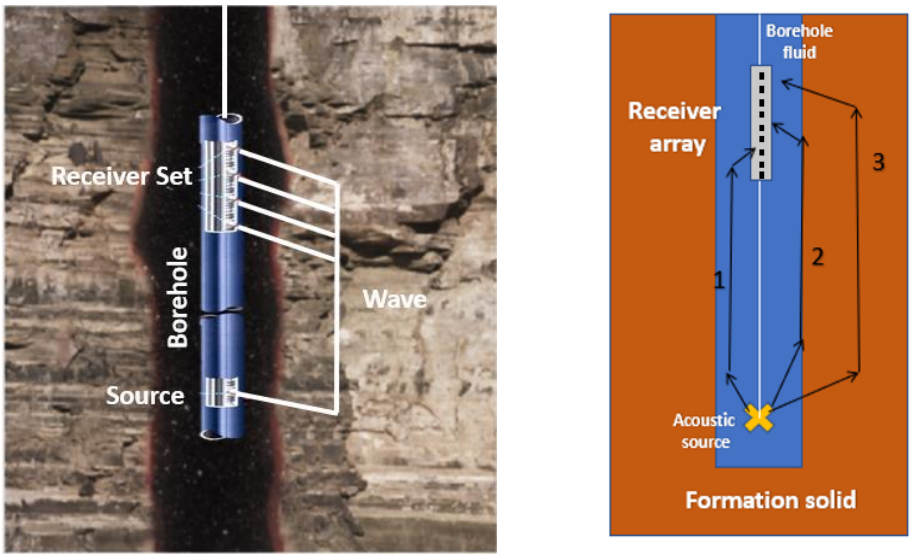

(a) **(b)**

Figure 10 (a) Pulse trajectory of a sonic tool and (b) the different trajectories of the pulse before reaching the receivers. The sonic tool illustration in (a) is taken from LWD-sonic VISION (Schlumberger)

b. Measuring of Elastic Properties Using Sonic Logs

Borehole sonic log measurements (i.e., slownesses) are used to estimate the elastic properties of rock formations from the compressional (P), shear (S), Stoneley, Flexural, and Pseudo-Rayleigh waves. X.-M. Tang and Cheng (2004) showed that the low frequency flexural wave excited by a dipole source asymptotes to the formation shear wave velocity. Moreover, dipole-flexural wave dispersion is used to determine stress-induced azimuthal anisotropy and to diagnose formation alteration.

c. Describing Fractures Using Sonic Logs

The common methods used to detect fractures in shales from sonic logs include cycle skipping, increase in acoustic time difference, decrease in rock density, increase in neutron porosity (H. Tang, Killough, Heidari, & Sun, 2017), chevron (crisscross) patterns caused by mode-conversion interference (Sowards, McCowan, & Drexler, 2012), variations in the V_p/V_s ratio, amplitude reduction of Stoneley-wave, slowness increase caused by the presence of weak fractures, mode conversion and reflections (Boadu & Long, 1996), shrinking and expansion of borehole caused by fluid injection that is manifested by (1) changes in stresses in the rock mass due to changes in void geometry of fractures and (2) changes in fluid and solid content of fractures in fractures (Council, 1996). These methods can be used individually or combined to provide an accurately identification and evaluation of in-situ and induced fractures (Zeng et al., 2016).

The response of sonic logs depends on the orientation of fractures. Horizontal fractures induce cycle skipping phenomenon by acoustic logging that is not detected in the case of vertical fractures. Thus, the need of other logging technique such resistivity,

porosity and lithology logs that can detect fractures oriented at different angles (A. Li et al., 2020).

Chen and Tang (2012) used a modified Biot's poroelastic wave theory for formations with cracks and analyzed the effect of crack density and aspect ratio on the dispersion and attenuation of elastic wave measured with acoustic tools. Chen, Tang, and Qian (2014) showed that for tight formations having low porosity and permeability, the sensitivity of acoustic waves on formation elastic properties is not significant, however, fractures and cracks add signatures to the acoustic waveform data that help in the identification of hydrocarbons. For example, gas saturated cracks are shown to have a huge effect on P-wave and Stoneley wave, but a little effect on the S-wave.

Chen et al. (2014) describe the effect of crack density and gas saturation on velocity dispersion and attenuation with multipole acoustic sources for logging while drilling (LWD) tools in a tight formation with abundant cracks. The crossplot analysis (V_p/V_s vs. V_p) was used for shale gas detection. Moreover, Barbosa et al. (2019) showed that fracture compliance is obtained by studying the velocity change and transmission losses inferred from sonic log data.

d. Numerical Modeling of Well Logging

Finite difference (FD) and finite element methods (FEM) have been widely used for the simulation of borehole sonic logs. Finite difference methods are effective when simulating completely structured stratigraphic models; therefore, they are not accurate in the case of deviated wells because of false reflections generated at the borehole boundaries and poor meshing. Finite element methods are used when arbitrary mesh shapes are needed and yield accurate results for borehole acoustic simulations (Wang,

Kuo, Guo, He, & Zhang, 2018). de la Puente, Dumbser, Käser, and Igel (2008) applied the discontinuous Galerkin method to simulate seismic wave propagation in heterogeneous media containing fluid–solid interfaces, both for 2D and 3D geometries. Frehner and Schmalholz (2010) simulated a time domain FEM to study Stoneley guided wave reflections in formations with fluid-filled fractures. A 2.5 D method in the frequency wavenumber domain was applied by (Zhang, Lin, & Wang, 2011) using the partial differential equations (PDE) interface in COMSOL Multiphysics to study the acoustic field generated by a dipole source in noncircular pipes. Moreover, Matuszyk, Torres-Verdín et al. (2013) developed a frequency-domain FEM approach that enables the use of 2D axisymmetric models to efficiently simulate both monopole and dipole sources. Moreover, P. J. Matuszyk, Torres-Verdín, and Pardo (2013) performed 2D wireline borehole measurements acquired in fractured and thinly bedded formations to evaluate the effects of thin beds and fractures on the wave amplitude and attenuation. P. J. Matuszyk and Demkowicz (2014) extended this method to coupled poroelastic/acoustic/elastic 2D wave propagation problems in the radial-axial coordinate system.

They demonstrated that finite-element methods in the frequency domain are stable and computationally efficient to model borehole waves. Borehole models can be used to model formations with fractures having different orientations, materials infill, dimensions and distributions. Such models are used to study the effect of fractures on the waveforms obtained using monopole and dipole excitations regarding changes in the wave's arrival time, attenuation and dispersion.

2. Core Analysis

a. Core Analysis: Definition

After/during drilling, samples of reservoir rocks (cores) are extracted from the well at different depth to analyze the well conditions and its potential productivity. Core drilling helps locating the reservoir and identifying new hydrocarbon prospects (Ubani, Adeboye, & Oriji, 2012).

b. Measuring of Elastic Properties Using Ultrasonic Analysis

After extracting cores from a reservoir, elastic properties are estimated using static compressive tests and ultrasonic measurements (Ubani et al., 2012). For ultrasonic measurements, a high frequency wave propagates thorough the rock and the compressional (P-waves) and shear (S-waves) velocities are determined form the measured waveforms at the receivers (Fei, Huiyuan, Jun, & Yonghao, 2016; Wyllie, Gregory, & Gardner, 1956). For compressional waves, the particle motion is in the direction of propagation, while for shear waves, the particle motion is perpendicular to the direction of propagation. Shear and compressional velocities provide valuable information about the lithology of rocks, fractures content and fluids through which they propagate.

c. Methods Used to Detect Fracture Properties in Cores

Ultrasonic analysis can be used to detect fractures in cores through studying the effect of different fractures traits (i.e., aspect ratio, crack density, material property, geometry, orientation and intersection) on the resulted waveforms. An experimental and theoretical study has been done by Ding et al. (2019) to study the effect of fracture

porosity, orientation and saturation on the (V_p/V_{sH}) and (V_p/V_{sV}) ratios and their implications on shale gas exploration during hydraulic fracturing. Aligned and randomly distributed fractures were considered. It was shown that horizontal natural fractures can be predicted from an abnormally low (V_p/V_s) ratio with no shear wave splitting.

d. Numerical Modeling of Ultrasonic Measurements

Finite element modeling have been used to improve rock characterization using ultrasonic measurements. Abboud et al. (1998) designed ultrasonic transducers and determined their appropriate elastic properties to model rocks and to minimize the difference between experimental results and finite element predictions. Andrews (2014) performed FEM simulations of ultrasonic models using COMSOL Multiphysics and validated them using experimental data to accurately design new ultrasonic systems and to confirm the absence of numerical instabilities. Moreover, Van Pamel, Sha, Rokhlin, and Lowe (2017) studied the scattering problems in terms of attenuation and dispersion for 3D heterogeneous medium defined by spatial fluctuation of its elastic properties. The method represents the first quantitative validation for the existence of transitional scattering regime. It addresses the differences between structured and unstructured mesh, symmetry and periodic boundary conditions, time stepping, and plane wave excitations which facilitate the implementation of future 3D models for similar heterogeneous formations.

Wang et al. (2018) emphasize the importance of using azimuthal variation in amplitudes (or attenuation anisotropy) to characterize fractures. They used the boundary element method (BEM) to study the effect of different fractures parameters including spatial

arrangement, spatial size parameters and orientation on wave scattering. They demonstrated the following:

- Using same scatters with different spatial arrangements affects the frequency contents of the transmitted wavefields.
- The spatial size parameters of the model affect the frequency of the peak attenuation.
- For oblate inclusions (aspect ratio<1), the amplitude of the transmitted waves is greatly affected by crack orientations.

J. Guo, Shuai, Wei, Ding, and Gurevich (2018) highlighted the importance of fracture detection as they control fluid flow mechanism in hydrocarbon reservoirs. They proposed a theoretical model to show that both fracture thickness and fluid bulk modulus significantly affect dispersion, scattering and attenuation of the P-wave especially in the low frequency effective regime, demonstrated by the displacement discontinuities across the fractures. Their conclusions were validated using ultrasonic measurements which shows a potential to use seismic data to infer fracture parameters.

3. Core Analysis vs. Well Logging

a. Correlating Well Logging with Core Analysis

Core analysis is usually used to reduce uncertainty in reservoir evaluation by offering data representative of the reservoir at in situ conditions. Therefore, the elastic properties can be estimated by core analysis. When cores are limited or cores are not available, the dynamic elastic properties are obtained using seismic or borehole acoustic measurements, which are available continuously in a well. In other words, core analysis

provides a means of obtaining additional information about the reservoir that are unavailable from well logs only (Darling, 2005).

Integrating core analysis and well logs ensures reliable determination of the fundamental elastic and physical properties such as crack density, porosity, permeability and saturation while also reducing uncertainty in measurements within the formation. The data from core analysis and well logs should be correlated to accurately characterize a formation and reduce uncertainty in the measurement (Bu, 2016). A. Li et al. (2020) combined core analysis and log data to accurately determine fracture location by calculating the second derivatives of lg(*R(n)/S(n)*) function for some logging parameters (lithology, porosity and resistivity) with *n* the number of logging points, *R(n)* is range and *S(n)* is standard deviation. The weight of each logging parameter is assigned using an analytical hierarchy process (AHP). A new quantitative parameter indicated by "fracture development coefficient" was introduced to study the degree of fracture development. The fracture development coefficient was shown to have a positive correlation with fracture linear density indicating that higher development of shale fractures' network can be deduced from larger fracture development coefficient.

b. Differences Between the Elastic Properties Obtained Using Core Analysis and Well Logging

The elastic properties obtained from core analysis (ultrasonic measurements) and acoustic logs are different for various reasons. Ultrasonic measurements are performed after extracting cores from high in situ pressure and temperature to the surface and following cleaning, drying and re-saturating processes. Therefore, the

porosity measured on core is different from that determined from log measurements (Ubani et al., 2012). Moreover, ultrasonic measurements yield the direct compressional (P) and shear (S) waves, while borehole acoustic measurements yield the critically refracted waves in the formation and borehole guided waves (e.g., Pseudo Rayleigh and Stoneley modes) that have different lengths of investigation and are not sensitive to the same stiffness coefficients of the rock. In addition, the frequency of acoustic logs ranges from 1 kHz to 50 kHz while that of the ultrasonic measurements ranges from 100 kHz to 1000 kHz (T. Li, Wang, Gu, Wang, & Wang, 2019), which cause sonic logs measurements to have lower velocities than ultrasonic laboratory measurements (Zoback, 2010).

Sample volumes measured by logs and ultrasonic measurements are different (Tutuncu & Sharma, 1992) and scaling from the small cores (cm) to logs (m) requires locating the cores along the borehole with an acceptable uncertainty of $\pm$2-3 ft (Bu, 2016; Mohamed & Kashlaf, 2016). The accuracy of core-depth correlations strongly depends on the core recovery method and the heterogeneity of the formation (Williams & Sharma, 1991). For isotropic homogenous formations, the effects of depth correlation and sampling volumes are small because the arrival time on the digital sonic log remains approximately the same in a $\pm$5 ft from the reported core depth (Tutuncu & Sharma, 1992) while in heterogeneous and anisotropic formations, large uncertainties are assumed.

The volume of investigation is one of the major drawbacks in well logging since it affects the resolution of fracture detection. Most logs average rock properties over equant volumes of 0.3 m which makes them quite sensitive to the presence of individual fractures. This also induces problems in resolving thin beds having a thickness <0.1 m

where in such cases their properties are averaged with those of surrounding beds (Council, 1996).

c. Comparing Core Analysis and Well Logging Using Experimental and Numerical Studies

Experimental studies are used to compare and correlate the elastic properties measured using ultrasonic core analysis and well logs. For example, Tutuncu and Sharma (1992) compared the elastic properties (Young's modulus (E)) obtained using static, ultrasonic and acoustic log measurements in poroelastic sandstone formations. They show that $E_{ultrasonic} > E_{log} > E_{static}$ which indicates that increasing the frequency of the applied strain (or wave) induces a stiffer rock. They also showed that increasing the stress applied on rocks causes cracks to close which increases the rock stiffness and yields smaller differences between the measured dynamic and static moduli. However, experimental analysis is not sufficient to describe all the parameters that yield differences between ultrasonic and log measurements, or to develop generalized fracture characterization workflows.

FEM is a powerful alterative for geomechanical analysis. It has been implemented to independently model well logs and ultrasonic measurements. Caspari et al. (2019) performed numerical simulations of (1) the borehole experiment, (2) the quasi-static upscaling approach and (3) the ultrasonic transmission experiment as a means to study the effect of these three mechanisms on seismic waves attenuation for a fractured porous formation saturated with fluid. It was shown that amplitude decay of propagating P and S waves in fractured fluid saturated media is due to geometrical spreading of the full-waveform sonic log (FWS) data in method (1), displacement of

pore fluid relative to the solid frame in method (2), and transmission losses and scattering caused by energy conversion at fracture interfaces in method (3).

d. Effect of Acquisition Scales on Fracture Parameters

The size of fractures differs between different scales: core, log and seismic. At the core scale, matrix properties including porosity and permeability are usually studied and millimeter-scale fractures (or cracks) are found. At the log scale, calibration of formation elastic properties must be done so larger (decimeter) fractures are estimated. The seismic scale is used for geomechanical and hydrodynamical modeling. It is of great interest in fracture characterization since it is mostly responsible for hydrocarbon flow and helps in the detection of critically stressed fractures (Bayuk, Dubinya, Garagash, Tikhotskiy, & Tikhotskaya, 2019). Therefore, it is important to link these scales so that seismic interpretations will provide reliable estimations of fractures parameters by taking into account the inner microstructure of the rock (Bayuk et al., 2019). For example, Kumar (2013) applied Backus averaging (Backus, 1962) to estimate seismic anisotropy from equivalent well-log data.

Integrating the three scales yield a 3D fracture map that highlights the 3D distribution of fractures and their relative opening, volume concentration and degree of connectivity (Bayuk et al., 2019).

F. The Effective Medium Theories (EMT)

1. EMT Establishment

The effective elastic properties of a composite or porous material can be estimated using theories that depend on three main properties of the individual

components of a rock: (a) the elastic properties, (b) the volume fraction and (c) the geometric shape and spatial distribution (Mavko, Mukerji, & Dvorkin, 2020).

- The bounding methods (maximum and minimum elastic properties) are obtained using (a) and (b) and yield the upper and lower bounds known as Hashin–Shtrikman and Voigt–Reuss.
- These estimates are improved using a second approach that includes statistical information about the different phases present (Beran & Molyneux, 1966).
- The third approach assumes extremely specific inclusion shapes and is known by the effective medium theory (EMT).

The establishment of EMT started by Eshelby (1957) who presented a theoretical model to estimate the effective properties of a single ellipsoidal inclusion embedded in a homogeneous elastic solid. Later, the effective theories were broadened to predict the effective elastic properties of fractured and porous medium.
The most common approach was the non-interaction approximation (NIA) which covers general anisotropy related to the distribution of inclusions and to the background but does not account for the interactions between pores and cracks.

2. First Type of NIA Approach (First Order Models)

In the first type of NIA, the effective compliance of the medium is estimated by computing the contributions from the matrix and adding to that an extra compliance due to pores and cracks (Mavko et al., 2020). The first type NIA was developed as follows:

- Bristow (1960) studied the effective elastic properties of fractured medium with random crack orientations.

- A general form of NIA was developed by Mark Kachanov (1980) to compute general effective anisotropy of an isotropic matrix with arbitrarily oriented dry cracks. The theory was then extended by M Kachanov, Tsukrov, and Shafiro (1994) to cover diverse shapes of arbitrary orientated dry inclusions and by Shafiro and Kachanov (1997) for fluid filled arbitrary orientated cracks.
- Sevostianov and Kachanov (1999) extended the EMT to include arbitrary ellipsoidal cracks defined by arbitrary elastic constants.
- Mark Kachanov (1992) showed that the progression of fractures in a medium does not deteriorate the effective properties estimated using compliance-based NIA so that the latter can still provide accurate estimations for medium with a large crack density and strong interactions.
- The effect of background anisotropy was recently added by J. Guo, Han, Fu, Xu, and Fang (2019) through performing static simulations for transversely isotropic background permeated by aligned penny-shaped cracks.
- Kuster and Toksöz (1974) is also an effective medium method that is limited to dilute concentration of inclusions.

3. Second Type of NIA Approach (Second Order Models)

In the second type of NIA, the effective stiffnesses are directly estimated as a function of porosity and crack density (O'Connell & Budiansky, 1974). The second type NIA was developed as follows:

- Hudson (1980, 1981) established the effective stiffness coefficients for an elastic solid permeated with thin, penny-shaped ellipsoidal inclusions. Hudson's theory analyzes the mean wavefield based on a scattering theory,

- Hudson's first order theory ignores the interactions between cracks, while Hudson's second order theory considers a pair-wise interaction between cracks.

4. Higher Crack Interactions Theories (High Order Models)

The previous geometry methods estimate the effective properties of anisotropic medium by assuming a single inclusion embedded in an infinite background defined with different materials. In case a distribution of multiple inclusions exists, each method uses its own scheme to estimate the effective properties. However, the previous methods have difficulties in estimating the interactions between inclusions in close proximity which make them limited only to dilute distributions of inclusions (Mavko et al., 2020).

Two popular methods known by the self-consistent approximation (SCA) (Budiansky, 1965; Budiansky & O'connell, 1976; Hill, 1965) and the differential effective medium (DEM) (Berryman, 1980) extended the previous geometry methods to slightly large concentrations of inclusions (pores and cracks). The SCA and DEM methods both account for crack interactions but differ in the scheme used to estimate the effective properties (Mavko et al., 2020).

- The self-consistent approximation (SCA) defines the medium as a collection of constituents without specifying any preferable host matrix,
- The differential effective medium (DEM) assumes a preferred host matrix where each constituent is treated asymmetrically.

Another two popular effective models that consider high crack density effects are the smoothing methods known by T-matrix (Jakobsen, Hudson, & Johansen, 2003) and Linear Slip (LS) (Schoenberg, 1980). These models are important to obtain physically

reasonable values at high crack density where the interactions between inclusions in close proximity cannot be neglected.

5. EMTs' Limitations

EMTs depend on the type of model being approximated (isotropic or anisotropic) and have limitations in terms of the inclusions' crack density, aspect ratio, interactions, material representation and spatial distribution. The main variable in these EMT models is epsilon "ε" (crack density) or volume concentration. All EMT assume idealized crack shape (ellipsoid) with cavities being isolated with respect to fluid flow. EMT do not simulate acoustic scattering behavior effects nor includes fluid-related dispersion mechanisms (Mavko et al., 2020).

The scattering attenuation mechanisms depend mainly on the dominant wavelength "λ" and on the diameter of the scattering heterogeneity "d_s" and include: (1) Rayleigh scattering ($\lambda > d_s$), (2) Stochastic/Mie scattering ($\lambda = d_s$) and (3) Diffusion scattering ($\lambda < d_s$) with the possibility of these mechanisms to overlap.

6. General Comparison Between Different Effective Medium Theories

A theoretical comparison between different effective models with first, second and high orders is provided by Hu and McMechan (2010) for a transversely isotropic coal medium with a horizontal symmetry axis (HTI). The results are shown in Figure 11 below:

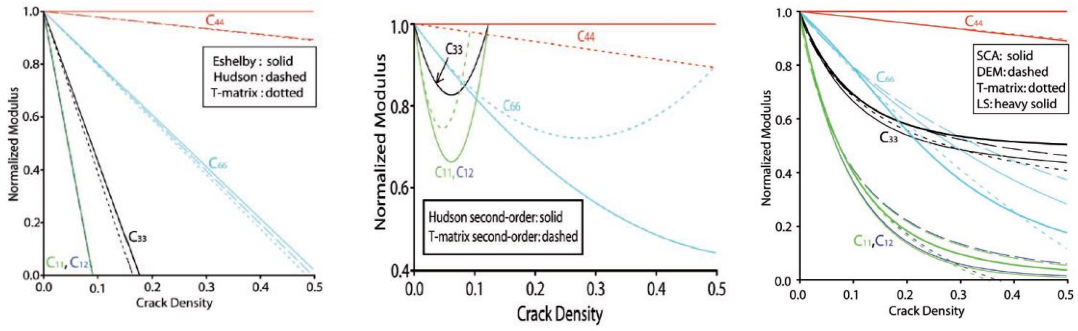

(a) **(b)** **(c)**

Figure 11 Comparison of different effective medium models with (a) first, (b) second and (c) higher orders, respectively for a coal medium with HTI geometry and an aspect ratio of 0.05 (Hu & McMechan, 2010)

- The first order models (Eshelby, Hudson 1st and T-matrix 1st) shown in Figure 11 (a) are suitable for medium with small crack density having cracks separated by a large average distance so that the crack interactions between them can be ignored (Hu & McMechan, 2010).
  - The estimations from first order methods overlap at a crack density "e" <0.02 and becomes flat for an aspect ratio of ~0.01 indicating an effective isotropic medium.
  - Randomly distributed dry fractures with $e \geq 0.02$, Hudson contradicts Eshelby (1957) by showing that the interactions between cracks result in a reduction in fracture induced anisotropy and implies higher stiffnesses compared to those predicted by J. Hudson (1980).
  - Grechka (2005) showed that Hudson fails to predict the elliptical anisotropy caused by dry fractures as in Mori-Tanaka **(**based on Eshelby model).

- Schoenberg (1980) and Mark Kachanov (1992) theories. His results are supported using numerical FEM computations.

- Second order formulations (Hudson 2nd and T-matrix 2nd) shown in Figure 11 (b) nearly overlap at a e <0.03. For 1st and 2nd order models, stiffnesses $C_{11} \approx C_{12}$ for dry crack cases and they are exactly equal for Hudson's formulation.
- The high order (crack interaction) effective models (SCA, DEM, LS and T-matrix) shown in Figure 11 (c) are proved to provide very similar estimations at ε < 0.03. Beyond this, the spatial distribution of inclusions significantly affects the results where the shear modulus normal to the plane of symmetry (C_{44}) has the highest difference between different methods.
  - Interactions are accounted for implicitly in SCA and DEM and explicitly in LS and T-matrix (Hu & McMechan, 2010).
  - For the same volume concentration and using a fixed inclusion geometry, the effective elastic moduli values predicted by Kuster and Toksöz (1974) are stiffer than the DEM estimation, which in turn are stiffer than the SCA elastic moduli (Mavko et al., 2020).

7. Detailed Explanation of the Selected FEM Models

The effective medium theories are used to estimate the effective elastic moduli and attenuation coefficients of a rock in terms of its constituents and pore space. Among the different methods that estimate effective properties for fractured rock, the following EMT models are considered as they are common:

- Hudson's 1st and 2nd orders.
- Self-consistent approximations (SCA).

- Differential effective medium (DEM).

The theories are discussed in terms of their assumptions, approximations, specific crack parametrizations, applications and limitations.

a. Hudson 1st and 2nd Orders

i. Hudson: Definition and Assumptions

Hudson (1980, 1981) differs from the NIA in its way to define the compliances. In NIA, the compliances are defined as linear functions of the crack density "e", however, Hudson (1980, 1981) constructs the effective stiffnesses as power series expansions with respect to e.

Below is a general summary on the assumptions adopted by Hudson's theory (Mavko et al., 2020):

- Hudson 1st order neglects crack interaction.
- Hudson 2nd order assumes a pair-wise crack interaction.
- Idealized ellipsoidal crack shape (penny-shaped) is assumed.
- Equation depends on aspect ratio and crack density of inclusions as two main parameters.
- Background and inclusions are defined using isotropic, linear and elastic materials.
- Cracks are isolated with respect to fluid flow.
- Dry, weak, or fluid thin inclusions are assumed.
- Small aspect ratios are assumed.
- Small crack density (up to 10%) or small contact density are assumed.

- Crack dimensions are assumed to be much smaller than a wavelength.
- Crack radius and the distance between cracks are much smaller than a wavelength.
- Available for randomly (isotropic medium) or oriented cracks (anisotropic VTI medium).
- For dry cavities modeling, the inclusion moduli are set to zero.
- For fluid-saturated cavities modeling, the inclusion shear modulus is set to zero.
- Available for oriented distributions other than random or strictly aligned.
- Provides effective elastic stiffnesses and attenuation coefficients for elastic waves in effective isotropic and isotropic cracked media.

ii. Hudson 1st Order vs. Hudson 2nd Order

- Hudson 1^{st} and 2^{nd} orders are obtained by truncating the power series after either the linear or the quadratic term, respectively. Hudson 1^{st} abides by the symmetry properties for transverse isotropy, while Hudson 2^{nd} abides by those of a hexagonal symmetry.
- The concentration of fractures is assumed to be dilute in Hudson 1^{st} order so that the disturbances of stresses and strains produced by cracks do not influence other adjacent cracks. In contrary, pair-wise interaction is assumed in Hudson 2^{nd} order.
- The second-order expansion provides unphysical approximations at high crack density (Grechka & Kachanov, 2006a) since it does not represent uniformly converging series. Thus, for crack density exceeding the formal limit of 0.1, the

estimated moduli of Hudson 2nd order increase when crack density increases (Mavko book, Cheng, 1993).

- It is recommended to use the first order correction so that inaccurate approximations from using the second order correction are avoided. Cheng (1993) has proposed a Pade´ approximation to avoid the second order problem (Mavko et al., 2020).

iii. Hudson: Models

- Hudson models the transverse isotropic symmetry of a cracked medium by taking a single set of cracks with cracks normal aligned along the 3-axis.
- Hudson (1980, 1981) covers multiple symmetrical distributions of inclusions such as the rotationally symmetric crack distribution and a cone shape distribution with cracks normal randomly distributed at a fixed angle from the 3-axis.
- Moreover, the effective elastic properties of an array of parallel faults known as heavily faulted structures were covered by J. A. Hudson and Liu (1999).

iv. Hudson: Applications

Hudson 1st order model is extensively used in exploration seismology (Grechka, 2005) especially for models that are transversely isotropic. The model is used to invert the effective anisotropic properties of fractured formations and thus estimating the fracture properties and characterizing the formation (Bakulin, Grechka, & Tsvankin, 2000).

Since Hudson model can be used directly as a "forward modeling engine" as described by Mavko et al. (2020) for fractured formations, it is important to study the accuracy of this model and check its validity to obtain reliable fracture characteristics.

v. Hudson: Limitations

- The formal limit of Hudosn's 1st and 2nd orders predictions is less than 0.1 crack density (Hill, 1965) for small aspect ratios "AR" (e,g., AR $\leq$0.05) (Hu & McMechan, 2010). Grechka (2005) showed that for dry fractures with AR = 0.02, the validity of assumption decreases to comprise only very small crack densities $e \leq 0.01$.
- A bias in the magnitudes of the effective anisotropic coefficients towards their higher values is expected by using Hudson' theory. This is caused by ignoring crack interactions and exist for the whole crack density range and for any fluid infill type (Z. Guo, Li, Liu, Feng, & Shen, 2013). However, Hudson still yield good approximations for liquid filled fractures where the strength of anisotropy caused by the fractures is mild compared to the dry case.
- To obtain an adequate representation of crack induced anisotropy, several crack sets with angular distributions must be used instead of a single crack set (Mavko et al., 2020).
- The anisotropic coefficient $\gamma(V)$ for fractures located in volume V given by Hudson's theory for either liquid-filled or dry cracks is reasonably accurate and is close to the fracture density value.
- However, in case of dry cracks, significant errors present for assuming the anisotropic coefficients $\varepsilon(V)$ and $\delta(V)$ using Hudson's theory. Numerical

computations show that these two anisotropic coefficients are significantly closer to each other for water filled and dry fractures than Hudson's theory suggests. This observation leads to difficult discrimination of fluid content from seismic data using the Hudson theory (Grechka, 2005).

b. Self-Consistent Approximation (SCA) And Differential Effective Medium (DEM)

i. Definition and Assumptions

The two methods belong to high order effective medium models where the crack interactions are taken into account. Below is a general summary on the assumptions used in SCA and DEM theories (Mavko et al., 2020):

- SCA treats the medium as an aggregate.
- DEM assumes a host background embedded with inclusions.
- Both account for interactions between cracks.
- Suitable for higher concentrations of inclusions.
- Background and inclusions are defined using isotropic, linear and elastic materials.
- Cracks are isolated with respect to fluid flow.
- Idealized ellipsoidal crack shape (penny-shaped) is assumed.
- Equation depends on aspect ratio and crack density of inclusions as the two main parameters.
- For dry cavities modeling, the inclusion moduli are set to zero.
- For fluid-saturated cavities modeling, the inclusion shear modulus is set to zero.
- Crack dimensions are assumed to be much smaller than a wavelength.

- Available for randomly (isotropic medium) or oriented cracks (anisotropic VTI medium). Hornby, Schwartz, and Hudson (1994) extended the SCA and DEM methods to the anisotropic solids in order to cover the elastic properties of shales. VTI versions (transversely isotropic medium) for anisotropic rocks with spheroidal inclusions invoke a fourth-rank tensor calculated by Mura (2013) from the response of an unbounded matrix of the effective medium.
- DEM and SCA are both non-deterministic theories since the spatial distribution of cracks is not included. They are also available for oriented distributions other than random or strictly aligned (Hu & McMechan, 2010).

ii. SCA: Models and Limitations

Berryman's Self-Consistent Approximation (SCA), also known as Coherent Potential Approximation, uses an integration procedure to account for the deformation of inclusions added successively to a background medium with unknown effective elastic properties calculated by subsequent iterations. The approach is also based on the mathematical solution of the deformation of isolated inclusions, while the background medium is replaced by the as-yet-unknown effective medium (Mavko et al., 2020). Thus, the effective elastic stiffness tensor is obtained by combining the elastic stiffness tensors of different elements using an element weight equals to the inclusion porosity (Eshelby, 1957).

- Bruggeman (1935) developed the SCA method to calculate the effective conductivity. It was later applied by Kröner (1958) to compute the effective elastic properties of polycrystals then by Hill (1965) and Budiansky (1965) for composite materials.

- Te Wu (1966) developed the SCA to estimate the moduli of two-phase composites.
- Kinoshita and Mura (1971) provided the equations for a matrix with aligned fractures to represent transversely isotropic matrices.
- Budiansky and O'connell (1976) worked together to formulate the effective equations of bulk and shear moduli for a cracked solid with randomly oriented dry inclusions having a penny-shaped geometry. Hoenig (1979) applied their formula to non-randomly oriented dry cracks with a parallel or cylindrical symmetry orientation.
- The equations were further expanded to cover infinitely thin fluid filled cracks having also a penny-shaped geometry. O'Connell and Budiansky (1977) enhanced the equations to provide adequate estimations for cracks with a soft fluid saturation and small aspect ratio.
- Gottesman and MA (1980) further extended the SCA method to cover 2D orthotropic composites with cracks parallel to the orthotropy axes, which was reformulated by Laws and Laws and Brockenbrough (1987) to include the effect of microcracks shapes on stiffness losses of brittle solids.
- A more general form of SCA for N-phase composites including minerals and pores with different shapes (spheres, Needles, disks and penny cracks). The equations are coupled, sums over all phases and are solved by simultaneous iteration (Berryman, 1980, 1995).
- SCA Limitations: Berryman's Self-Consistent Approximation (SCA) must be used with care for fluid saturated composites. The formula does not converge in

case cracks are modeled as disks; however, a non-singular solution is obtained using penny-shaped fluid filled cracks which converges rapidly.

iii. DEM: Models and Limitations

The Differential Effective Medium (DEM) theory estimates the effective moduli of two phases composites by considering the matrix material as a load bearing (Sayar, 2015). DEM theory depends on the construction path taken, i.e., the effective elastic properties are calculated by incrementally adding inclusions of a phase 2 to the matrix of phase 1. Thus, phase 1 represents the matrix only when the concentration of phase 2 is zero and is updated at each increment (Cleary, Lee, & Chen, 1980; R. W. Zimmerman, 1990).

- Bruggeman (1935) was the first to propose the DEM theory which was further developed by Norris (1985), R. W. Zimmerman (1990) and Berryman (1992). The method assumes that either the matrix or the inclusion material is displaced at each new addition of a pore or inclusion.
- A modified scheme of the DEM theory was proposed by R. Zimmerman (1984) which assumes that only the matrix host is displaced at each new addition. This assumption gives slightly stiffer moduli compared with conventional DEM model at volume concentrations > 10 %.
- Mukerji, Berryman, Mavko, and Berge (1995) proposed a new model that incorporates the percolation behavior which specifies a critical porosity value at which the host matrix falls apart. The critical porosity for most reservoirs is significantly smaller than 1 and defines the limit for the host to remain connected so that it can be still considered as load bearing. In contrary, the

conventional DEM theory assumes a critical porosity value of 1 so it does not represent well actual reservoirs.

- DEM Limitations: The DEM theory relies only on the final volume concentrations of the constituents to calculate the effective moduli of the inhomogeneous medium. However, the effective moduli of a cracked medium depend also on the order in which the inclusions are incrementally added. Thus, DEM method cannot be used to accurately describe the true evolution of rock porosity in nature.

iv. Validation for DEM And SCA

- The SCA and DEM theories provide reliable approximations that are qualitatively acceptable at higher crack densities.
- The estimated effective moduli slightly differ between SCA and DEM while both decrease (for weak and dry fractures infill) while crack density increases, without being negative (Mavko et al., 2020).
- The SCA and DEM theories are effective medium models that implicitly account for crack-crack interaction without explicitly describing how these interactions are taking place (Mavko et al., 2020).
- Hu and McMechan (2010) showed that for a constant aspect ratio, SCA and DEM models provide accurate estimations for random crack distributions.

c. Cautions for EMTs Models

All EMT theories assume that cavities are isolated with respect to fluid flow. This assumption causes pore pressures to become non-equilibrated and adiabatic.

Therefore, EMT estimations are appropriate for modeling very high frequency ultrasonic behavior.

For low frequency field measurements, enough time is available for wave induced pore pressure increments to flow and equilibrate, therefore it is recommended to find the effective moduli for dry cavities using general EMT methods that correspond to isolated cavities and then saturate them with relations that describe well connected pores such as the Brown and Korringa relations for Hudson approximations and the low frequency SCA-Gassmann method for SCA and DEM approximations (Mavko et al., 2020).

Z. Guo and Li (2015) compared the high frequency SCA method to the low frequency SCA-Gassmann method in predicting shear velocity from sonic compressional measurements. The former gives better approximations for the Barnet shale case, while both gives same results for Marble Falls interval. This dependence on whether the sonic frequency range is within the validity range of a specific method or within the transition range. As noticed, these methods still have the tendency to approximate low-frequency theories (Mavko et al., 2020).

d. Previous Work on EMTs Validation

The main crack parameters that affect the effective elastic properties of a fractured formation are the spatial distributions, orientation, shape and fluid content of inclusions. Moreover, the dominant frequency, the acquisition method, the distance between cracks compared to wavelength, wavelength/crack diameter which relates to scattering mechanism and the crack density which affects the interaction between cracks at higher values yield differences in measured effective properties.

The mathematical expression of anisotropy is included within the elastic stiffness tensor, therefore when using anisotropic seismic, ultrasonic or acoustic modeling followed by an inversion, inference and interpretation processes to characterize a reservoir, it is important to represent rock and fracture properties in terms of the equivalent anisotropic elastic stiffness tensor (Hu & McMechan, 2010).

Due to the assumptions and limitations of EMTs, there is a need for extensive lab measurements and numerical models to test the validity of the theoretical effective medium models. The accuracy of the effective medium theories has been studied in literature using different physical and numerical models. Each study targets a specific geometrical model with specified rock and fractures parameters. The inclusions might by dry or filled with a weak solid or a fluid material.

i. Validation of EMTs Using Numerical Modeling

The accuracy of the effective medium theories was studied using different finite element and finite difference numerical models.

- **EMT Validation Using the Finite Element Method (FEM)**

Dahm and Becker (1998) compared the effect of in-plane or anti-plane highly fractured shear cracks with a crack density up to 20% on the validity of the DEM theory in approximating the effective moduli. The fractures are randomly oriented or aligned (VTI) and have an equal length or follow a logarithmic size distribution. The DEM is found to be important for in-plane shear cracks at high crack densities while better results were obtained using a model that disregards crack-crack interaction for the anti-plane cracks.

Grechka and Kachanov (2006a) imitated real fractured geometries by assuming regular ellipsoids shape and other irregular fracture shapes including (circular, porelike, non-circular and micro-corrugated) embedded in an isotropic host. The fractures are randomly distributed, either intersecting or non-intersecting, distributed as single or multiple sets and are either dry or saturated with liquid. The crack density was varied up to 20% by changing the number of cracks, their aspect ratios from 0.04 to 0.08 and the locations of their centers. The cracks are assumed to be flat so that the interactions in the stress fields of different cracks can be ignored, constant loads (static modeling) are applied to represent the remote stress boundary. The anisotropic coefficients and stress components were studied for the different models and compared to Hudson and Linear slip (LS) effective models. The main findings are listed below:

- The linear slip theory provides satisfactorily estimations for effective elasticity for all models.
- Hudson's first-order theory encounters problems for small $V_{S,b}/V_{p,b}$ ratios (b indicates background) or large Poisson's ratios.
- Hudson's 1st order theory breaks down for any nonzero crack density of dry fractures in the limit $gb \rightarrow 0$ defined as

$$gb = \frac{V_{s,b}^2}{V_{p,b}^2}, \quad (2)$$

- Regular isolated, penny-shaped cracks can be successfully replaced by planar, irregular and possibly intersecting fractures. To replace regular fractures by irregular circular ones, the effective elliptical orthotropy should be conserved.
- The effective moduli of rocks with dry circular fractures are almost independent of aspect ratio.

Grechka and Kachanov (2006b studied Grechka and Kachanov (2006b) the effect of fractures' intersections and interactions on randomly distributed ellipsoidal dry cracks at partial crack densities up to 6%. The NIA predictions of the effective elasticity compared to the estimated values obtained using static modeling (applied loads) were good in all cases including intersecting and non-intersecting fractures. According to the author, the NIA can be considered as the method of choice for fracture characterization since it is barely affected by fractures' intersection and interaction.

Grechka and Kachanov (2006c) compared the effect of crack-induced orthotropy for randomly distributed vertical cracks. The cracks have shapes of circular, thin, oblate ellipsoids, a variable density up to 10% and are either dry or water filled. The computation results of effective velocity, anisotropic coefficient and anellipticity coefficients using uniaxial static loading were compared to the predictions using EMTs. It was shown that Hudson 1st and 2nd orders provided inferior estimations compared to Schoenberg (LS) and Kachanov (NIA) theories especially for dry fractures. LS and NIA fit FEM computations with good accuracy and are shown to be useful for fracture characterization. The authors highlighted that a smaller aspect ratio below [0.1-0.15] will not affect the effective properties of dry fractures, while the aspect ratio value is interestingly important for fluid filled fractures cases. An inversion technique was also applied to zero-offset travel times of P-waves and two split shear waves to identify parameters of multiple fracture sets from multi-azimuth surface reflection data.

Grechka, Vasconcelos, and Kachanov (2006) showed that the effective moduli obtained from remote loading (static modeling) of fractured media with irregular shapes (e.g., rectangles) or regular circular assumption adopted by EMTs hold the same

accuracy. The irregular cracks sets are dry, have a crack density within [0.02-0.09] and are possibly partially filled or intersecting.

Grechka (2005) numerically supports Hudson's theory using FEM static modeling through fractured rocks having ellipsoidal cracks with 0.2 aspect ratio and a crack density up to 10%. They compared the effect of single to many inclusions and showed that inter-fracture communications in horizontal transverse isotropy (HTI) media, ignored by Hudson theory, affects the accuracy of the results. They also suggested to use the Eshelby solution of a single ellipsoidal inclusion to specify the limits of applicability of EMTs that assume dilute concentration such as in the Hudson theory. Hudson's theory was also shown to provide more reliable estimates for dry fractures compared to water filled fractures. The Numerical modeling highlights the effect of different aspect ratios (0.02, 0.1 and 0.2) or crack size on crack interactions and therefore on EMTs' estimations. This is explained by the stronger interaction obtained for smaller fractures during static deformation that typically stiffens effective media and causes a reduction in the magnitude anisotropy.

- **EMT Validity Using the Finite Difference Method (FD)**

Saenger, Gold, and Shapiro (2000) derived a new rotated staggered grid technique that avoids the need of using boundary conditions when simulating the propagation of elastic waves in a medium embedded with cracks, pores or free surfaces. The method was applied by Saenger and Shapiro (2002) to study the effect of increasing the crack density from 2.5% to 80%. Different 2D models' combinations were constructed with multiple porosity [0.2-14] %, different numbers of cracks, and different aspect ratios [0.021-0.14]. The fractures were modeled as a middle region bounded by homogenous materials so that 2D models can represent 3D transversely

isotropic medium. Numerical dynamic simulations acquired by applying a plane wave were compared to static theories including NIA, SCA and DEM that estimate the effective P-, SV- and SH- velocities in the long wavelength limit. The dry cracks are randomly distributed and randomly orientated, rectilinear, non-intersecting and thin. The numerical results up to crack density of 30% agreed with the results of the modified DEM (or differential) self-consistent theory. However, to obtain accurate results for intersecting cracks, the numerical results must be compared with the modified DEM estimates that account for the critical porosity value.

Saenger, Krüger, and Shapiro (2004) also applied the new rotated staggered technique to study the effective velocities and scattering attenuation in 3D fractured media by simulating ultrasonic plane waves with a central frequency of 800 kHz. Periodic boundary conditions were applied in the two horizontal directions. The cracked models were built with crack densities up to 97.7%, porosities up to 10.6% and an aspect ratio of 0.0025. The inclusions modeled as thin penny-shaped cracks are randomly distributed and randomly orientated, dry or fluid filled and are intersecting or non-intersecting. The computed P- and S- waves velocities were compared to the effective velocities estimated using NIA, Kuster and Toksöz, SCA and DEM theories. For non-intersecting void or fluid filled cracks, the models considered reach a crack density of 18% and indicated that P- and S-waves velocities are in good agreement with the predictions of SCA method. For intersecting cracks, the effective velocities slightly differ from those obtained using non the intersecting cracks, where the numerical values that fall after a crack density equivalent to the connectivity percolation threshold (20% to 30%) are in better agreement with the DEM. In addition, they demonstrated that the

scattering attenuation coefficient of the mean field is in excellent agreement with Hudson's approximations.

Saenger, Krüger, and Shapiro (2006) applied the new viscoelastic rotated staggered technique derived in Ass' ad, Tatham, and McDonald (1992) in order to transform a dynamic computation using uniform displacement to a static one, which is similar to a uniform stress by attenuating all non-zero available frequencies. The fractured model was built by embedding randomly distributed dry parallel cracks with a crack density of 0.2 in-between homogenous bounds. The static results are shown to give results similar to theoretical static upper bound. The explained that the DEM method is capable to produce accurate results at higher crack densities which is not the case for the NIA method. The validity of DEM method for both static and dynamic measurements depends on scale effects represented by the ratio of the VE (volume element) edge length/crack length. A ratio < 20 is shown to give strongly varying effective moduli between different static and dynamic methods. A scale >20 is needed for both the dynamic and static results to verify the DEM theory.

ii. Validation of EMTs Using Experimental Work

Physical modeling combined with numerical simulations enhance the understanding of effective medium theories and confirm their application conditions. Below are examples of some experimental work for studying the accuracy of EMTs. Ass' ad et al. (1992) was the first to use a pulse transmission method in a series of physical models composed by epoxy resin with inclusions of thin rubber discs of approximately equal cross-sectional areas. His work reflected on the effect of seismic plane-wave propagation on fractured models with cracks filled with a weak material to verify the accuracy of Hudson theory.

The conditions of Hudson were adopted in his models, i.e., a wavelength that is greater than the dimensions of the individual cracks and their separation distance, and cracks are in dilute concentration. Seismic measurements S-waves velocities at different polarization and propagation directions were studied for crack densities up to 10%. The results revealed that S1 velocities (polarized parallel to inclusions plane) agree well with Hudson theories, however, S2 velocities (polarized perpendicular inclusions plane) agree well with Hudson theories up to 7% and diverge at higher crack densities. The change of anisotropy as a function of crack density is represented by Ass' ad et al. (1992) anisotropy parameter γ defined by

$$\gamma = \frac{1}{2}\left(\frac{V_{S_1^2}}{V_{S_2^2}} - 1\right), \tag{3}$$

The results revealed a huge deviation from theoretical at 10% crack density which might be justifiable by the effect of crack-crack interaction and their coalescence at high crack density. As a result, seismic techniques can rely on such observable anisotropy to distinguish between microcracks and larger macrocracks.

Ass' ad, Tatham, McDonald, Kusky, and Jech (1993) addressed penny-shaped inclusions that are oriented in plane but randomly distributed, with a crack density up to 10% and a constant aspect ratio of 0.06. P-wave and S-wave velocities are obtained at different polarizations (from normal 0° to tangential 90° to the direction of the inclusion plane). S1 and S2 polarized velocities show an excellent agreement with Hudson theory up to 7% crack density and diverge at higher crack densities. In contrast, P-wave polarized velocities show a good agreement with Hudson only at low crack densities (up to 3%) and show a large divergence from the theory for higher crack densities. The ratio V_P/V_S for models with 0.06 aspect ratio increases as crack density (tested up to

10%) or porosity increases (tested up to 3.75%) for velocities normal to inclusions plane and slightly decreases for velocities parallel to the inclusion plane.

Ass' Ad, McDonald, Tatham, and Kusky (1996) extended his previous work to study the effect of different aspect ratios (0.012, 0.06 and 0.13) with a fixed crack density of 5%. Experimental results show a good agreement with Hudson theory for P-wave velocity only at the smallest aspect ratio (0.012), however, the S-waves velocities agrees with Hudson independent of the aspect ratio used. The effect of frequency (from 0 to 35 Hz) on velocity (dispersion analysis) was studied using a multiple-filtering technique. Velocity results for S1 and S2 waves show a maximum dispersion at a 0° angle of incidence and the minimum velocity dispersion at a 90° angle of incidence. The results suggested that the effect of crack density on anisotropy is more important than the effect of the aspect ratio. Finally, they showed that the ratio V_P/V_S is anisotropic; for models with 5% crack density, the ratio decreases as aspect ratio (tested up to 0.13) or porosity (tested up to 40%) increases for velocities normal to the inclusion plane and remains constant for velocities parallel to the inclusion plane.

J. Guo et al. (2018) studied the effect of fracture thickness and fluid content on P-wave scattering, dispersion and attenuation in carbonate like fractured rocks. Their theoretical model is represented by a reservoir with large 2D aligned fracture corridors with centers distributed randomly and sparsely with an aspect ratio of 0.01 and saturated with a viscous fluid. The studied variables include the fracture thickness, crack density [1-10]%, frequency range [10-1000] Hz and the fluid bulk modulus. The results show that P-wave dispersion and attenuation are greatly affected by fracture thickness, central frequency and crack density. For the low frequency regime, the dispersion increases with crack density while a stable velocity is obtained at higher frequencies independent

of the crack density. In addition, increasing the fracture thickness causes the P-wave velocity to decrease in the low frequency regime and to increase at high frequencies. This reverse in velocity is related to the peak scattering attenuation that occurs when the seismic wavelength is comparable to the fracture length (Kawahara & Yamashita, 1992). The dispersion of P-wave caused by changing fluid bulk modulus followed the same trend obtained by changing the fracture thickness (decreases in the low frequency regime and increases at high frequencies) but the highest dispersion is for the lowest bulk modulus (0 GPa). Ultrasonic measurements were performed on 3D synthetic epoxy mixture embedded with fractures modeled as penny-shaped rubber discs fractures (weak material) and compared to EMTs (Hudson 1st and 2nd, SCA and NIA). Ultrasonic measurements were taken at different frequencies (660, 210 and 97) kHz. The results show overall good agreement between Hudson 1st and 2nd and the experimental results. P-wave parallel greatly agreed with theoretical results at all frequencies and for all fracture thickness, however, P-wave perpendicular only agreed at high frequencies and divert at smaller frequencies after a small crack thickness. They also concluded that crack-crack interaction should not be neglected when the ratio between S-wave wavelength to crack diameter is less than 5. A gap between ultrasonic S2-wave velocity and theoretical predictions was observed at a frequency of 100 kHz. According to the author, the potential of extracting these parameters from the seismic data can help in fracture detection.

Shuai et al. (2020) performed ultrasonic experiments to study the accuracy limit of NIA, Hudson and SCA theories in quantifying the crack density for VTI fractured rocks. The models include an epoxy matrix embedded by fractures' layers of equal thicknesses made from several penny-shaped ellipsoidal inclusions. The ellipsoids

represent weak material, with an aspect ratio of 0.04. The effects of varying the crack density (up to 12%) and central frequency (500, 250, 100) kHz on the P-wave and S-wave in the directions parallel and perpendicular to the fractures are studied. Fast S-wave is polarized parallel to the fractures plane while Slow S-wave is polarized perpendicular to the fractures. The findings of the study are as follows:

- P-wave and S-wave velocities decrease as crack density increases with a major decrease in amplitude for the fast S-wave.
- Lowering the central frequency of the source causes more energy dissipation in the matrix so that measured velocities are lower and the deviation from EMTs approximations are higher.
- P-wave velocities fit better the Hudson 1st order approximations.
- Slow S-wave velocities are closer to the anisotropic SCA and compliance-based NIA model, while fast S-wave velocities laid between the Hudson theory and compliance-based NIA model.
- The P-wave velocity resulted in better agreements with EMTs compared to S-wave velocities. This might be related to the ratio of wavelength to crack diameter of the P wave which is larger (nearly two times) than that of the S wave. Therefore, the long wavelength assumption is more satisfied for the P wave.
- For slow S-wave velocity, the agreements with EMTs highly diverged at low frequency, which is due to the fact that measurement frequencies lie in the Mie scattering regime for S2 wave.
- The importance of EMT in quantifying the crack density was demonstrated for Hudson 1st theory using an inversion technique based on lowest RMS error for

the average values obtained by fitting theoretical predictions with measured data at different frequencies.

Owing to the different numerical and experimental methods and models, it is hard to acquire a consistent understanding. The literature review shows a lack of work modeling regarding VTI shale fractured rocks. In the discussed studies, each model has specific geometry and crack parameters such as core size, crack shape, crack distribution, distance between cracks and central frequency. All these parameters affect the validation of EMTs and they are not well understood, i.e., the results will be general for shale fractured models but we have to take into account the parameters used. Our objective is to compare our results that are based on certain parameters to what is available in literature. Therefore, we are not only concerned with the calculation of the selected EMT validity threshold regarding crack density and volume concentration as much as we care about comparing our model built using specific parameters with what is available in literature.

iii. Rock Physics Models of Barnet Shale Formation Using Core and Well Log Data Based on EMTs Inversion Technique

Shuai et al. (2020) developed a rock physics model-based scheme to estimate the aspect ratio and shear wave velocity as they are two important parameters for unconventional reservoir characterization and fluid identification. The model takes as input the measured well log data, porosity and mineralogy in the borehole and uses a statistical distribution to obtain the aspect ratio of pores. The Barnett shale model was constructed by comparing the measured data to two effective medium methods: (1) the SCA method performed at high frequency and assumes isolated pore spaces and (2)

SCA-Gassmann method performed at low frequency and describes well connected pore spaces. The results show that V_S is accurately predicted using the high frequency SCA model for the three studied aspect ratio intervals (0.01, 0.1 and 1), while the low frequency SCA-Gassmann assumptions are invalidated. This is explained by the poor in situ characteristics of the Barnet shale formation including pore connectivity and low permeability which allow the low frequency well log velocities to behave as high frequency ones and thus validate the SCA assumptions. Measured velocities from other examples such as the overlying Marble Falls and underlying Ellenburger carbonates validate V_S predicted values with reasonable accuracy by using both the low and high frequency effective methods. This can be related to the strong in situ condition characterized by a higher pore connectivity which makes the sonic frequencies lay within the transition frequencies zone of the two effective methods.

Z. Guo et al. (2013) constructed a rock physics model-based scheme to evaluate specific microstructure properties including porosity, lithology and brittleness index from measured core and well log data and using the most convenient EMTs including SCA and DEM in addition to Backus averaging. The key feature of this model (Figure 12) is related to the importance of compositions and pores' preferred orientations in shales on selecting the best EMT that describes the formation under study.

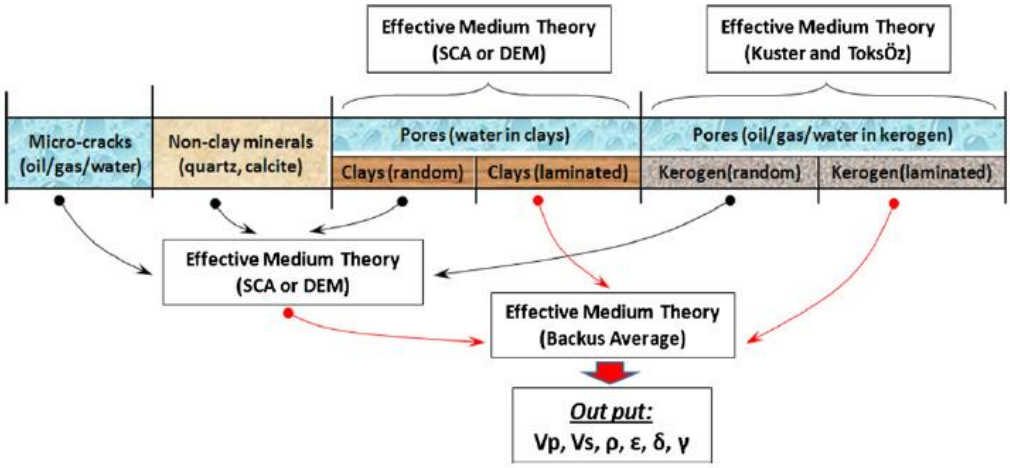

Figure 12 Diagram highlighting the EMT used in the Barnett shale rock physics model Z. Guo et al. (2013)

Measured core and sonic data were used to construct the model and reflect on important properties of the formation. The Poisson's ratio was shown to have a high sensitivity to shales' texture caused by the preferred orientation of clay particles, so it increases with clay content in contrast to the Young's modulus that tends to decrease. The model was applied to predict the microstructure properties based on the calculated AVO (amplitude variation with offset) responses from the top and bottom of the Barnett Shale.

CHAPTER III

METHODOLOGY

- We use the finite element method (FEM) on ABAQUS to calculate the dynamic ultrasonic elastic properties of 3D fractured rocks having a VTI symmetry.
- The accuracy of EMT models (Hudson 1st and 2nd orders, SCA and DEM) is investigated for fractured shale VTI models.
- A benchmark of borehole acoustic modeling using the finite element method (FEM) on COMSOL for fractured VTI rocks is presented.

A. Dynamic Elastic Properties for a VTI Medium

The stiffness matrix of a VTI medium is given by Mavko et al. (2020)

$$\mathbf{C} = \begin{bmatrix} c_{11} & c_{11}-2c_{66} & c_{13} & 0 & 0 & 0 \\ c_{11}-2c_{66} & c_{11} & c_{13} & 0 & 0 & 0 \\ c_{13} & c_{13} & c_{33} & 0 & 0 & 0 \\ 0 & 0 & 0 & c_{44} & 0 & 0 \\ 0 & 0 & 0 & 0 & c_{44} & 0 \\ 0 & 0 & 0 & 0 & 0 & c_{66} \end{bmatrix}, \tag{4}$$

where c_{ij} are the stiffness coefficients.

The five-independent dynamic (ultrasonic) stiffness coefficients c_{ij}^{u} are calculated from the shear ($V_{s,\theta}$) and compressional velocities ($V_{p,\theta}$) as follows

$$c_{33}^{u} = \rho(V_{p,0}^{u})^2, \tag{5}$$

$$c_{44}^{u} = \rho(V_{s,0}^{u})^2, \tag{6}$$

$$c_{11}^{u} = \rho(V_{p,90}^{u})^2, \tag{7}$$

$$c_{66}^{u} = \rho(V_{s,90}^{u})^2, \tag{8}$$

$$c_{13}^{u} = -c_{44}^{u} + \sqrt{\begin{matrix}4\rho^2\left(V_{p,45}^{u}\right)^4 - 2\rho\left(V_{p,45}^{u}\right)^2(c_{11}^{u} + c_{33}^{u} + 2c_{44}^{u}) \\ +(c_{11}^{u} + c_{44}^{u})(c_{33}^{u} + c_{44}^{u})\end{matrix}}, \tag{9}$$

where θ = [0°, 45° or 90°] indicates the incident angle of the wave with respect to the axis of symmetry of the rock, ρ is the average density of the formation and the superscript u denotes ultrasonic simulation.

B. Numerical Modeling: Ultrasonic and Borehole Measurements

1. Ultrasonic Model

a. Model Geometry

The ultrasonic simulations are built on ABAQUS by modeling three-dimensional (3D) fractured rocks connected to a source and a receiver (Figure 13). The wave is excited at the source modeled as a boundary load and detected at the receiver (or set of receivers) after propagating through the solid formation. The source wave is a five-peak burst wavelet with a central frequency, f_c, that ranges from (100 to 500) kHz with a maximum frequency $f_{max} = 2\, f_c$.

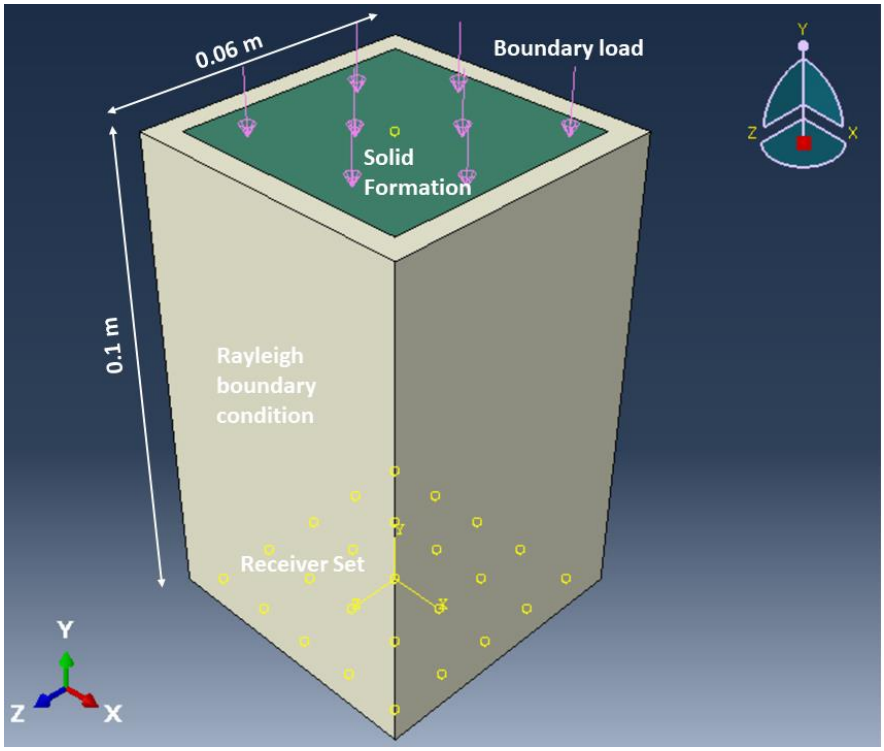

Figure 13 3D ultrasonic model with a boundary load excited in the y- direction

The boundary load is applied in the y- direction (Figure 13) to excite the P-mode, and in the x- or z- direction to excite the S-modes with different polarizations, respectively. The rock is surrounded by a Rayleigh boundary condition to suppress the artificial reflections. The receiver might represent a single point located at the middle of the bottom layer or might be taken as the average of 25 points receivers distributed on the bottom layer as shown in Figure 13.

b. Inclusions' Geometry

The inclusions are modeled either as ellipsoids (Figure 14) or octahedrons (Figure 15). The octahedrons are selected to optimize the simulations in terms of time and to be able to model smaller aspect ratios without facing meshing problems. The inclusions represent a horizontally oriented 3D set. In each direction (x, y, and z), the

same distance between the inclusions' edges is selected so that the resulted set has a homogeneous VTI symmetry.

An ellipse is defined using three semi-axes $a_1, a_2, a_3 \geq 0$. An oblate (penny-shaped) crack has $a_2 = a_3 >> a_1 \geq 0$ and has the following (Grechka, 2005):

- Crack aspect ratio (AR)

$$\alpha = \frac{a_1}{a_2}, \tag{10}$$

- Crack density

$$e = \frac{n\, a_2^3}{V}, \tag{11}$$

- Volume concentration

$$\emptyset = \frac{4}{3}\pi\alpha e, \tag{12}$$

where n is the number of ellipsoids embedded in a rock volume V. AR is chosen to be 0.1 and 0.2 so that the resulted inclusions are oblate.

The EMT are based on the penny-shaped (oblate) ellipsoidal approximations. Therefore, to be able to use octahedrons and still compare the numerical results with the EMTs' models, the volume concentration of the ellipsoids in EMT is taken equal to that of the octahedrons modeled in the FEM.

Note that the effect of crack density on the effective stiffness velocities is known to be much higher than that of volume concentration for rocks having penny-shaped cracks with AR $\leq$ [0.1-0.2] (M. L. Kachanov, Shafiro, & Tsukrov, 2003) .

In this work, we are computing the ultrasonic velocities by changing the volume concentration of octahedrons. In order to compute the EMT analytical solutions that are

based on ellipsoidal approximations, the volume concentration of ellipsoids is assumed to be similar to that of octahedrons and the equivalent crack densities are obtained. The analysis is based on both volume concentration and crack density but the main conclusion is in terms of crack density since it is more important and common to use.

Note that different crack dimensions and aspect ratios might have the same crack density since it only depends on the semi major of the fracture while the volume concentration depends on both the semi major and semi minor of the cracks.

An oblate octahedron has a volume concentration of

$$\emptyset' = \frac{\frac{4}{3}ma_2a_1}{V}, \tag{13}$$

where m is the total number of octahedrons embedded in a rock volume V.

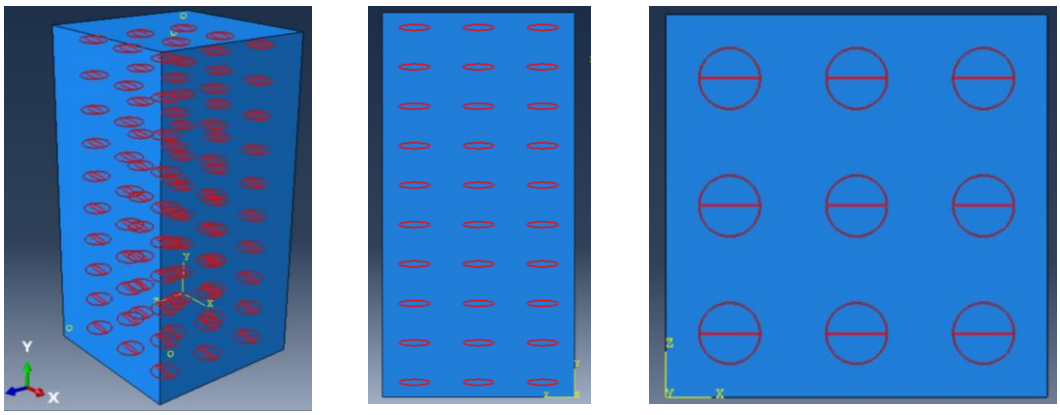

(a) **(b)** **(c)**

Figure 14 Fractured core with an inclusion set oriented horizontally and modeled using ellipsoids (AR=0.2) with a volume concentration and crack density of 1.3% in (a) 3D view, (b) side view and (c) top view

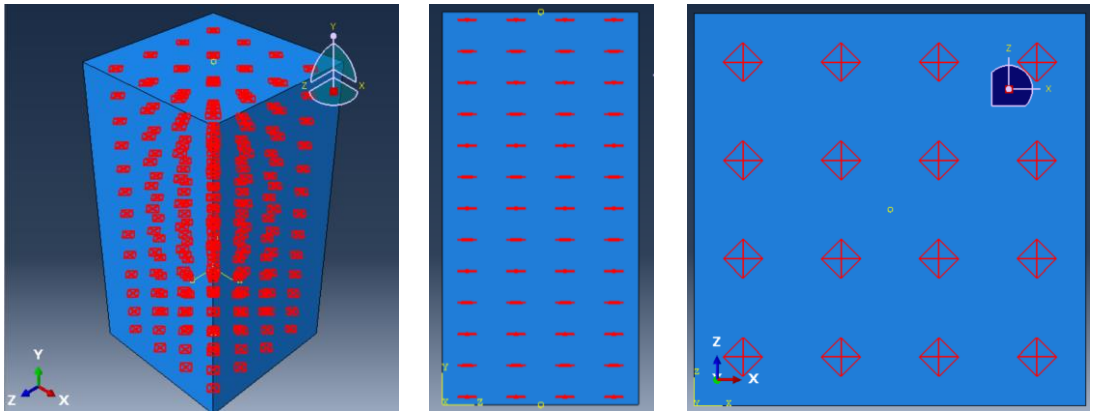

(a) **(b)** **(c)**

Figure 15 Core showing a VTI inclusion set oriented horizontally and modeled using octahedrons (AR 0.1) with a volume concentration of 0.35% and a crack density of 1.3% in (a) 3D view, (b) side view and (c) top view

c. Simulating P-Wave And S-Wave Velocities

In a fractured medium, a load is excited perpendicular and parallel to the fracture sets to calculate the longitudinal (vertical) and transverse (horizontal) P- and S-wave velocities.

The inclusions are titled at an angle of 0° (Figure 16(a)) and 90° (Figure 16(b)) to simulate different polarized P- and S- waves velocities. The resulted effective c_{ij}^{u} can be calculated using Eq. 5 through 9.

To excite a boundary shear load in ABAQUS, a reference point is defined. A point load is applied to the reference point in a certain direction (x or z). This reference point is then linked to the top surface as shown in Figure 17 so that the top surface behaves as a shear boundary load. Otherwise, the only method to define a shear boundary load on the top surface in ABAQUS is by selecting the whole set of nodes which is time consuming.

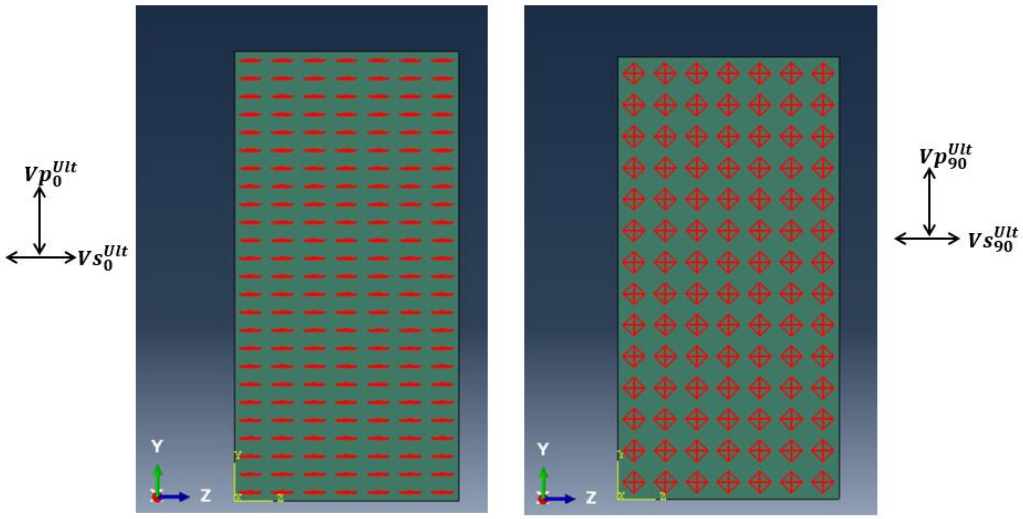

(a) **(b)**

Figure 16 Side views of a 3D fractured rock with (a) 0° and (b) 90° octahedron cracks planes. Black arrows indicate the direction of particle displacement for waves propagating axially through the sample. The volume concentration of octahedrons is (a) 2.04% and (b) 2.12%, respectively

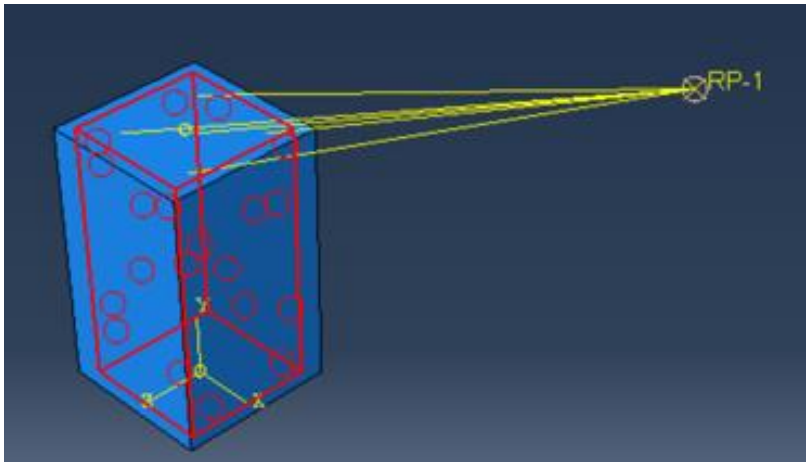

Figure 17 Boundary shear load excitation in ABAQUS using a reference point. The red selected surfaces represent a Tie connection

d. Waveforms and Velocity Calculation

The wave propagation defined using the set of Eq. (16) are solved in the time domain and the single or averaged waveforms calculated at the receivers are used to extract the arrival times of the compressional (P-) and shear (S-) waves and to calculate the effective P- and S- velocities of the 3D fractured rock. Figure 18 shows the arrival times of the P- and S-waves that are obtained by exciting the ultrasonic source in the y- and x-directions, respectively, for a fractured formation composed of octahedron cracks with AR of 0.1, filled with calcite and having a volume concentration of 3.1 % with the material properties defined in Table 2.

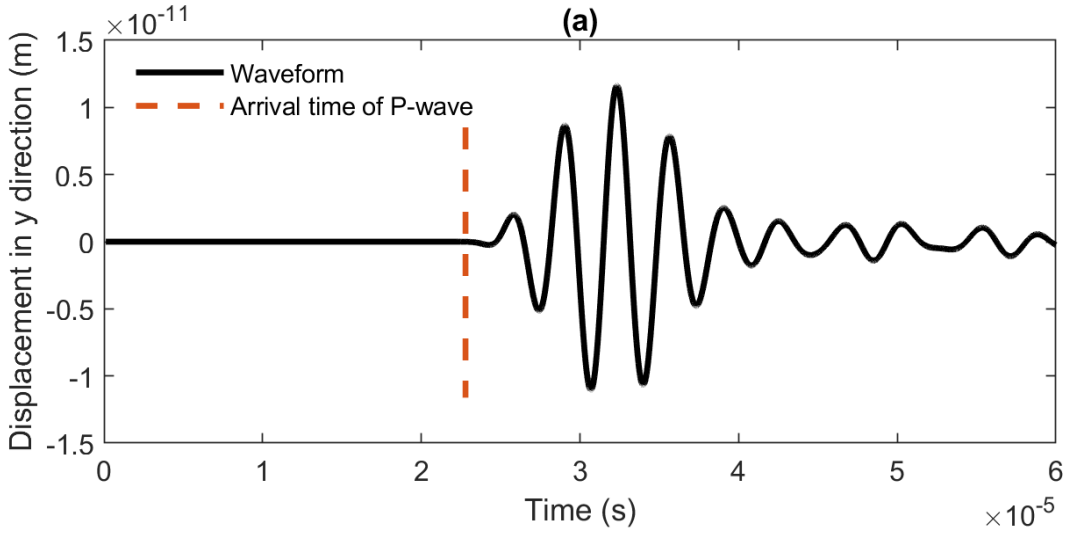

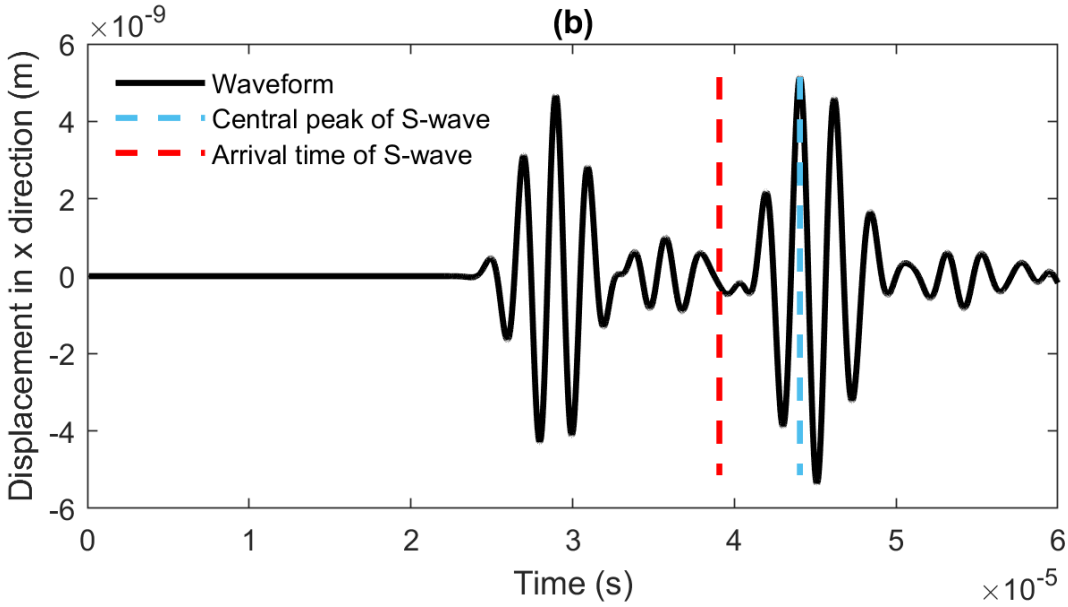

Figure 18 Ultrasonic waveforms obtained with a boundary load source excitation in the (a) y- and (b) x- directions for a VTI fractured rock with octahedrons inclusions filled with calcite, have AR of 0.1 and a volume concentration of 3.1%. The central frequency of the source is (a) 300 kHz and (b) 500 kHz

e. Numerical Validation

The numerical simulation is validated by comparing the computed velocities of an isotropic elastic model to the defined elastic properties and yields a relative error below 2 m/s. Figure 19 shows that the arrival time computed using a specified threshold is almost the same as the one computed analytically using $t_{p,analytical} = \frac{d(distance\ traveled = core\ length)}{V_{p\_Barnet}}$. The fractured model is validated by comparing the FEM ultrasonic results of a fractured model with a single calcite inclusion (AR 0.1) at low crack density to EMT Hudson 1st order analytical value with 1 m/s rms error.

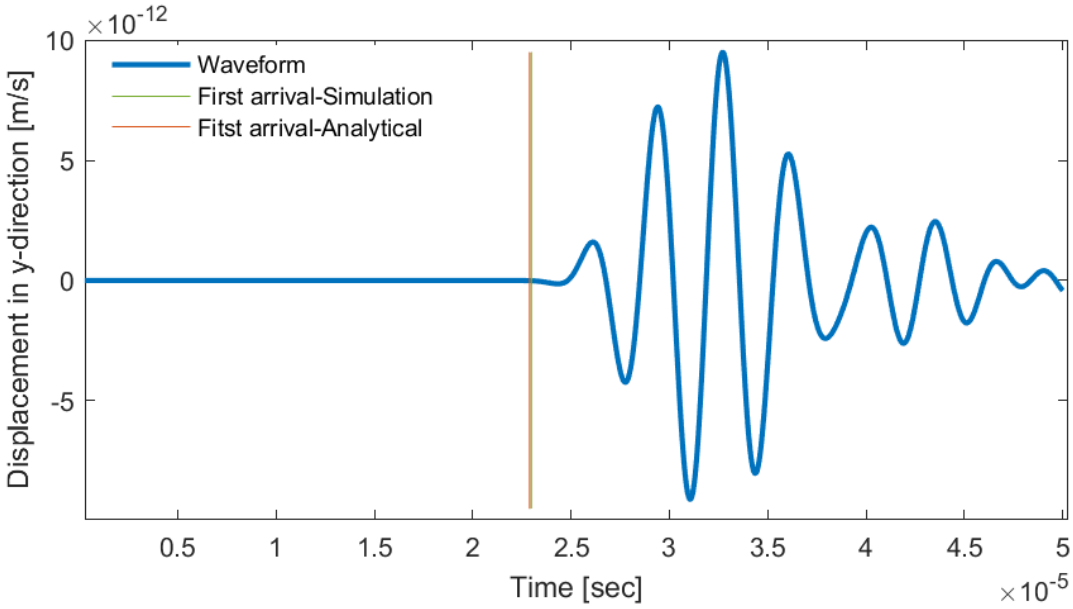

Figure 19 Validation of the numerical model. Reference case (core only without cracks) for a load excited in y- direction with f_c =300 kHz

f. Scattering Parameter

A scattering parameter representing the ratio of the wavelength over crack diameter is defined as

$$\beta_i = \frac{v_i/f_c}{2a_2}, \tag{14}$$

where v_i indicates P-wave or S-wave velocity. β_i is used to validate the condition of EMT methods ($\beta_i > 1$) with $i = p$ for P-wave and $i = s$ for S-wave, respectively. This value is also important to evaluate the scattering mechanisms that might occur. It is also used to check for the EMT applicability condition where the wavelength must be larger than the crack length.

g. Boundary Rayleigh Condition

A Rayleigh boundary condition is added to the core's boundaries (Figure 13) to suppress the reflections. Both Rayleigh damping and the infinite boundary conditions can be used to suppress the reflections at the boundaries. The former is chosen since it simpler to model and provides better mesh quality. The Rayleigh damping method relies on defining an additional material property (Mechanical damping) and is characterized by two types of damping: mass and stiffness damping. In short, mass damping is usually used for "lower" wave frequencies and its effect on simulation time is negligible, while stiffness damping is used for "higher" wave frequencies and has significant effect on computational time. In this work, we use mass damping. The general equation for Rayleigh damping of waves with natural frequency ω_i [rad/s] is given by (ABAQUS documentation 2017)

$$\xi_i = \frac{\alpha_R}{2\omega_i} + \frac{\beta_R \omega_i}{2}, \tag{15}$$

where ξ_i is the fraction of critical damping [unitless], α_R is the mass damping coefficient [rad/s], and β_R is the stiffness damping coefficient [s/rad]. By taking $\xi_i = 1$, the system would be critically damped (overdamped if $\xi_i > 1$) and no noise oscillations would occur. Assuming $\beta_R = 0$ and a natural frequency value of $f_c\pi$ [rad/s], α_R equals $4f_c\pi$ [rad/s] which corresponds to an overdamped system. Since Rayleigh damping is applied as a material property, a thin outer layer part was created (like the infinite elements) and that outer layer alone was damped.

h. Wave Propagation Equation and Explicit Dynamic Analysis in ABAQUS

Elastic wave propagation in the formation and in the absence of body forces, is described with the equations of linear elasticity (P. Matuszyk, Demkowicz, & Torres-Verdín, 2012)

$$\begin{cases} -\nabla . \boldsymbol{\sigma} + \rho_s \frac{\partial^2 \boldsymbol{u}}{\partial t^2} = 0, \\ \boldsymbol{\sigma} = \mathbb{C} : \varepsilon, \\ \varepsilon(\boldsymbol{u}) = \frac{1}{2}(\nabla \boldsymbol{u} + \nabla^T \boldsymbol{u}), \end{cases} \tag{16}$$

where σ is the stress tensor, ε is the strain tensor, u denotes the displacement vector, ρ_s is the solid density, and $\mathbb{C}$ denotes the elastic 4th order compliance tensor. The equations must be accompanied with appropriate boundary and (in the case of an unbounded domain) radiation conditions.

The first equation is Navier's equations and the second equation represents Hook's law which relates the stress to strain via the elastic stiffness coefficients tensor c_{ijkl}. This tensor will be used to define the solid formation and inclusions as linear solids. For a linear isotropic solid, the tensor $\mathbb{C}$ becomes a fourth-order isotropic tensor given by

$$c_{ijkl} = \mu\left(\delta_{ik}\delta_{jl} + \delta_{il}\delta_{jk}\right) + \lambda\delta_{ij}\delta_{kl}, \tag{17}$$

where $\lambda \; and \; \mu$ denote (real) Lamé coefficients that can be defined through characteristic wave speeds in the solid, namely P-wave speed V_p and S-wave speed V_s with a solid density ρ_s. Lamé coefficients are defined as follows:

$$\mu = \rho_s V_s^2, \tag{18}$$

$$\lambda = \rho_s\left(V_p^2 - 2V_s^2\right). \quad (19)$$

i. Explicit Dynamic Analysis (ABAQUS Documentation 2017)

An explicit dynamic analysis is used in ABAQUS to solve the wave propagation equation within the 3D fractured cores.

The explicit dynamics defines a large number of small-time increments and integrates the equations of motion for the body using an explicit central-difference time integration rule. The small-time increments are advantageous since they allow for the solution to be solved without iterations and avoid the need of tangent stiffness matrices. This method is commonly used for wave propagation studies where Abaqus/Explicit can commonly take over 10E5 increments for an analysis. The parallelization procedure is applied to enhance the simulation time.

2. *Borehole Model*

a. Model Geometry

The sonic log technique is simulated by using COMSOL Multiphysics of a water-filled borehole surrounded by a solid formation that can be either homogenous (Figure 20 (a)) or fractured (Figure 20 (b)).

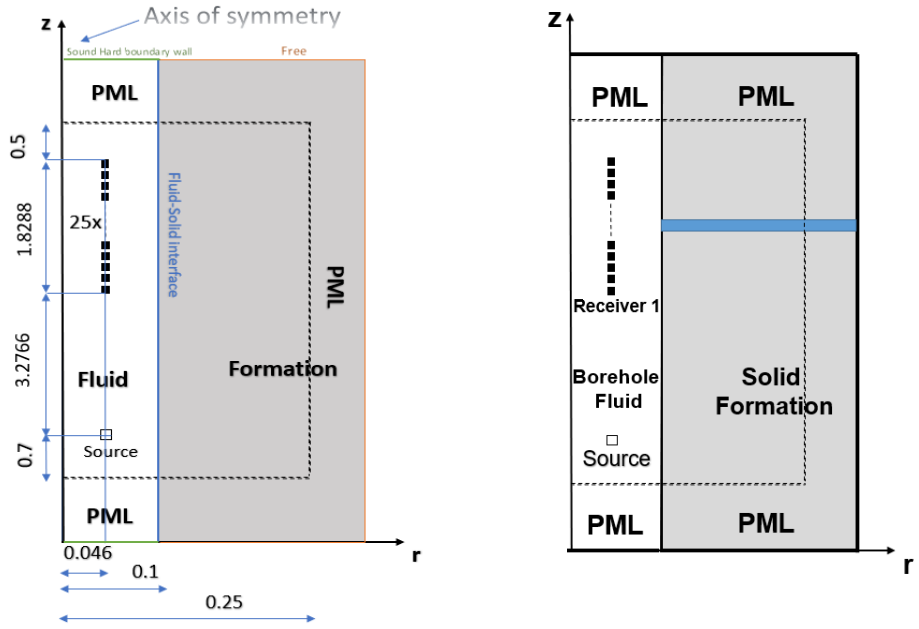

(a) **(b)**

Figure 20 Borehole acoustic model for (a) isotropic and (b) fractured formations. All dimensions are in meter

The borehole includes a wireline tool and a monopole and dipole sources defined using a Ricker wavelet with a central frequency of f_c= 8 kHz and 3kHz respectively and a maximum frequency $f_{max} = 3\ f_c$. The propagation of the acoustic wave in the solid formation domain causes spurious reflections at the boundaries of

domain. To reduce the reflections at the boundaries, a perfectly matched layer (PML) domain that surrounds the formation is defined (P. J. Matuszyk & Demkowicz, 2014).

When using a monopole source, a 2D axisymmetric model (Figure 20) is used to model the sonic tool. For a dipole source, the symmetry is lost and a 3D model (Figure 21) is used to simulate wave propagation. For the 3D dipole model, the PML width does not affect the results. However, a swept mesh with 8 layers is applied to the PML region and boundary layers are added between the domain and the PML with 100 elements per minimum wavelength to obtain accurate results. A symmetry boundary condition in the (x, z) plane and an anti-symmetry boundary condition in the (y, z) plane are added to reduce simulation time and memory.

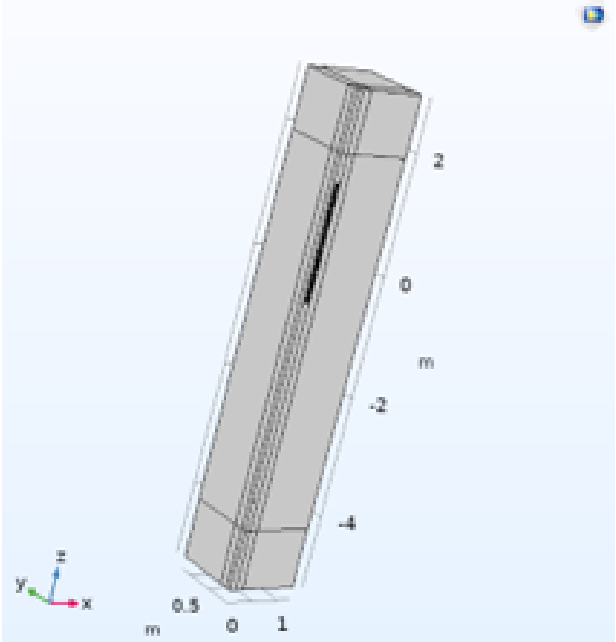

Figure 21 3D Borehole geometry in COMSOL

b. Waveforms and Velocity Calculation

The simulation yields a pressure frequency-spectrum at the receivers. The acquired pressure spectrum measured at the receivers are processed using the Matrix Pencil (MP) method (Ekstrom, 1996) to estimate the dispersive velocity (phase velocity vs. frequency) of the guided waves. Moreover, the spectrum is converted to a time-domain waveform using the inverse Fast Fourier Transform (iFFT). The waveforms are then processed using the Slowness Time Coherence (STC) method (Kimball and Marzetta, 1984) to obtain the shear (V_s) and compressional (V_p) velocities. The numerical simulation is validated using the 1D real-axis integration method.

c. Validation Of 2D Axisymmetric Model Excited By A Monopole Source

An isotropic homogenous formation (fast 1 in Table 2) is simulated by a monopole source in 2D axisymmteric domain. COMSOL FEM results (dots) are compared to the analytical 1D real-axis integration (RAI) solution (circles) for validation (Figure 22). The horizontal green, blue, and red lines represent the borehole fluid velocity, the shear and the compressional velocities of the formation, respectively. The root-mean-square (RMS) error between the FEM modeled phase velocities and the ones obtained using the analytical solution is 0.253 m/s for the compressional (P) mode, 0.0204 m/s for Pseudo Rayleigh (PR) mode, 0.0034 m/s for higher Pseudo Rayleigh (PR 1) mode and zero for Stoneley (ST) mode.

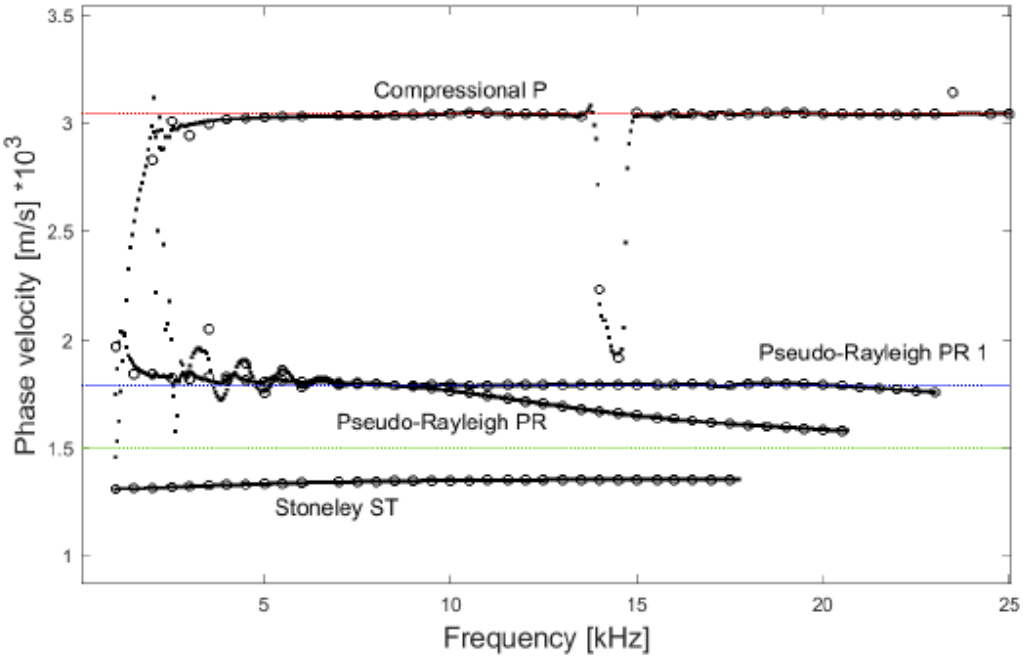

Figure 22 Comparison of the dispersion curve obtained using the 1DRAI method (circles) to the one obtained using COMSOL FEM (dots) for discrete frequencies from 50 Hz to 25 kHz for the isotropic formation defined in Table 2

The pressure spectrum obtained at the receivers is post processed using an iFFT code and the resulted waveform is compared to the one obtained using an analytical 1D real-axis integration (RAI) technique (Figure 23) which shows a perfect fit.

The waveforms obtained at the receivers are then processed using the STC technique to calculate the slowness profile (Figure 24) of each mode that yields velocity estimations with a relative error below 2%.

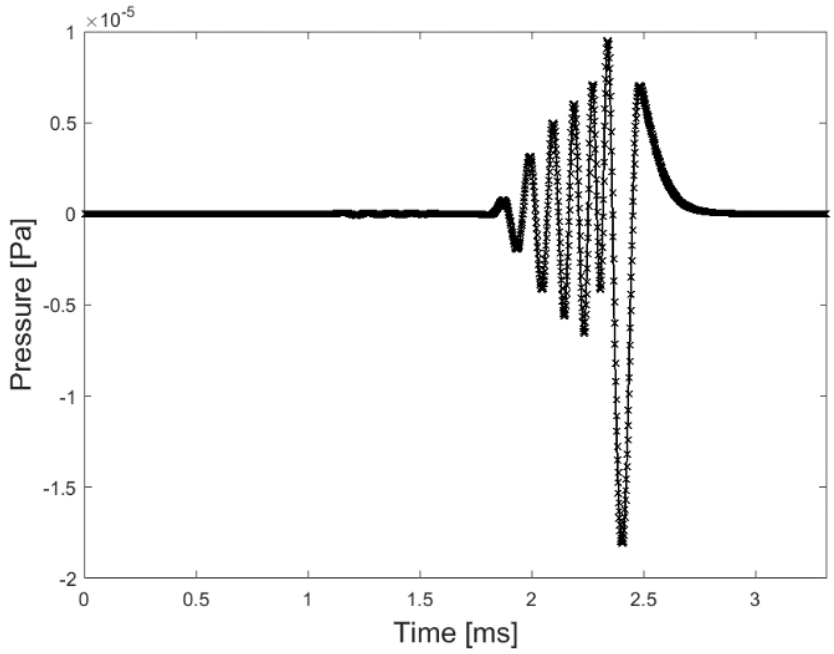

Figure 23 Comparison of the waveform obtained using the 1DRAI method (crosses) to the one obtained using the COMSOL (line) for an isotropic fast 1 formation defined in Table 2

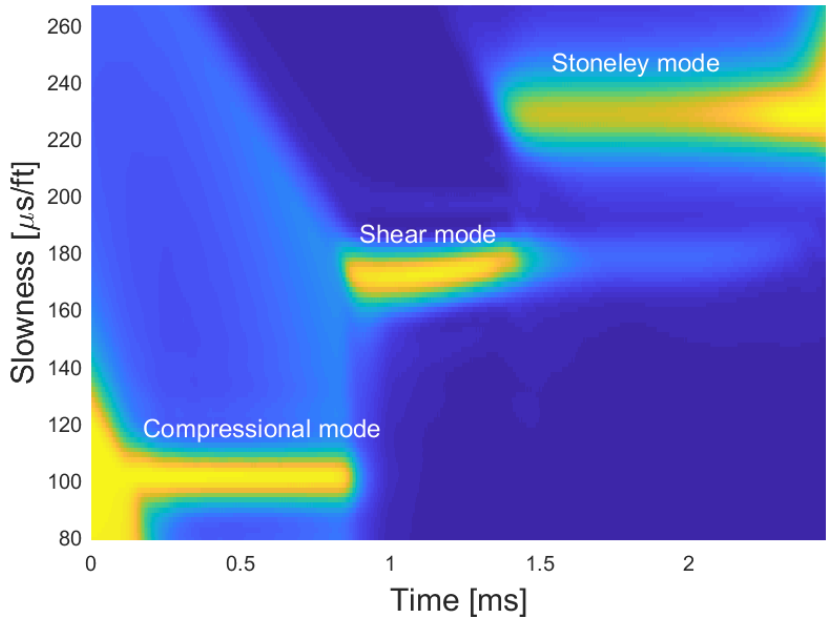

Figure 24 STC coherence map for an isotropic fast 1 formation defined in Table 2

d. Validation Of 3D Model Excited by A Dipole Source

An isotropic homogenous formation (fast 1 in Table 2) is simulated by a dipole source in 3D domain. Figure 25 shows a comparison of the dispersion curve of the flexural mode obtained using the analytical 1DRAI method (dots) to the one obtained using COMSOL FEM (stars) for discrete frequencies from 100 Hz to 5 kHz. The horizontal red line is the shear velocity of the formation. The RMS error for flexural mode is 1.901 m/s for selected discrete frequencies above 1 kHz.

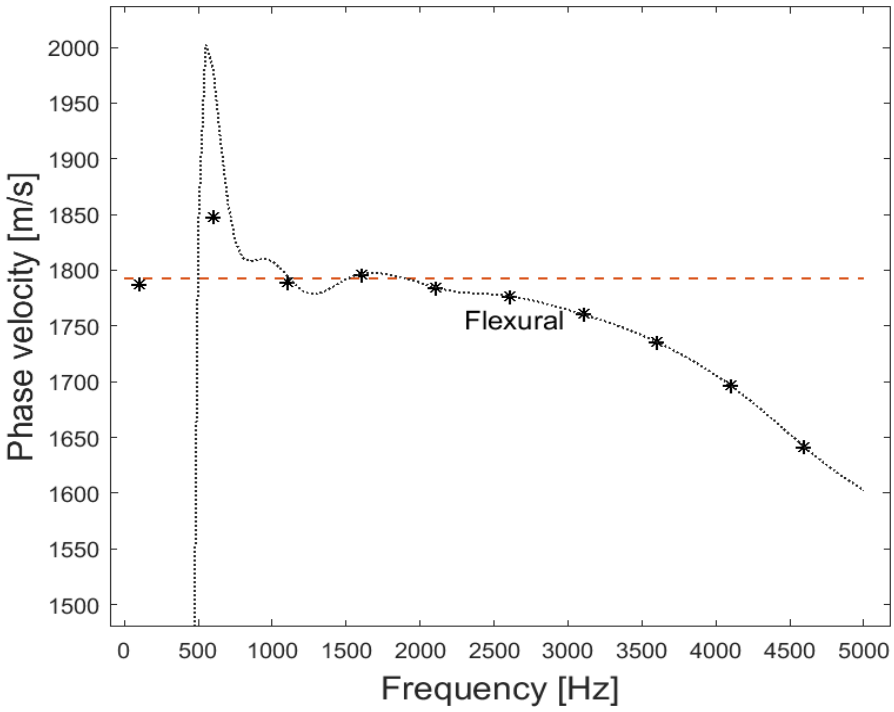

Figure 25 Comparison of the dispersion curve obtained using the 1DRAI method (dots) to the one obtained using COMSOL FEM (stars) for discrete frequencies from 100 Hz to 5 kHz for the isotropic fast 1 formation defined in Table 2

3. Numerical parameters

a. Mesh Element Size

The FEM subdivides the modeling domain into smaller, simpler domains called elements. A trial-and-error analysis is performed to select the optimal mesh element size needed to obtain accurate results while reducing the computational memory and time. The minimum mesh element size in the x, y, and z directions are chosen for the isotropic fractured elastic simulations as: $\Delta_x, \Delta_y, \Delta_z \leq \frac{V_{min}}{q\ f_{max}}$ where V_{min} is the minimum velocity in the domain and f_{max} is the maximum dominant frequency in the source spectrum (Maalouf & Torres-Verdín, 2018). The number of elements per minimum wavelength is q =[5-10] which is chosen according to the complexity of the model and following a sensitivity analysis. The PML is meshed using 8 layers.

b. Mesh Quality

Ultrasonic using ABAQUS: using small mesh element size induces mesh quality warnings (typically < 0.2%). An anti-distortion and deletion options are activated as part of mesh control to remove the elements once they satisfy the distortion criteria.

Borehole using COMSOL: the minimum element quality based on the skewness method is approximately 0.51 and the average element quality is around 0.95 for most of the cases which is very close to 1 and indicates a good mesh.

c. Mesh Element Type and Order

Ultrasonic using ABAQUS: A tetrahedral mesh must be used to mesh the core embedded with fractures and hexagonal elements are used for the outer Rayleigh layer.

The element order used is linear. Since dissimilar mesh element types are used, a Tie constraint (Figure 17) must be added between the two surfaces to avoid relative motion between them (ABAQUS documentation 2017).

Borehole using COMOSL: each domain is defined in terms of the element type/order and shape function used in the simulations as listed in Table 1.

Table 1 Element type/order and shape function for each domain

Domain	**Element type**	**Element order**	**Shape function type**
PML Acoustic	Quadrilateral	Second order (Quadratic)	Lagrange
PML Solid	Quadrilateral	Second order (Quadratic)	Nodal serendipity
Acoustic domain	Triangular	Second order (Quadratic)	Lagrange
Solid elastic domain	Triangular	Second order (Quadratic)	Nodal serendipity

d. Frequency and Time Steps

Ultrasonic using ABAQUS: in time domain simulations, the time step is given by

$$\Delta_t = \frac{1}{w\, f_{max}}, \tag{20}$$

with w =[60-100] and the value of w depends on the complexity of the model and obtained following a sensitivity analysis.

The central frequency of the source for calculations related to the P-wave velocity is f_c= [100,300] kHz, while ta for the S-wave velocities is $f_c = [400,500]$ kHz.

The f_c selected must provide a wavelength that is larger than the crack length so that the comparison to the EMT analytical solutions is applicable.

Borehole using COMOSL: to apply an iFFT and transform the frequency spectrum to time domain waveforms, a frequency step of $\Delta_\omega = 50\ Hz$ is used for $f_c = 8kHz$ (monopole source) and $\Delta_\omega = 25\ Hz$ is used for $f_c = 3kHz$ (dipole source).

e. ABAQUS vs. COMSOL

In case the inclusions (fractures) are defined using weak properties, in ABAQUS, the core merged with the inclusion must be meshed using the smallest element size, however, in COMSOL, it is easier to select independent mesh element sizes for different regions without the need to connect them with a Tie connection like in ABAQUS. COMSOL however requires computationally expensive simulations because it solves the equation for a large set of parameters compared to ABAQUS where the output parameters are selective (user-defined).

f. Accuracy and Limitation of Numerical Modeling

To ensure accurate results, sensitivity analysis is performed to select mesh size and time step for each model. However, the high computational time and the mesh complexity might prevent the use of very small-time step (or automatic) or very fine mesh size.

C. EMT Models: Equations for VTI Anisotropic

The effective elastic properties (i.e., the effective stiffness coefficients, c_{ij}, and effective velocities, $V_{s,\theta}$ and $V_{p,\theta},$) of a heterogeneous medium are approximated using

the effective medium theories. The mathematical models of each method (Hudosn 1st and 2nd, DEM and SCA) are described below.

1. Hudson 1st and 2nd Order Models

Hudson (1980, 1981) derived the effective elastic properties by analyzing the mean wavefield in an elastic solid background embedded with thin, penny-shaped ellipsoidal cracks using a scattering-theory analysis. The effective stiffness coefficients, c_{ij}, are given as

$$c_{ij}^{eff} = c_{ij}^{0} + c_{ij}^{1} + c_{ij}^{2}, \tag{21}$$

where c_{ij}^{0} belongs to the isotropic background and c_{ij}^{1}, c_{ij}^{2} account for 1st and 2nd order corrections, respectively (Mavko et al., 2020).

The transverse isotropic symmetry (VTI) model is derived by Hudson for a crack set with the normal directions aligned along the 3-axis, the 1st (c_{ij}^{1}) and 2nd (c_{ij}^{2}) corrections are

$$c_{11}^{1} = -\frac{\lambda^2}{\mu}\varepsilon U_3, \tag{22}$$

$$c_{11}^{2} = \frac{q}{15}\frac{\lambda^2}{(\lambda+2\mu)}(\varepsilon U_3)^2, \tag{23}$$

$$c_{13}^{1} = -\frac{\lambda(\lambda+2\mu)}{\lambda}\varepsilon U_3, \tag{24}$$

$$c_{13}^{2} = \frac{q}{15}\lambda(\varepsilon U_3)^2, \tag{25}$$

$$c_{33}^{1} = -\frac{(\lambda+2\mu)^2}{\mu}\varepsilon U_3, \tag{26}$$

$$c_{33}^{2} = \frac{q}{15}(\lambda+2\mu)(\varepsilon U_3)^2, \tag{27}$$

$$c_{44}^{1} = -\mu\varepsilon U_1, \quad (28) \qquad c_{44}^{2} = \frac{2}{15}\frac{\mu(3\lambda+8\mu)}{(\lambda+2\mu)}(\varepsilon U_1)^2, \quad (29)$$

$$c_{66}^{1} = 0, \quad (30) \qquad c_{66}^{2} = 0, \quad (31)$$

where

$$q = 15\frac{\lambda^2}{\mu^2} + 28\frac{\lambda}{\mu} + 28, \quad (32)$$

$$\varepsilon = \frac{N}{V}a^3 = \frac{3\emptyset}{4\pi\alpha} = crack\ density, \quad (33)$$

where λ and μ are the elastic moduli for the isotropic background, a and α are crack radius and aspect ratio, respectively.

The terms U_1 and U_3 depend on the elastic properties of the inclusions. For "dry" cracks

$$U_1 = \frac{16\ (\lambda+2\mu)}{3\ (3\lambda+4\mu)}, \quad (34) \qquad U_3 = \frac{4\ (\lambda+2\mu)}{3\ (\lambda+\mu)}, \quad (35)$$

The weak condition is satisfied when it is of the order of 1 and cannot be neglected and is give by

$$\frac{\mu\alpha}{K' + \frac{4}{3}\mu'}, \quad (36)$$

Thus, the shape or aspect ratio as well as the relative moduli of the inclusion with respect to matrix material, all are criteria for an inclusion to be considered as weak. For "weak" inclusions

$$U_1 = \frac{16\,(\lambda+2\mu)}{3\,(3\lambda+4\mu)}\frac{1}{(1+M)}, \quad (37) \qquad U_3 = \frac{4\,(\lambda+2\mu)}{3\,(\lambda+\mu)}\frac{1}{(1+\kappa)}, \quad (38)$$

where

$$M = \frac{4\mu'}{\pi\alpha\mu}\frac{(\lambda+2\mu)}{(3\lambda+4\mu)}, \quad (39) \qquad \kappa = \frac{(K'+\frac{4}{3}\mu')(\lambda+2\mu)}{\pi\alpha\mu\,(\lambda+\mu)}, \quad (40)$$

where K' and μ' define the bulk and shear modulus of the inclusion material.

2. Differential Effective Medium (DEM) Model

The differential effective medium (DEM) theory computes the effective stiffness coefficients for of a two-phase mixture by incrementally adding inclusions defined as phase 2 to a host rock defined as phase 1 until a desired concentration x_2 of phase 2 is reached (Bandyopadhyay, 2009; Sayar, 2015).

The effective stiffness tensor C_{DEM} is given by (Jakobsen, Hudson, Minshull, & Singh, 2000)

$$(1-x)\frac{d}{dx}[C_{DEM}(x)] = (C_2 - C_{DEM})Q_{DEM_2}(x), \quad (41)$$

where x is volumetric concentration of the inclusion defined with phase 2, Q is geometric shape factor (Appendix A) with subscript DEM_2 indicates that Q is evaluated for an inclusion of phase 2 embedded in a background matrix with an effective stiffness tensor C_{DEM}, C_2 is the stiffness tensor of the inclusion material (phase 2) and C_{DEM} is stiffness tensor of the effective medium at every iteration.

The DEM calculates the effective properties at every iteration by defining the matrix using the previously calculated effective stiffness coefficients. At the first increment, when the matrix has no inclusions ($x = 0$), $C_{DEM}(x = 0) = C_1$ where C_1 is

the stiffness tensor of the initial host rock (phase 1). To account for rocks having more than 2 phases, several steps are needed to reach the final effective elastic properties of the mixture while at each step a new phase is added to the medium. The new phase is randomly selected which limits the ability of this method to describe real rock evolution.

3. Isotropic Self-Consistent Approximation (SCA) Model

The isotropic self-consistent approximation (SCA) model estimates the effective stiffness tensor of an N-phase mixture using

$$\sum_{i=1}^{N} x_i (C_i - C_{SCA}) Q_{SCA_i} = 0, \tag{42}$$

where x_i is the volumetric concentration of inclusion i, Q is the geometric shape factor (Appendix A) with subscript SCA_2 indicates that Q is evaluated for an inclusion of material i embedded in a background matrix with an effective stiffness tensor C_{SCA} (Bandyopadhyay, 2009; Sayar, 2015).

D. RMS Error

The root-mean-square (RMS) error is used to measure the difference between the numerical models and the EMT and to identify the volume concentration threshold that yields divergence to the EMT. The modeled velocities are obtained from post processing numerical results (ultrasonic or Well logging) and the analytical velocities are obtained using the EMT approximations or the 1D-real axis integration method for the ultrasonic and borehole measurements, respectively. The RMS error is expressed as

$$RMS\ error = \sqrt{\frac{\sum_i^{N_L}(v_i^{actual} - v_i^{modeled})^2}{N_L}}, \tag{43}$$

where N_L is the total number of discrete phase velocities, v_i^{actual} is the i-th phase velocity value of the actual (analytical) results, and $v_i^{modeled}$ is the i-th phase velocity value of the modeled (numerical) results.

E. Summary Plan for Ultrasonic Modeling and Analysis

- The VTI fracture set is built using a MATLAB code based on a specific aspect ratio and volume concentration or crack density.
- The fractures are shaped as ellipsoids or octahedrons and the orientation is specified to compute a specific polarized velocity.
- The VTI fractured rock is modeled by embedding the inclusions in the matrix using a MATLAB code.
- Material properties are defined for matrix and inclusions. The matrix is defined using elastic Barnet shale properties and embedded with dry, weak or calcite filled inclusions modeled using void, elastic slow and elastic fast formations, respectively.
- An outer layer is added to model the Rayleigh boundary condition needed to suppress artificial reflections.
- A boundary load source is defined using a specific central frequency and the polarized direction is specified.
- The mesh element type and size are specified and a Tie connection between different mesh types is added.

- Simulation parameters including time step and parallelization technique are specified and the final waveforms are computed on the receivers.
- The waveforms are used to extract the effective velocities using calibrated first arrival and central peak analysis.
- Analytical effective elastic properties obtained using the EMTs models coded on MATLAB are compared to ultrasonic measurements.
- The accuracy of the EMT methods is evaluated by calculating the RMS error.

CHAPTER IV

RESULTS AND ANALYSIS

This chapter includes synthetic cases of fractured formations. The cases presented are as follows:

Section 1: Ultrasonic measurements (fractured Barnet shale)

- Comparison of octahedron vs. ellipsoidal cracks: AR=0.2, calcite filled and dry cracks.
- Example 1: Octahedron shaped cracks, AR=0.1, calcite filled cases.
- Example 2: Octahedron shaped cracks, AR=0.1, dry case.
- Example 3: Octahedron shaped cracks, AR=0.1, slow (weak) material filled cases.
- Comparison of results for cracks of AR=0.1 vs. AR=0.2: octahedrons cracks, calcite filled and dry cases.

Section 2: Borehole measurements (fractured and layered Marcellus shale)

- Example 1: Effect of single fracture location on ultrasonic and borehole compressional velocity.
- Example 2: Effect of fracture layer thickness in a VTI medium on ultrasonic and borehole compressional velocity.

In section 1, dynamic ultrasonic properties are estimated for three types of fractured formations. The three examples include a fractured rock defined with a Barnet Shale matrix embedded with horizontally oriented inclusions modeled as octahedrons.

The inclusions have an aspect ratio (AR) of 0.1 and are filled with calcite (Example 1), dry (Example 2) or filled with a slow material (Example 3). The fractured formations are approximated as VTI and are compared to EMT analytical solutions for VTI models.

At first, the effect of crack shape (ellipsoids vs. octahedrons) on elastic properties is addressed for fractures having an AR of 0.2 and that are either dry or filled with a calcite material.

Finally, a comparison between AR = 0.1 and AR = 0.2 is discussed for dry or calcite filled cracks.

In section 2, dynamic borehole properties are presented for a fractured rock excited with a monopole source. The elastic properties are taken from the Marcellus Shale formation and the rock is embedded with a horizontal water filled fracture. Tables 2 to 7 summarize different modeling parameters as follows:

- The formation properties are summarized in Table 2 for ultrasonic (core analysis) models and in Table 3 for borehole (well logging) models.
- The dimension of the core is 50 mm×100 mm×50 mm with inclusions having dimensions listed in Table 4.
- The workflow to obtain the results from ultrasonic and borehole acoustic measurements is described in Table 5.
- The ultrasonic simulations conditions are summarized in Table 6.
- The crack distribution for each ultrasonic model is listed in Table 7.
- The RMS values between computed ultrasonic results and estimated EMTs' values are listed in Table 8. The value of the crack density threshold that yield a divergence between the numerical models and the EMT ae included in the table.

Note that the terms cracks, inclusions or fractures are used interchangeably without any dimension preference.

Table 2 Formation and inclusions' properties for ultrasonic (core analysis) models

Model	**Formation**	**Formation Properties**	**Inclusion**	**Inclusion Properties**
Core analysis "Ultrasonic modeling"	Barnet Shale	ρ_1= 2430 kg.m^{-3} V_{p1}= 4368.4 m.s^{-1} V_{s1}= 2586.8 m.s^{-1}	Calcite	ρ_2= 2710 kg.m^{-3} V_{p2}= 6672.7 m.s^{-1} V_{s2}= 3432.5 m.s^{-1} $\boldsymbol{\gamma = 0.0135}$
			Dry	ρ_3= 0 kg.m^{-3} V_{p3}= 0 m.s^{-1} V_{s3}= 0 m.s^{-1} $\boldsymbol{\gamma =}$ **7.013 (Dry compared to a weak material with** $\boldsymbol{(E = \frac{E,Barnet}{200})}$ *Simulated as void
			Slow (weak)	ρ_4= 1100 kg.m^{-3} V_{p4}= 1300 m.s^{-1} V_{s4}= 800 m.s^{-1} $\boldsymbol{\gamma = 0.875}$

* γ: Hudson condition 2 (Eq. 36) , must be of the order of 1 for a material to be considered as weak

Table 3 Formation and inclusions' properties for borehole (well logging) models

Model	**Formation or Layers**	**Properties**	**Borehole fluid**	**Properties**
Well Logging "Borehole modeling"	Marcellus Shale	ρ_5= 2580 kg.m^{-3} V_{p5}= 2917 m.s^{-1} V_{s5}= 1804 m.s^{-1}	Water	ρ_f = 1000 kg.m^{-3} V_f = 1500 m.s^{-1}
	Isotropic Fast 1	ρ_6= 2200 kg.m^{-3} V_{p6}= 3048 m.s^{-1} V_{s6}= 1793 m.s^{-1}		
	Isotropic Fast 2	ρ_7= 2300 kg.m^{-3} V_{p7}= 4354 m.s^{-1} V_{s7}= 2621 m.s^{-1}		

Table 4 Crack dimensions

Crack Aspect ratio, α	**Semi-Minor, a_1 [m]**	**Semi-Major, a_2 [m]**	**Shape**	**Core length/crack length**
0.2	0.0008	0.004	Oblate	12.5
0.1	0.00025	0.0025	Oblate	20
0.05	0.00025	0.005	Oblate	10

The scale effect is represented by the ratio of core length to crack length. A ratio of 20 or above is needed to obtain robust results between different velocity acquisition

methods (dynamic and static) and to validate EMT assumptions (DEM) (Saenger et al., 2006).

Table 5 Workflow used to compute the elastic properties using ultrasonic and borehole acoustic measurements

Method	**Simulated data**	**Properties calculated from data**	**Other derived properties**
Ultrasonic	Waveform at the point or average receiver/s	V_p from first arrival and V_s from central peak of the waveform	c_{33} (Eq.5) c_{44} (Eq. 6)
Borehole Acoustic	Waveforms at the receiver array of the tool	V_p and V_s from the STC method	

Table 6 Ultrasonic simulations conditions

Model #	**Matrix material**	**Crack material**	**Crack AR, α**	**f_c, kHz**	**Wavelength $\lambda_i = \frac{c_{i\,(Barnet)}}{f_c}$ (m)**	**Wave-length/ crack diameter, $\beta_i = \frac{\lambda_i}{2a_2}$**	**Core length/λ_i, $\delta_i = \frac{L}{\lambda_i}$**	**Time step, sec**	**[Max., Min.] or fixed mesh element size, m (the % in some cases refer to mesh quality warnings)**	**Receiver type: Single point (SP) or Multiple point receivers (MP)**	**Computed velocity**
1	Barnet	Calcite	0.2	300	λ_p: 0.015	β_p: 1.82	$\boldsymbol{\delta_p}$: 6.87	1.5e-8	0.00086, 0.00075	SP	$V_{p,0}^u$
2	Barnet	Dry	0.2	300	λ_p: 0.015	β_p: 1.82	$\boldsymbol{\delta_p}$: 6.87	2e-8	0.00086	SP	$V_{p,0}^u$
3	Barnet	Calcite	0.1	300	λ_p: 0.015	β_p: 2.91	$\boldsymbol{\delta_p}$: 6.87	1.5e-8	0.00086, 0.0005 (0.0005%)	SP	$V_{p,0}^u$
4	Barnet	Calcite	0.1	300	λ_p: 0.015	β_p: 2.91	$\boldsymbol{\delta_p}$: 6.87	1.5e-8	0.0005 (0.0002%)	SP	$V_{p,90}^u$

5	Barnet	Calcite	0.1	500	λ_s: 0.0052	β_s: 1.035	$\boldsymbol{\delta_s}$: 19.33	1.2e-8	0.00086, 0.0005 (0.0005%)	SP	$V_{s,0}^u$
6	Barnet	Calcite	0.1	500	λ_s: 0.0052	β_s: 1.035	$\boldsymbol{\delta_s}$: 19.33	1.2e-8	0.0005 (0.0002%)	SP	$V_{s,90}^u$
7	Barnet	Dry	0.1	300	λ_p: 0.015	β_p: 2.91	$\boldsymbol{\delta_p}$: 6.87	1.2e-8	0.0004	SP & MP	$V_{p,0}^u$
*8	Barnet	Dry	0.1	300	λ_p: 0.015	β_p: 2.91	$\boldsymbol{\delta_p}$: 6.87	1.5e-8	0.0004	SP	$V_{p,0}^u$
9	Barnet	Dry	0.05	300	λ_p: 0.015	β_p: 1.46	$\boldsymbol{\delta_p}$: 6.87	8e-9	0.0004	MP	$V_{p,0}^u$
10	Barnet	Slow	0.1	100	λ_p: 0.044	β_p: 8.74	$\boldsymbol{\delta_p}$: 2.29	2.5e-8	0.0005, 0.0004	SP	$V_{p,0}^u$
11	Barnet	Slow	0.1	400	λ_s: 0.0065	β_p: 1.29	$\boldsymbol{\delta_p}$: 15.38	2e-8	0.0004	SP & MP	$V_{s,0}^u$
12	Barnet	Slow	0.05	100	λ_p: 0.044	β_p: 4.368	$\boldsymbol{\delta_p}$: 2.29	2.5e-8	0.0004 (6.01%)	SP	$V_{p,0}^u$
13	Barnet	Slow	0.1	400	λ_p: 0.01	β_p: 2	$\boldsymbol{\delta_p}$: 10	2e-8	0.0004	MP	$V_{p,0}^u$

- δ_i: Highlights the effect of wavelength compared to core length.
- The models are all excited using a boundary load.
- β_i: defined using (Eq. 14) and indicates the validity of EMT assumption since all values >1.

*Model 8 for alternating cracks.

Table 7 Cracks (VTI set) distribution parameters

Model # in Table 6	**Max. number of cracks, *N* (VTI set)**	**Crack Shape**	**[Min., Max.] distance between cracks, $[d_1, d_2]$ in m**	$\frac{\lambda_i}{d_1}, \frac{\lambda_i}{d_2}$	**Validity of Hudson condition 1 ($\frac{\lambda_i}{d_{1,2}}$ >1)**	**Volume concentration range, VC %**	**Crack density range, CD %**
1, 2	700	Ellipsoids	0.0045, 0.042	3.24, 0.35	First two points not valid	10.43	12.44
1, 2	550	Octahedrons	0.002, 0.048	7.28, 0.303	Two points only valid including last one	7.5	14.08
3	2560	Octahedrons	0.0021, 0.045	7.14, 0.33	-	4.27	16

4	2625	Octahedrons	0.0015, 0.045	10, 0.33	-	4.38	16.4
5	2560	Octahedrons	0.0021, 0.045	2.48, 0.12	-	4.27	16
6	2625	Octahedrons	0.0015, 0.045	3.47, 0.12	-	4.38	16.4
7	1862	Octahedrons	0.0021, 0.045	7.14, 0.33	First two points not valid	3.1	14.81
8	1862	Octahedrons	0.0021, 0.0013	7.14, 11.54	All valid	3.1	14.81
9	880	Octahedrons	0.0013, 0.0025	11.54, 6	All valid	5.87	44
10	4928	Octahedrons	0.0008, 0.045	54.605, 0.97	Only first fractured case not valid	8.21	30.8
11	4928	Octahedrons	0.0008, 0.045	8.084, 0.14	Only first fractured case is not valid	8.21	30.8
12	880	Octahedrons	0.0013, 0.0025	33.6, 17.47	All valid	5.87	44
13	936	Octahedrons	0.0075	1.46	Valid	1.56	5.85

- CD refers to the crack density value calculated using (Eq. 11). For octahedrons cracks, the CD is calculated by assuming the number of ellipsoids equals to that of octahedrons (N) with same aspect ratio (α).
- Hudson condition 1 is only analyzed for cases where Hudson is applicable (for dry or weak cracks), it indicates that the wavelength must be greater than the distance between cracks for Hudson to be valid.

Table 8 Ultrasonic results: RMS errors and selected EMT method with specified threshold

Background material, Crack material, Crack shape, Crack AR, Computed Velocity	**Model # in Table 6**	**EMT, RMS (m/s)**				**Selected EMT, Best fit**	**Validity of EMT "Max. CD %- Max. VC%"**	**Threshold for selected EMT "point of deviation"**
		SCA	**DEM**	**H1 Hudson 1st**	**H2 Hudson 2nd**			
Barnet, Calcite, Elli., 0.2, $V_{p,0}^{u}$	1	36.85 w/o last point: 13.9		-	-	SCA & DEM	CD:14.08% VC:7.5%	CD: 5.32% VC: 2.84%
Barnet, Calcite, Oct., 0.2, $V_{p,0}^{u}$	1	16.86		-	-	SCA & DEM	CD:12.44% VC:4.05%	CD: 1.61% VC: 0.86%
Barnet, Dry, Elli., 0.2, $V_{p,0}^{u}$	2	207.39	206.8	273.52	81.701	H1	CD: 1.34% VC: 1.34%	CD: 1.34% VC: 1.34%

Barnet, Dry, Oct., 0.2, $V_{p,0}^{u}$	2	197.87	235.61	189.85	104.805	H1	CD: 1.61% VC: 0.86%	CD: 1.61% VC: 0.86%
Barnet, Calcite, Oct., 0.1, $V_{p,0}^{u}$	3	8.95		-	-	SCA &DEM	CD: 16% VC: 4.27%	CD: 2.96% VC: 0.79%
Barnet, Calcite, Oct., 0.1, $V_{p,90}^{u}$	4	22.33		-	-	SCA &DEM	CD: 16.4% VC: 4.37%	CD: 3.78% VC: 1%
Barnet, Calcite, Oct., 0.1, $V_{s,0}^{u}$	5	4.65		-	-	SCA &DEM	CD: 16% VC: 4.27%	CD: 2.96% VC: 0.79%
Barnet, Calcite, Oct., 0.1, $V_{s,90}^{u}$	6	6.28		-	-	SCA &DEM	CD: 16.4% VC: 4.37%	CD: 3.78% VC: 1%
Barnet, Dry, Oct., 0.1, $V_{p,0}^{u}$	7	260.0	268	177.5	130.18	H1	CD: 0.51% VC: 0.14%	CD: 0.51% VC: 0.14%
Barnet, Slow, Oct., 0.1, $V_{p,0}^{u}$	10	209.98	215.82			DEM	CD: 1.3% VC: 0.35%	CD: 0.5% VC: 0.14%
				291.68	147.73	H1		CD: 1.3% VC: 0.35%

Barnet, Slow, Oct., 0.1, $V_{s,0}^{u}$	11	28.25	31.08	30.32	37.92	H1	CD: 11.6% VC: 3.1%	CD: 11.6% VC: 3.1%
						SCA	CD: 30.8% VC: 8.21%	After VC 3.1% for MP results

- The threshold given is the table was obtained using the simulated data points. More data points might yield higher thresholds for the validly of EMT. The threshold is selected when the relative difference with the selected EMT solution is below 50 m/s.
- RMS are only presented for runs including ranges of different volume concentrations, single trails relevant to one value of volume concentration are discussed within the text.
- The validity range corresponds to the [0-VC]% and [0-CD]% where the selected EMT yield accurate estimations.
- The threshold defines the volume concentration and equivalent crack density at which the ultrasonic values deviate from analytical EMT.

A. Section 1: Ultrasonic Measurements

1. Octahedrons vs. Ellipsoidal Cracks, AR 0.2, Calcite Filled and Dry Cases

In this section, the validity of using octahedrons cracks as alternative for ellipsoidal cracks is investigated.

The VTI fractured rock has a Barnet shale background embedded with calcite filled or dry inclusions. The ultrasonic simulations conditions are defined in Table 6 (Models 1 and 2) and the VTI cracks sets distribution parameters are defined in Table 7.

a. Calcite Filled Inclusions Case

The compressional wave velocity $V_{p,0}^{u}$ in the direction perpendicular to the fractures is computed for a fractured Barnet shale embedded with calcite filled ellipsoidal and octahedron cracks with AR = 0.2.

Refer to Model 1 in Table 6 to check different simulation conditions.

In this case, ultrasonic elastic properties cannot be compared to Hudson EMT method since calcite material does not validate the weak assumption of Hudson. Therefore, the computed ultrasonic velocity $V_{p,0}^{u}$ is compared to those obtained analytically using SCA and DEM (Figure 26).

The results for calcite filled inclusions show that cracks with ellipsoidal shape led to higher velocities estimations compared to those obtained using an octahedron shape. A linear fit is added to the octahedrons data points to compare with velocities obtained using ellipsoidal cracks at the same volume concentration and the two values are found to differ by an average of 12.5 m/s (calculated up to a VC of 8%).

The Ellipsoids are shown to give higher velocity estimations compared to EMT assumptions while octahedrons provide lower ones. The RMS errors listed in Table 8 show that both crack shapes provide $V_{p,0}^{u}$ velocity estimates that are highly compatible with SCA and DEM values. The validity is tested up to a CD of 14.08% (VC: 7.5%) for ellipsoidal cracks case and a CD of 12.44% (VC: 4.05%) for octahedrons cracks.

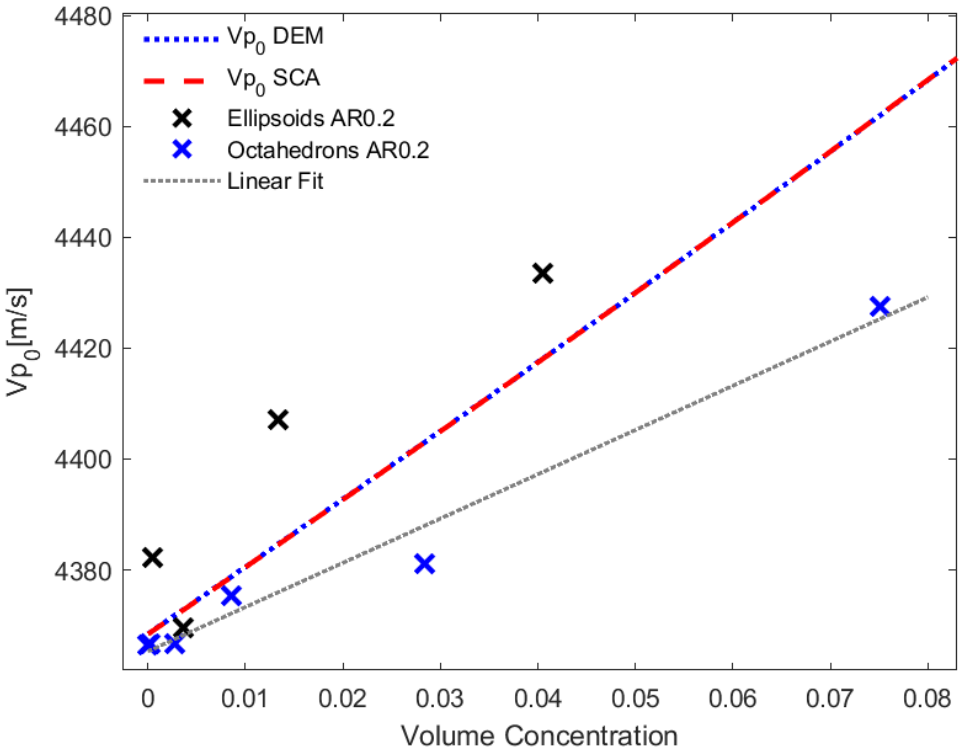

Figure 26 Comparison of computed ultrasonic compressional velocity $V_{p,0}^{u}$ with $f_c = 300$ kHz to estimated EMT values for Barnet shale fractured formation embedded with calcite filled inclusions (AR 0.2) modeled as ellipsoids and octahedrons

b. Dry Inclusions Case

The compressional wave velocity $V_{p,0}^{u}$ in the direction perpendicular to VTI fracture set is computed in this section for fractured Barnet shale formation embedded with dry ellipsoidal and octahedron cracks with AR of 0.2.

Refer to Model 2 in Table 6 to check different simulation conditions.

In the model, dry inclusions are modeled with void instead of using a strong weak material or air. This is due to mesh limitations in the model when the properties of air are used, yielding very high computational time.

The computed ultrasonic values for the compressional velocity $V_{p,0}^{u}$ are compared to those obtained analytically using SCA, DEM, (Hudson 1st) H1 and (Hudson 2nd) H2 models (Figure 27).

The results for dry inclusions modeled using void show that cracks with ellipsoidal shape lead to slightly lower velocities estimations compared to those obtained using octahedrons. A polynomial fit is added to the octahedrons data points in order to compare with velocities obtained using ellipsoidal cracks at the same volume concentration and the two values are found to differ by an average of 63 m/s (calculated up to a VC of 7.5% or CD: 14.08%) for octahedrons cracks and VC of 10.43% (CD: 12.44%) for Ellipsoidal cracks.

The RMS errors listed in Table 8 show that both shapes provide $V_{p,0}^{u}$ velocity estimates that follow the same trend for the H1 model but with very large RMS errors. H2 values show unrealistic estimations where velocity estimates increase as VC increases, therefore, H2 is not used for comparison.

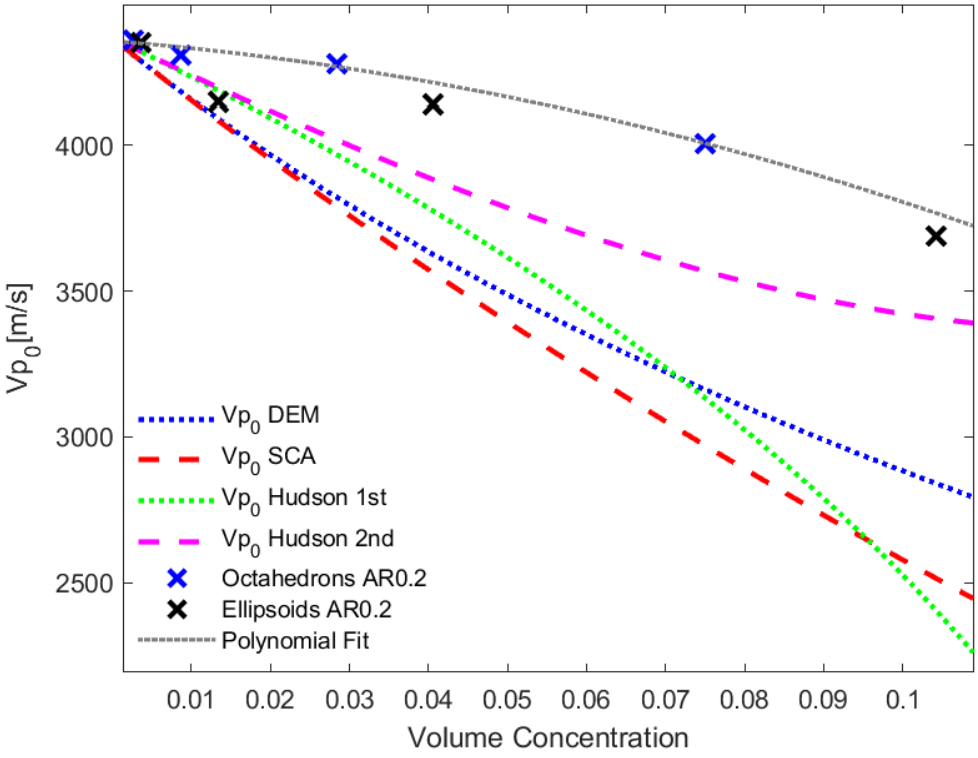

Figure 27 Comparison of computed ultrasonic compressional velocity $V_{p,0}^{u}$ with $f_c = 300$ kHz to estimated EMT values for Barnet shale fractured formation embedded with dry inclusions (AR 0.2) modeled as ellipsoids and octahedrons

Hudson 1 condition states that the wavelength must be large than the crack length, it seems that even if the validity applies (as in ellipsoids case) or does not (as in octahedrons case) at higher VC, both deviate at VC values above 1.34%.

Since EMT models rely on ellipsoidal cracks estimations, using irregular crack shape (octahedron) still provide accurate ultrasonic estimations. This is compatible with Grechka and Kachanov (2006a) findings where irregular shaped cracks are shown to provide similar results compared to cracks with regular shape up to 20% CD using a static loading for randomly distributed dry or liquid saturated cracks.

2. *Example 1: Octahedrons, AR 0.1, Calcite Filled Cases*

The compressional and shear wave velocities in the directions perpendicular ($V_{p,0}^{u}$,$V_{s,0}^{u}$) and parallel ($V_{p,90}^{u}$, $V_{s,90}^{u}$) to the VTI fracture set are computed in this section for fractured Barnet shale formation embedded with calcite octahedron cracks with AR of 0.1.

Refer to Models 3, 4, 5 and 6 in Table 6 to check different simulations conditions.

The computed ultrasonic values for $V_{p,0}^{u}$, $V_{p,90}^{u}$, $V_{s,0}^{u}$ and $V_{s,90}^{u}$ are compared to those obtained analytically using SCA and DEM methods as shown in Figure 28.

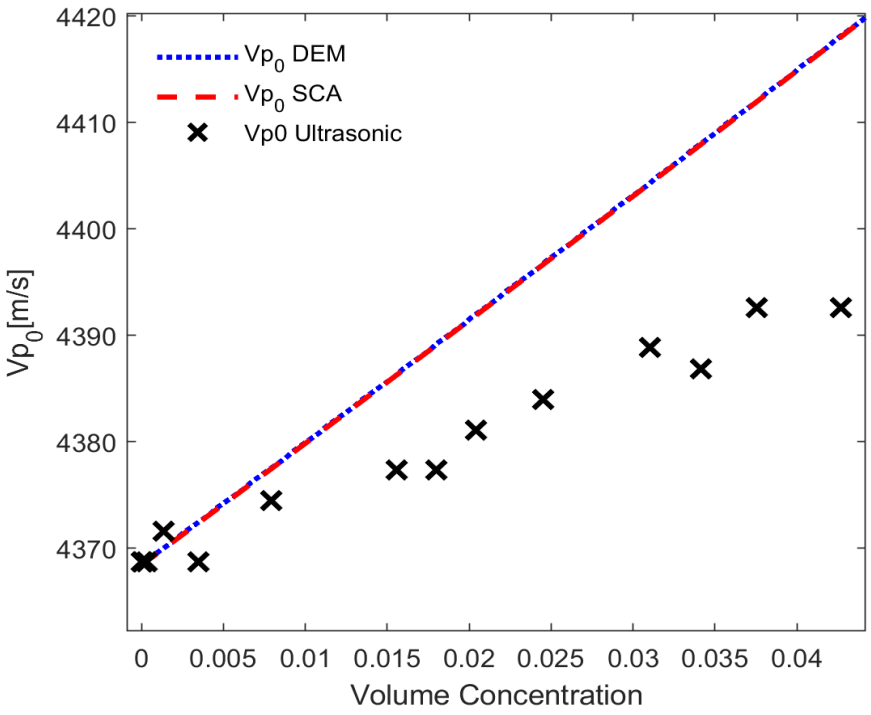

(a)

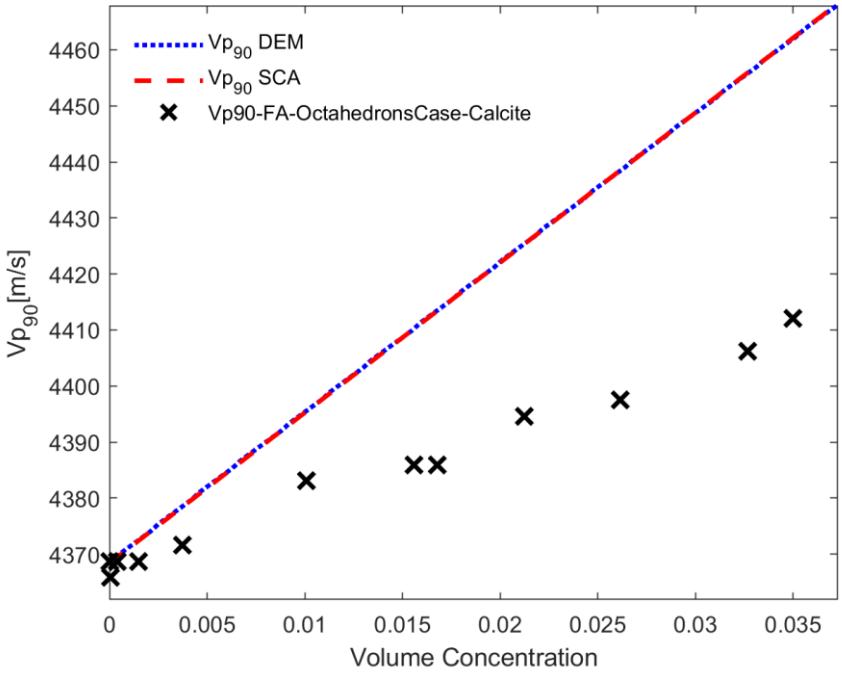
Vp90 DEM
Vp90 SCA
Vp90-FA-OctahedronsCase-Calcite
Vp90[m/s]
Volume Concentration
4460
4450
4440
4430
4420
4410
4400
4390
4380
4370
0
0.005
0.01
0.015
0.02
0.025
0.03
0.035

(b)

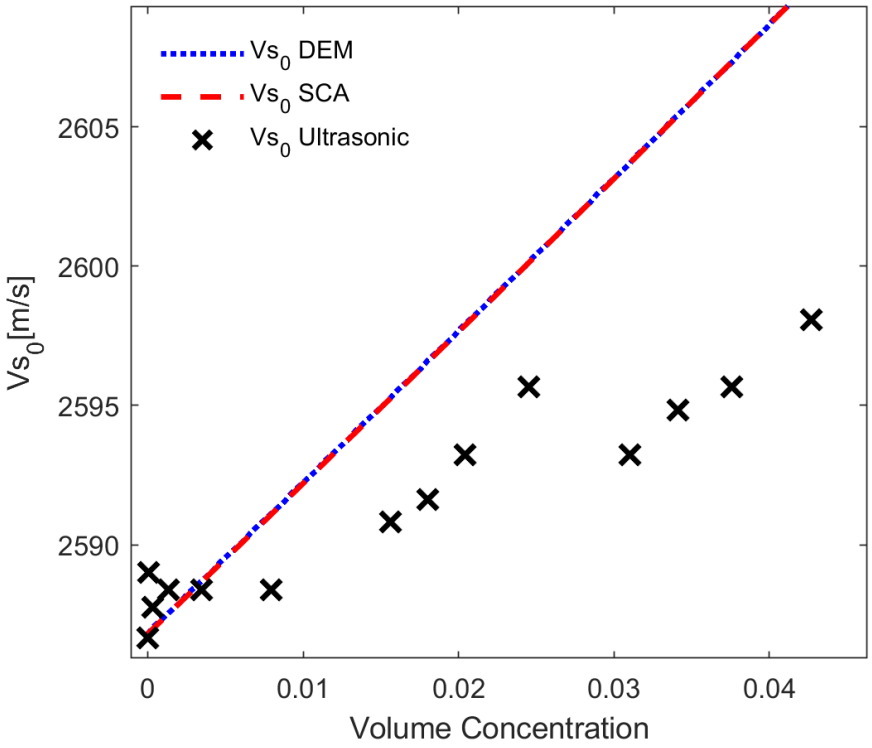
Vs0 DEM
Vs0 SCA
Vs0 Ultrasonic
Vs0[m/s]
Volume Concentration
2605
2600
2595
2590
0
0.01
0.02
0.03
0.04

(c)

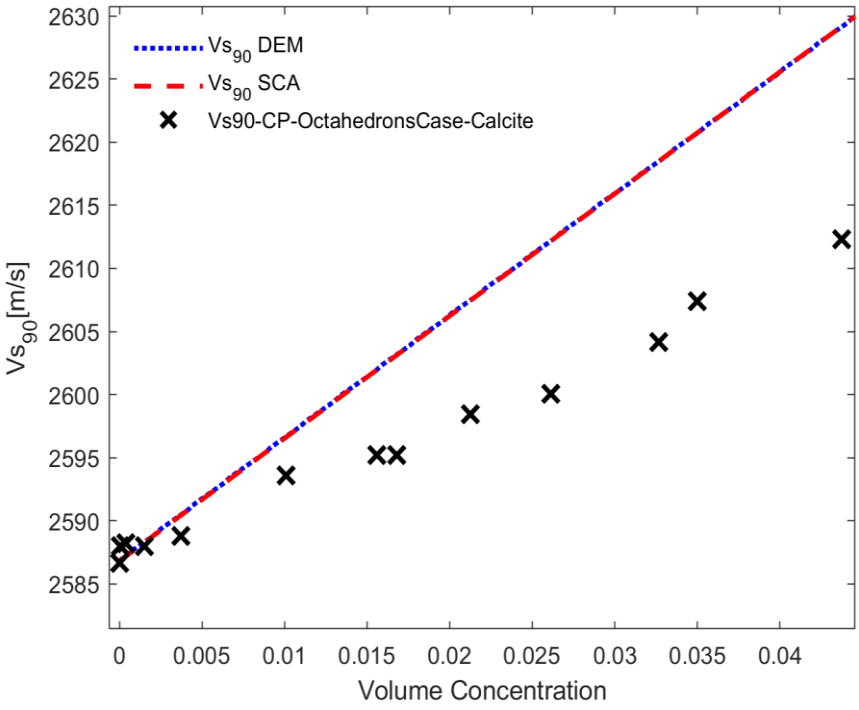

(d)

Figure 28 Comparison of computed ultrasonic compressional (a) $V^{u}_{p,0}$, (b) $V^{u}_{p,90}$ with $f_c = 300$ kHz and shear (c) $V^{u}_{s,0}$,(d) $V^{u}_{s,90}$ with $f_c = 500$ kHz velocities to estimated EMT values for Barnet shale fractured formation embedded with octahedrons calcite filled inclusions (AR 0.1)

The RMS values in Table 8 show that ultrasonic results fit well the SCA and DEM approximations for the whole VC studied range (up to 4.37%) equivalent to a CD range up to 16.4%. The RMS errors values for P-wave velocities (average RMS: 15.88 m/s) are higher than that of S-wave velocities (average RMS: 5.47 m/s). This might be related to the use of a higher central frequency when computing shear wave velocities (500 kHz) compared to that used when computed P-wave velocities (300 kHz) which led to a smaller shear wavelength compared to compressional wavelength. Therefore,

the resultant ratio $\boldsymbol{\delta_i}$ (Table 6) of the core length to wavelength is higher in the case of S-wave (19.33) than that of P-wave (6.87).

In addition, the velocities in the direction parallel to fracture set are shown to have higher RMS errors relative to EMT compared to those simulated perpendicular to the fracture set for both P-wave and S-wave velocities.

The computed velocities validate SCA and DEM assumptions for the whole studied range (up to CD of 16.4%). The deviation from the EMTs approximation increases as the VC increases and the threshold at which the deviation starts is around CD: 3.78% for all computed velocities including $V_{p,0}^{u}$, $V_{p,90}^{u}$, $V_{s,0}^{u}$ and $V_{s,90}^{u}$. Note that the computed velocities validate the EMTs for the whole CD region and this threshold only highlights the crack density value after which the values start to deviate without diverging from the ETM approximations.

Dahm and Becker (1998) showed that DEM better estimate numerical VTI fractured models with equal length cracks. Thus, SCA and DEM models can be used to estimate the crack density of calcite-filled fractures in Barnet shale formations up to 16.4% CD. This is important as calcite filled fractures play a major role in enhancing hydraulic fracturing treatment as explained in section II.C.b.

3. Example 2: Octahedrons, AR 0.1, Dry Case

The compressional wave velocity $V_{p,0}^{u}$ in the direction perpendicular to the VTI fracture set is computed in this section for fractured Barnet shale formation embedded with dry octahedron cracks modeled as void with AR of 0.1.

Refer to Model 7 in Table 6 to check different simulations conditions.

The computed ultrasonic values for $V_{p,0}^{u}$ are compared to those obtained analytically using SCA, DEM, H1 and H2 methods as shown in Figure 29.

The results are shown to give a large discrepancy compared to EMT analytical values. The RMS errors presented in Table 8 (Model 7) show that the lowest error corresponds to Hudson 1. Although the results are closer to H2 model, H2 predicts increasing moduli at high CD and thus cannot be considered as an accurate estimation. However, the RMS errors relative to H1 are very large (>100 m/s) and reflect on very small threshold (CD: 0.51% CD, VC: 0.14%) for Hudson 1 estimates to remain valid. Grechka and Kachanov (2006a) show that Hudson theory breaks when $gb \rightarrow 0$ for numerical 3D static modeling of randomly distributed dry cracks with maximum AR of 0.08. In our model, the background Vs,b /Vp,b velocity ratio calculated using Eq. 2 is gb = 0.27 for Barnet shale. This eliminates the possibility of the background material to be the main reason of discrepancies.

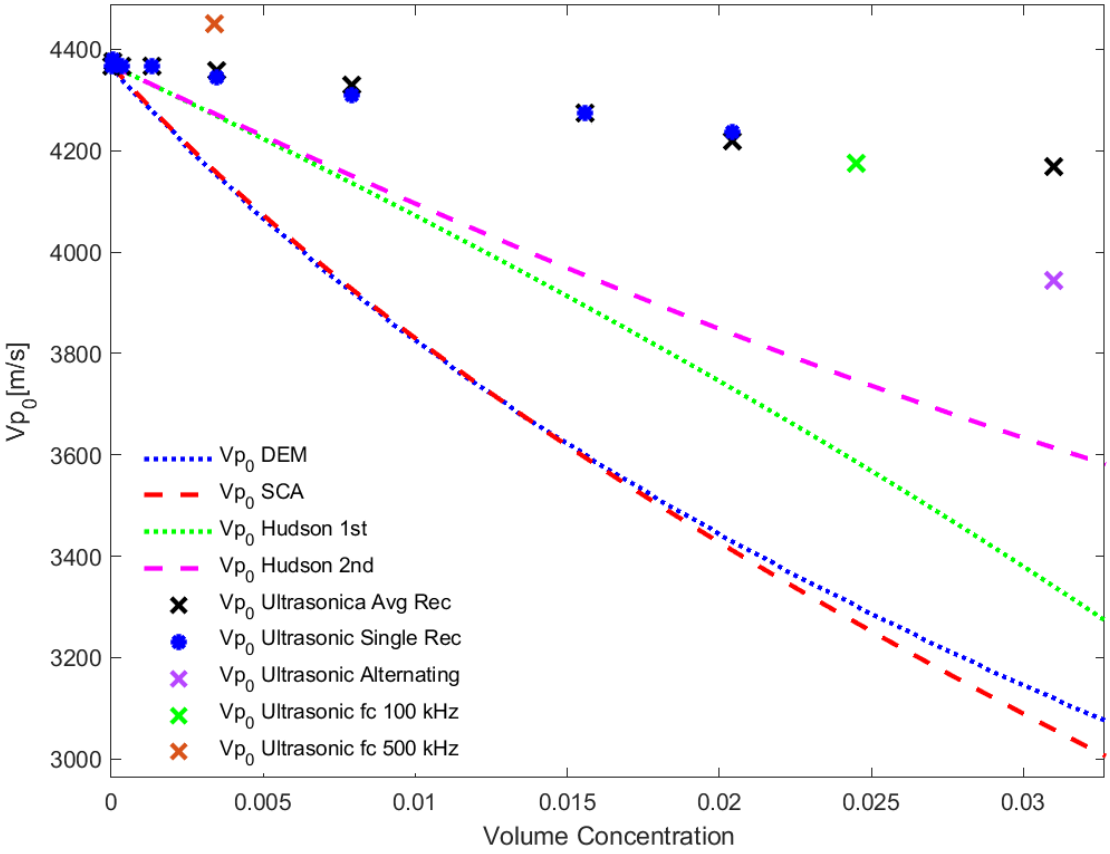

Figure 29 Comparison of computed ultrasonic compressional velocity $V_{p,0}^{u}$ with $f_c =$ 300 kHz to estimated EMT values for Barnet shale fractured formation embedded with dry inclusions modeled as octahedrons (AR 0.1)

Grechka and Kachanov (2006c) show that Hudson provides inferior estimations compared to other EMT models (LS and NIA) using numerical 3D static loading of randomly distributed dry cracks. The same authors support Hudson modeling for dry fractures up to 6% crack density using 3D numerical static modeling for fractured rock with AR 0.2 (Grechka et al., 2006) and up to 10% CD (Grechka & Kachanov, 2006a).

In addition, Saenger et al. (2004) show that 3D ultrasonic modeling for fractured media with very small AR (0.00025) and high central frequency (800 kHz) provides accurate SCA estimations up to a CD of 1% for P-wave and a CD of 3% for S-wave for

non-intersecting cracks. Saenger and Shapiro (2002) also support the use of SCA by ultrasonic modeling of 2D dry fractures resembling 3D VTI medium up to 30% crack density with a threshold of 10% CD. Both highlight the importance of crack interaction above this threshold.

Therefore, small thresholds for compressional velocity perpendicular to the fracture plane in fractured shale models embedded with dry cracks are documented in literature. The small threshold that we got might be acceptable. However, it is necessary to undergo a deeper investigation of the different numerical and geometrical parameters to know what is the main parameter behind the observed discrepancy (small threshold) with all EMT theories.

a. Effect of Single vs. Average Receiver Set

The velocity results are calculated by picking the arrival time of waveform obtained at a middle receiver (blue dots in Figure 29) and compared to those obtained by averaging 25 waveforms obtained at multiple receivers (black x in Figure 29). Single and Average cases give very similar results with an RMS error of 8.33 m/s.

b. Effect of Normalizing the Waveforms Amplitudes at Receivers

Normalizing the waveforms before picking the arrival time yields a small difference of 20 m/s.

c. Effect of using an Automated Time Step

The models are built following a sensitivity analysis to select accurate mesh and time step. An additional verification is performed by testing the use of an automated time step for a case with VC of 0.02%; ABQUS will automatically select a smaller time

step when needed. The effect is also not significant since the result only change by 18 m/s.

d. Effect of Crack Aspect Ratio: AR 0.2 vs. AR 0.1 vs. AR 0.05

Previous results obtained for an aspect ratio of 0.1 and 0.2 for fractured formation with dry fractures show similar discrepancies with EMT approximations. A smaller aspect ratio of 0.05 is tested in this section. The results of an octahedron cracks set with an AR of 0.05 is shown in Figure 30. The model with AR 0.05 represents VTI fractured Barnet formation with dry cracks modeled as void and have a VC of 5.89% (CD: 44%), the results are presented in Figure 31.

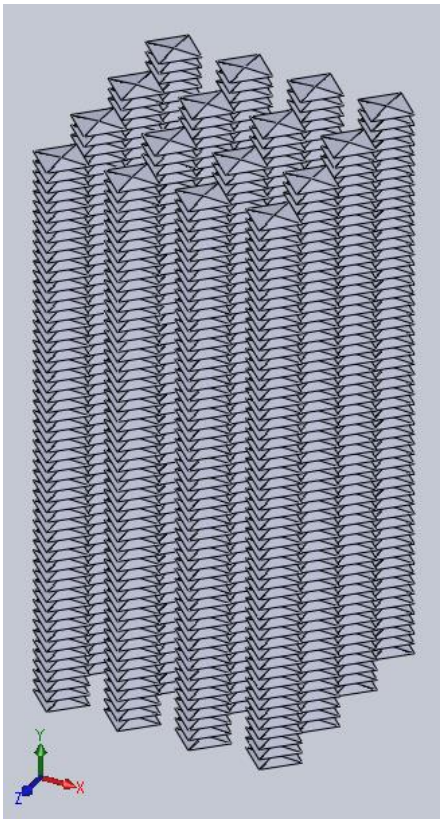

Figure 30 Set of octahedrons with AR 0.05. (CD: 44%) and (VC: 5.866%)

Results show that

- For AR 0.1, the relative difference with DEM at 3.1% VC (14.8% CD) is 1051.39 m/s.
- For AR 0.05, the relative difference with DEM at 5.8% VC (44% CD) is 2642 m/s.

Thus we conclude that using a samller AR is also showing large differnecs with EMTs; this elimiates the suggestion that AR is causing this discprency for the model studied.

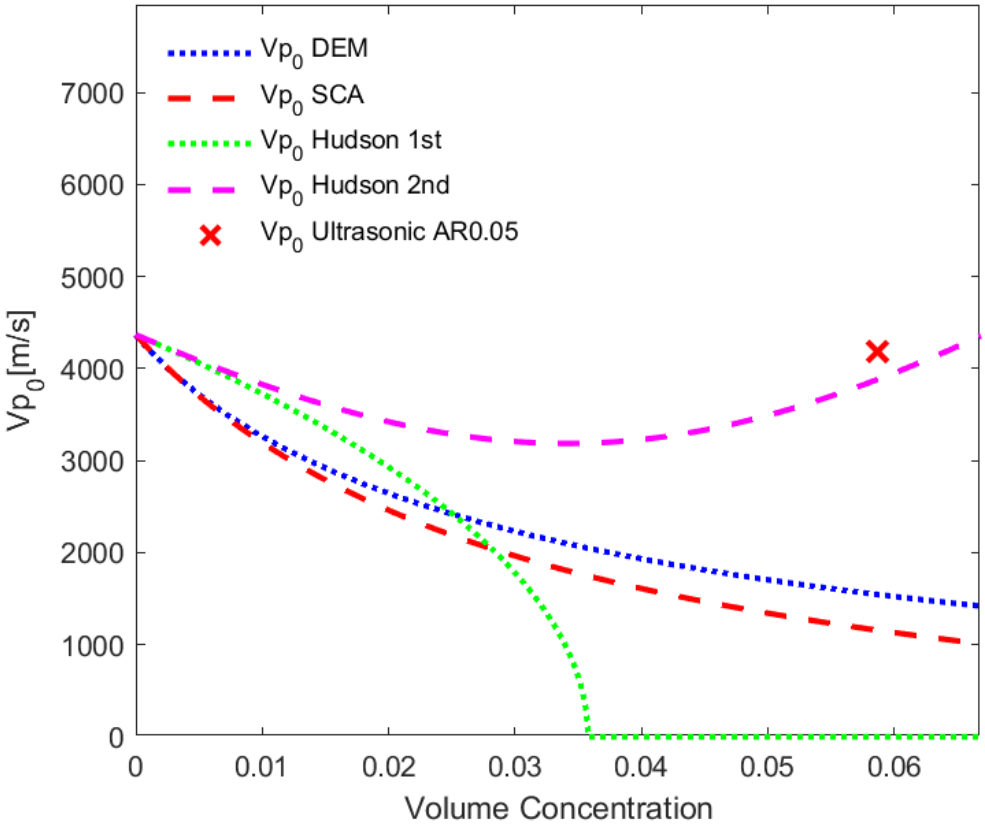

Figure 31 Effect of AR 0.05 on EMT validation for dry inclusions modeled with void and using a $f_c = 300$ kHz

Grechka and Kachanov (2006c) studied aspect ratio effect using numerical 3D static loading of randomly distributed dry cracks and show that smaller aspect ratio below about [0.1-0.15] will not affect the effective properties of dry fractures. The scale effect value is 20 for an AR of 0.1, 12.5 for AR 0.2 and 10 for AR 0.05 (Table 4). According to Saenger et al. (2006), using dynamic and static 2D modeling of fractured rock with randomly distributed dry parallel cracks, a scale value ≥ 20 is needed for the dynamic results to validate DEM estimations even at small crack densities for fractured rock with dry fractures. Therefore, the selection of an AR 0.1 is optimal.

e. Effect of Central Frequency

The central frequency used $f_c = 300$ kHz leads to a core edge length/wavelength ratio (δ_p) of 6.87. For $f_c = 500$ kHz and $f_c = 100$ kHz, δ_p=1.5 and δ_p= 7.49, respectively. For all the central frequencies tested, the wavelength is larger than crack length and larger than the distance between cracks which validates the Hudson's conditions. It was noticed that increasing the central frequency increases the value of ultrasonic computed velocity, which in return increases the gap between computed and analytical EMTs' results. This is investigated in subsequent sections since we expect that increasing the central frequency would decrease the computed velocity value and lead to a better comparison with EMT.

f. Alternating Model

We tested an alternating model where the cracks are sparsely distributed as shown in Figure 32. The simulation conditions are listed in Table 6 (Model 8) and the

octahedrons cracks parameters are listed in Table 7 (Model 8). Figure 29 shows that using an alternating crack model improved the result by 224 m/s.

In the alternating model (Figure 32), the contact fraction between the transmitted waveform and the cracks increases so that the ultrasonic effective values are more affected by the presence of fractures.

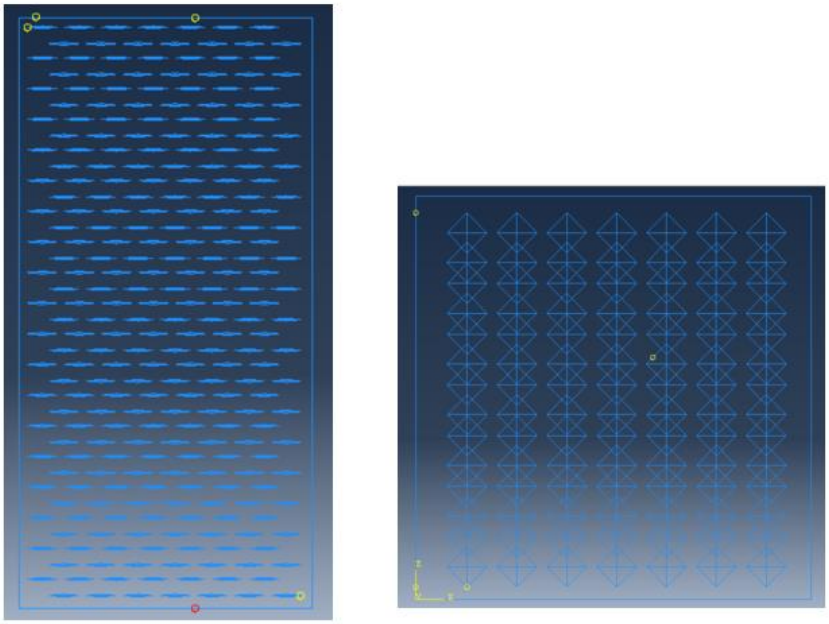

(a) **(b)**

Figure 32 (a) Side and (b) top views for suggested alternating model with Octahedrons cracks sparsely distributed for fractured Barnet shale formation with a VC (5.87 %) or CD (14.8%)

4. Example 3: Octahedrons, AR 0.1, Slow Filled Cases

The compressional and shear wave velocities in the directions perpendicular to the VTI fracture set are computed in this section for fractured Barnet shale formation

embedded with octahedron cracks filled with a slow elastic material (Table 2) with AR of 0.1.

Refer to Models 10 and 11 in Table 6 check different simulations conditions.

The computed ultrasonic values for $V_{p,0}^{u}$ and $V_{s,0}^{u}$ are compared to those obtained analytically using SCA, DEM, H1 and H2 methods as shown in Figure 33 (a) and Figure 34, respectively.

A slow material (weak material) is used in this model to fill the cracks and investigate the validity of the analytical EMT compared to the previous case where dry cracks were modeled as void.

a. Effect of Crack Density on Compressional Velocity, $V_{p,0}^{u}$

The effect of inclusion material (dry vs. slow) is compared in Figure 33 (c). The effect of AR 0.05 on ultrasonic compressional velocity $V_{p,0}^{u}$ is shown in (d) and compared to that for the dry inclusions case in (e).

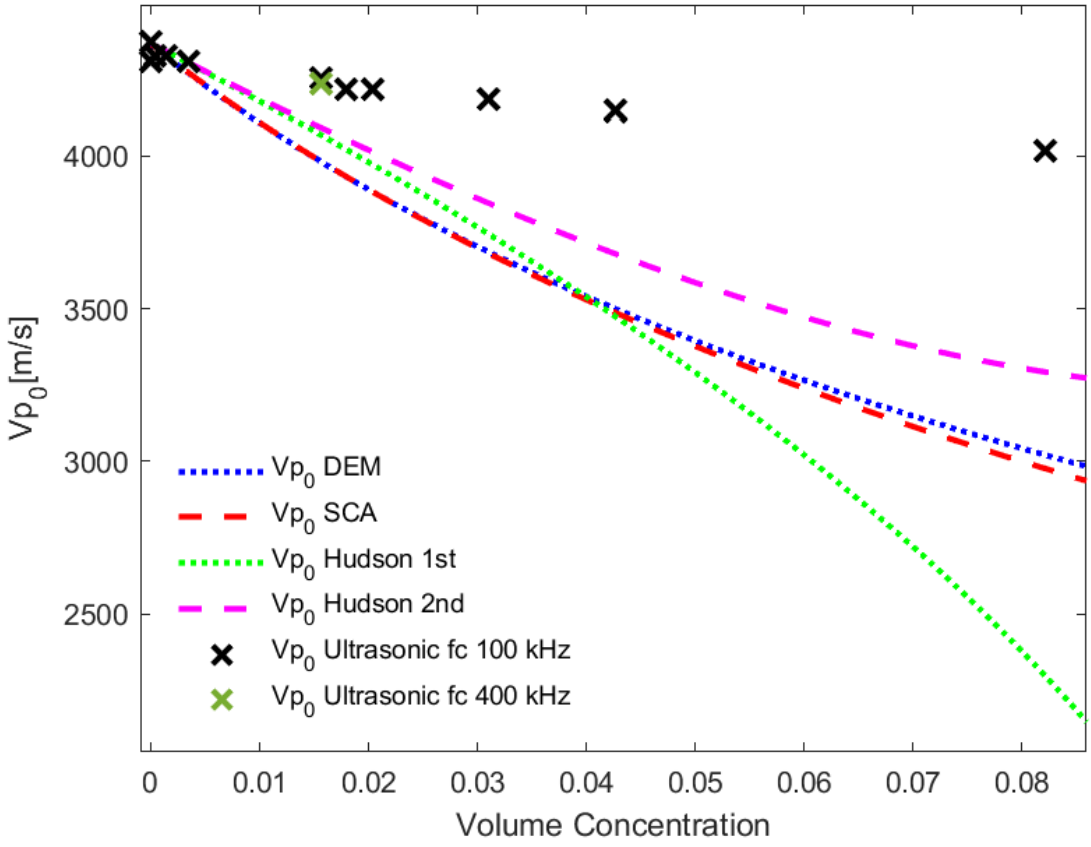
4000
3500
3000
2500
Vp0[m/s]
Vp0 DEM
Vp0 SCA
Vp0 Hudson 1st
Vp0 Hudson 2nd
Vp0 Ultrasonic fc 100 kHz
Vp0 Ultrasonic fc 400 kHz
0
0.01
0.02
0.03
0.04
0.05
0.06
0.07
0.08
Volume Concentration

(a)

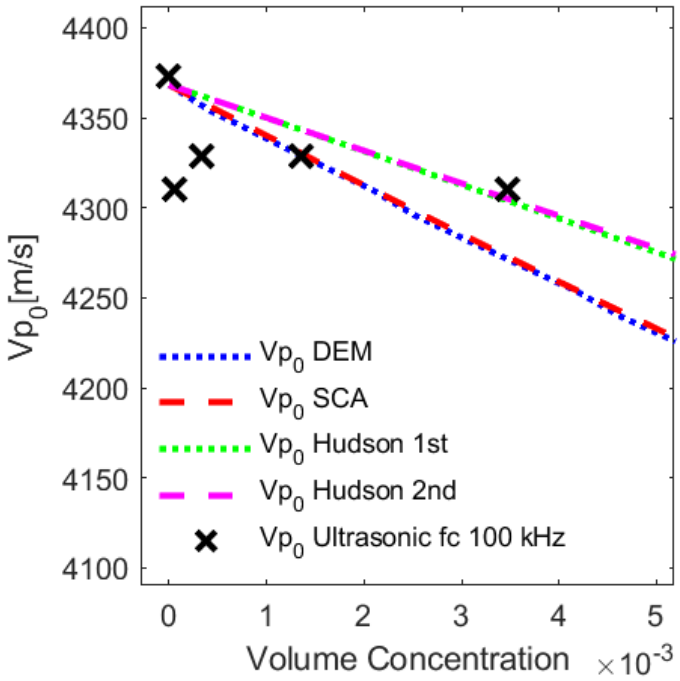
4400
4350
4300
4250
4200
4150
4100
Vp0[m/s]
Vp0 DEM
Vp0 SCA
Vp0 Hudson 1st
Vp0 Hudson 2nd
Vp0 Ultrasonic fc 100 kHz
0
1
2
3
4
5
Volume Concentration
×10-3

(b)

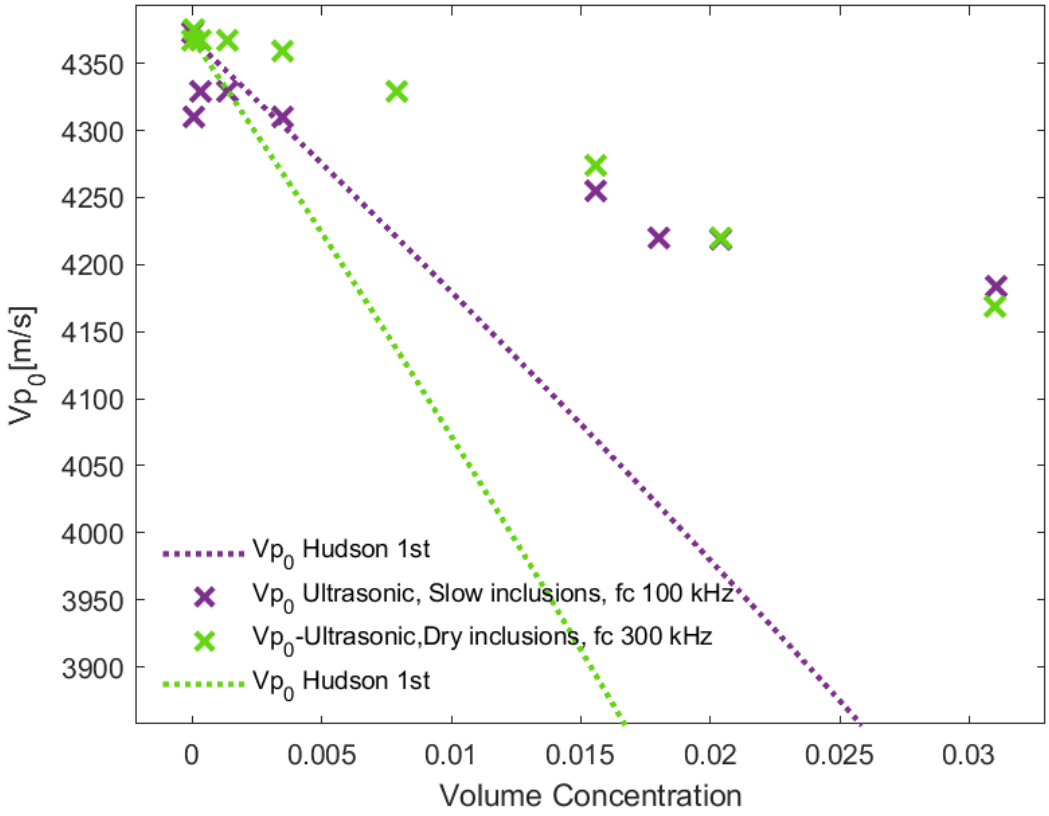
4350
4300
4250
4200
4150
4100
4050
4000
3950
3900
Vp0 [m/s]
Vp0 Hudson 1st
Vp0 Ultrasonic, Slow inclusions, fc 100 kHz
Vp0-Ultrasonic,Dry inclusions, fc 300 kHz
Vp0 Hudson 1st
0
0.005
0.01
0.015
0.02
0.025
0.03
Volume Concentration

(c)

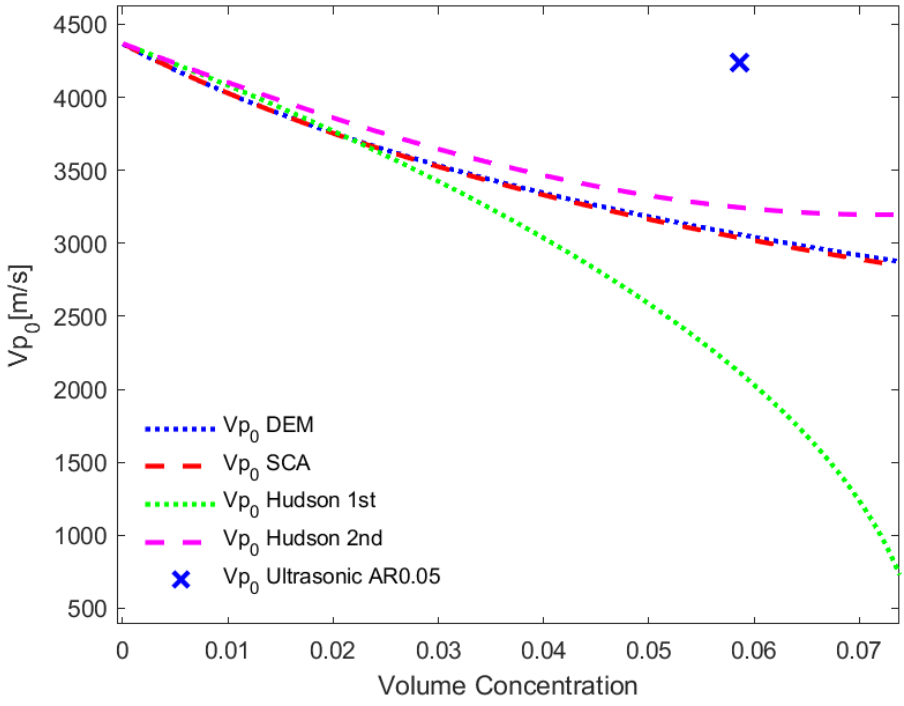
4500
4000
3500
3000
2500
2000
1500
1000
500
Vp0 [m/s]
Vp0 DEM
Vp0 SCA
Vp0 Hudson 1st
Vp0 Hudson 2nd
Vp0 Ultrasonic AR0.05
0
0.01
0.02
0.03
0.04
0.05
0.06
0.07
Volume Concentration

(d)

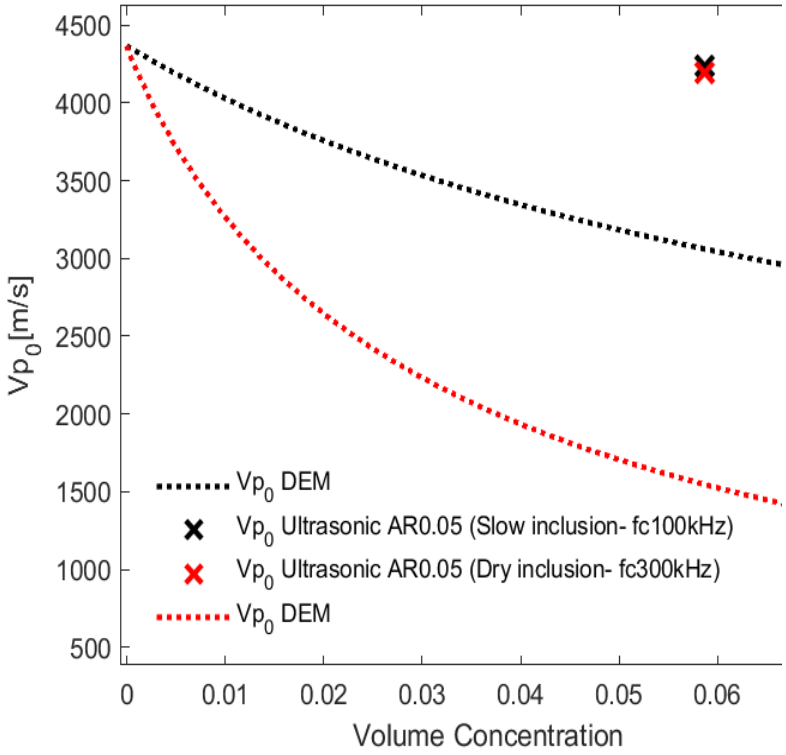

(e)

Figure 33 Comparison of computed ultrasonic compressional velocity (a) $V_{p,0}^{u}$ with $f_c = 100$ kHz to estimated EMT values for Barnet shale fractured formation embedded with slow (weak) octahedron inclusions (AR 0.1). (b) is a zoomed picture from (a). The effect of inclusion material for AR 0.1 (dry vs. slow) is compared in (c). The effect of AR 0.05 on ultrasonic compressional velocity $V_{p,0}^{u}$ is shown in (d) and compared to that for dry inclusions case in (e)

The results show a large discrepancy compared to EMTs analytical values (Figure 33 (a)). The RMS errors presented in Table 8 (Model 10) show that the lowest error corresponds to Hudson 1 (Figure 33 (b)). However, the RMS errors are very large (>100 m/s) similar to those obtained with the dry cracks in the previous section. Moreover, for CD> 0.35%, the velocities slightly decrease as the volume concentration

increases and follow a path similar to DEM and SCA but also with large RMS errors. Therefore, both models behave in a similar way for compressional velocity polarized perpendicular to the fracture plane. Additional parameters are investigated below to check on possible reasons behind this large deviation from EMTs.

Weak fracture models for the P-wave velocity has been tested in the literature. Shuai et al. (2020) performed ultrasonic experiments for 3D fractured VTI rocks embedded with a weak material and showed that P-wave velocities match better with the Hudson 1st order approximations up to crack density of 12%, with a small divergence that starts from CD of 2% while following the Hudson trend. Our results are also compatible with Ass' ad et al. (1993) who proved experimentally using seismic measurements on 3D fractured media for randomly distributed aligned cracks (AR 0.06) filled with rubber material that P-wave polarized velocities have a good agreement with Hudson only at low crack densities (1% and 3%) and yield a large divergence from the theory for higher crack densities.

i. Comparing Dry and Slow (weak) Cracks

It is interesting to notice that dry inclusions modeled with void or weak inclusions modeled with an elastic material give close results (similar trend) (Figure 33 (c)). Lower RMS are obtained for the weak material inclusion case with a slightly higher range of validity (larger threshold).

ii. Effect of Central Frequency

The current results are obtained with a central frequency value of 100 kHz. The effect of increasing the central frequency from 100 kHz to 400 kHz is studied. For simulation parameters of f_c= 400 kHz, refer to Model 13 in Table 6. The computed

compressional velocity decreases only by 18 m/s (Figure 33 (a)). The relative difference with Hudson 1st decreases only by 0.45%.

The effect of central frequency on the validity of Hudson theory is studied by J. Guo et al. (2018) using ultrasonic experiments on carbonate like 3D fractured rocks embedded with aligned fluid saturated fractures. His results showed that P-wave parallel greatly agreed with Hudosn 1st and 2nd at all frequencies up to 660 kHz and for all fracture thicknesses, however, P-wave perpendicular only agreed at high frequencies and divert at smaller frequencies after a small crack thickness.

Lowering the central frequncy of the source induces more energy dissipation in the matrix so that measured velocities show larger deviations from EMT approximations at smaller frequencies. This was examined by Shuai et al. (2020) using ultrasonic experiments for 3D VTI fractured medium with weak cracks.

Thus, a much higher central frequency (of 1000 kHz) must be tested to check if the computed ultrasonic $V_{p,0}^{u}$ results will be improved.

iii. Effect of AR 0.05

The effect of a small AR 0.05 (Table 6, Model 12) is shown in Figure 33 (c) and (d) where the ultrasonic result for $V_{p,0}^{u}$ shows a similar result for both dry and slow inclusions.

b. Effect of Crack Density on Shear Velocity, $V_{s,0}^{u}$

We study the effect of increasing the crack density on the shear wave velocity $V_{s,0}^{u}$ for inclusions filled with a slow material.

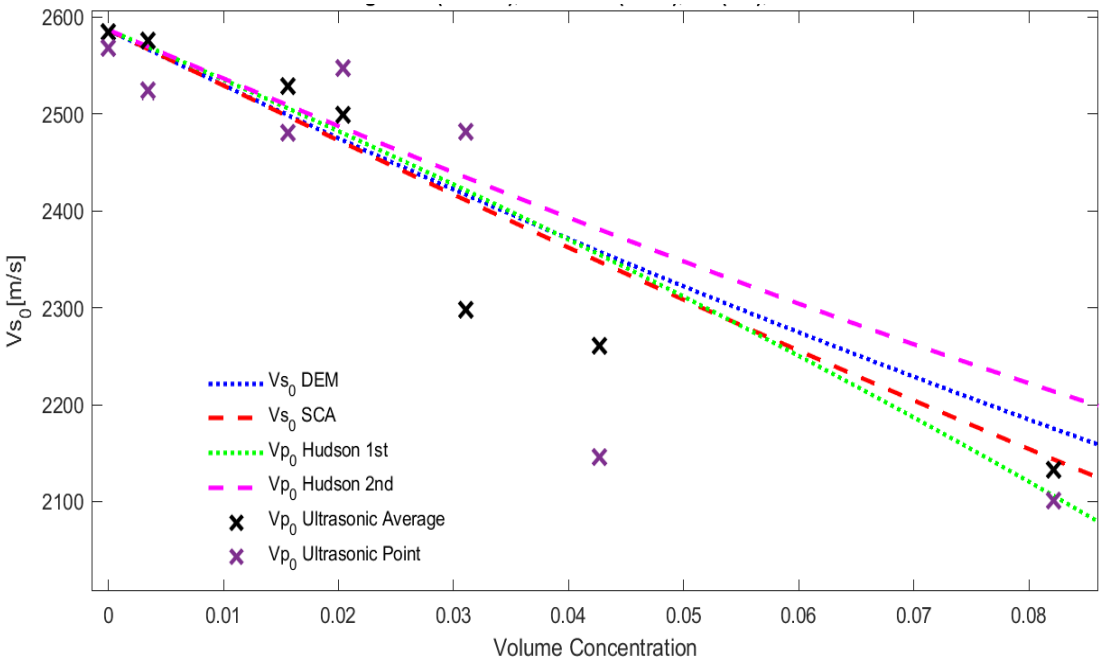

(a)

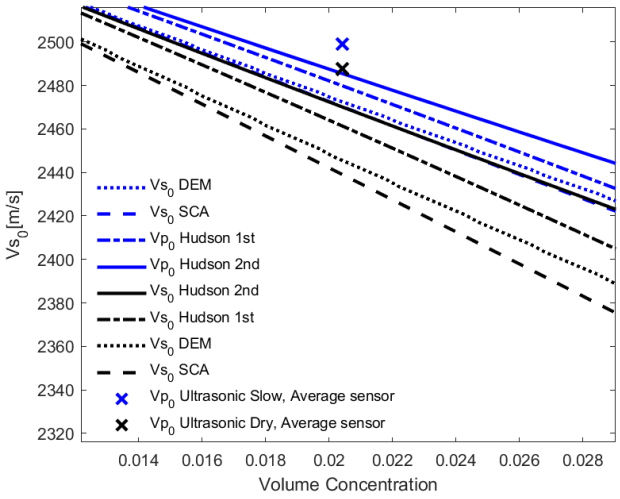

(b)

Figure 34 Comparison of computed ultrasonic shear velocity $V_{s,0}^{u}$ with f_c= 400 kHz to estimated EMTs' values for Barnet shale fractured formation embedded with slow inclusions. The effect of inclusion material (dry vs. slow) is compared in (b)

The shear wave ultrasonic computed velocities $V_{s,0}^{u}$ validates the Hudson theory (lowest RMS error) estimations for a VC up to 3.1% equivalent to CD up to 11.6%

(Figure 34 (a)). After this threshold, the computed $V_{s,0}^{u}$ velocity diverges. The ultrasonic $V_{s,0}^{u}$ computed by averaging the waveforms gives better estimations than picking the waveform only at the center receiver. However, at higher crack densities (CD: 30.8%, VC 8.2%), the computed velocity agrees with the SCA method when using average receivers and agrees with Hudson 1st when using a point sensor results. Therefore, the SCA can be used to provide estimations at higher crack densities (above 30.8%).

A lower threshold was proposed by Ass' ad et al. (1992) using seismic measurements on 3D fractured medium with weak cracks. He revealed that shear velocities polarized parallel to inclusions plane agree well with Hudson theories, however, shear velocities polarized perpendicular to the inclusions plane agree well with Hudson theories up to 7% and diverge at higher crack densities.

The use of SCA to estimate the shear effective elastic properties for fractured models is discussed in literature. Shuai et al. (2020) did ultrasonic experiments for 3D VTI fractured medium with weak cracks. He concluded that slow S-wave (perpendicular to fracture plane) velocities are closer to the anisotropic SCA and compliance-based NIA model up to 14% CD. In addition, Z. Guo and Li (2015) proved by using well log data for VTI Barnet shale formation that V_s is accurately predicted using the high frequency SCA model for three values of aspect ratio (0.01, 0.1 and 1) up to porosity of 2%.

J. Guo et al. (2018) related the central frequency to crack-crack interaction by calculating the ratio between S-wave wavelength to crack diameter. This is confirmed by in Figure 33 (c) where the major deviations are shown to occur after VC of 1% where the ratio is less than 5.

We computed $V_{s,0}^{u}$ at 2% VC (7.65% CD) for the dry model and compared it to the weak model. A good agreement with Hudson theory is obtained both for the dry and weak model (Figure 34). The RMS error at the CV tested is 20 m/s for the weak cracks case and 25 m/s for the dry cracks.

5. AR 0.1 vs. 0.2: Octahedrons, Calcite Filled and Dry Cases

Ultrasonic results obtained for $V_{p,0}^{u}$ are compared for aspect ratios of 0.1 and 0.2.

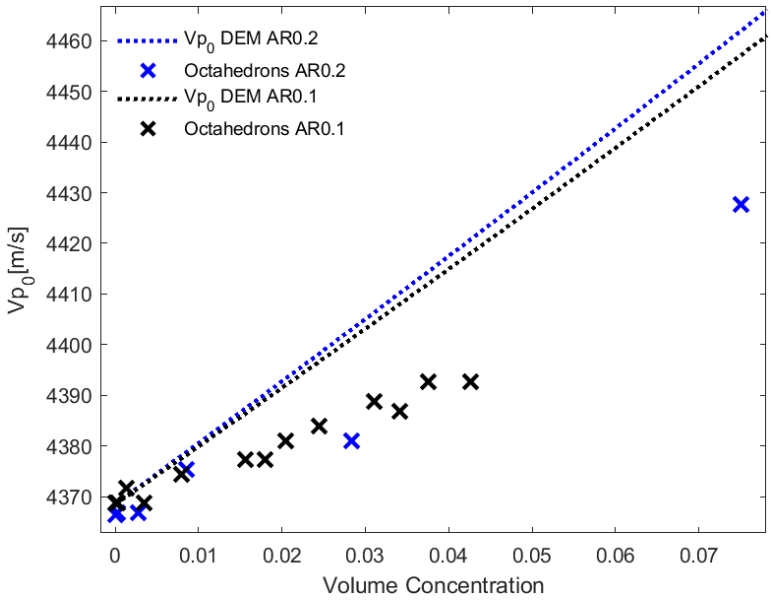

(a)

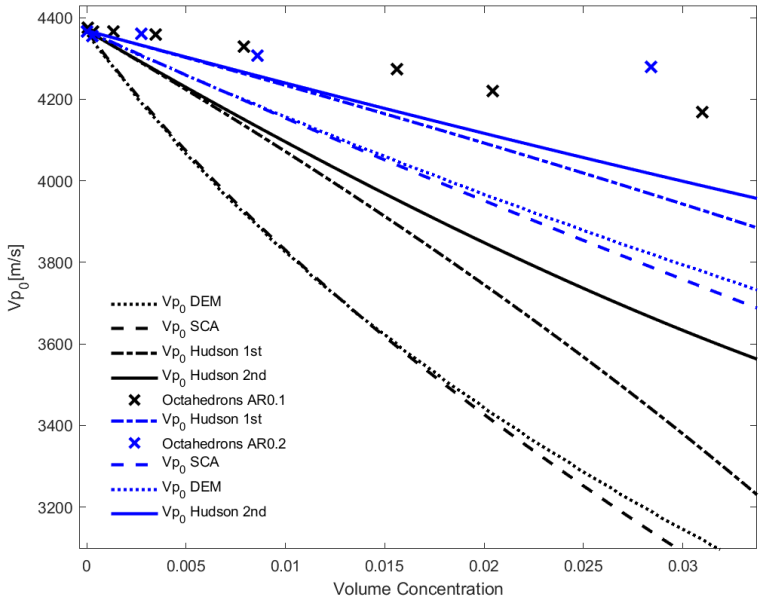

(b)

Figure 35 Comparing AR 0.1 to that of 0.2 for computed ultrasonic $V_{p,0}^{u}$ values for (a) calcite filled and (b) dry inclusions at f_c= 300 kHz

a. Calcite Case: AR 0.1 vs. 0.2– Octahedrons Cracks

AR 0.1 and 0.2 do not show major differences and both agree that Hudson leads the best approximation. The RMS error compared with H1 values is 10.26 m/s (excluding the last point) for AR 0.2 and 8.95 m/s for AR 0.1.

b. Dry Case: AR 0.1 vs 0.2 – Octahedrons Cracks

AR 0.1 and 0.2 show similar results for dry inclusions. The deviation of computed ultrasonic velocities from H1 is large with an average RMS of 184 m/s.

The negligible effect of AR on the effective properties was demonstrated by Grechka and Kachanov (2006a) who performed numerical 3D static modeling of randomly distributed dry cracks and show that the elastic properties are independent of AR ranging from 0.04 to 0.08. Grechka and Kachanov (2006a) also studied the aspect

ratio effect using numerical 3D static loading of randomly distributed dry cracks and show that smaller aspect ratio below about [0.1-0.15] will not affect the effective properties of dry fractures.

We concluded that AR was not the issue and that it is either the central frequency of the source or the distribution of cracks (regular or alternating) that mainly affect the EMT validity.

6. Conclusion on Ultrasonic Models with Dry and Weak Cracks

In sum, Barnet shale model embedded with cracks that are either dry or filled with a weak material will behave in a similar way both for P-wave and S-wave velocities perpendicular to the fracture plane. The P-wave ultrasonic velocities deviate from EMT at very small threshold compared to the S-wave threshold. The main reason for the discrepancy with EMT might be the source central frequency and its effect on crack-crack interaction. A higher central frequency (e.g., 1000 kHz) must be tested to finalize our conclusions.

Our results contradict with those given by Shuai et al. (2020) who performed ultrasonic experiments for 3D VTI fractured medium with weak cracks and stated that P-wave velocity resulted in better agreements with EMT compared to S-wave velocities. He related that to the ratio of wavelength to crack diameter of the P- wave which is larger (nearly two times) than that of the S- wave so that the long wavelength assumption is more satisfied for the P- wave. He also related the high divergence of S-wave velocity at low frequency to the fact that measurement frequencies lie in the Mie scattering regime for S2 wave. In our model, this ratio is 6 time larger for the P-wave

compared to the S- wave and still the results show better agreement with EMT for the S-wave velocity.

Future work will include comparison with parallel P-wave and S-wave velocities ($V^{u}_{s \text{ and } p,90}$) as it is shown from the literature to yield better agreements with EMT models compared to the perpendicular elastic properties.

B. Section 2: Borehole Measurements (Benchmark)

We simulate borehole acoustic (2D axisymmetric) and ultrasonic (2D) models to calculate the geomechanical properties of fractured (Example 1) and layered rocks (Example 2).

1. Example 1: Effect of Single Fracture Location on Ultrasonic and Borehole Compressional Velocity

Example 1 illustrates the applicability of the borehole 2D axisymmetric model in computing the effective elastic properties for fractured rocks. A Marcellus shale rock embedded with water filled horizontal fractures with material properties defined in Table 3 is used. Ultrasonic 2D measurements are compared to Borehole 2D axisymmetric measurements (Figure 36).

a. Model Geometry

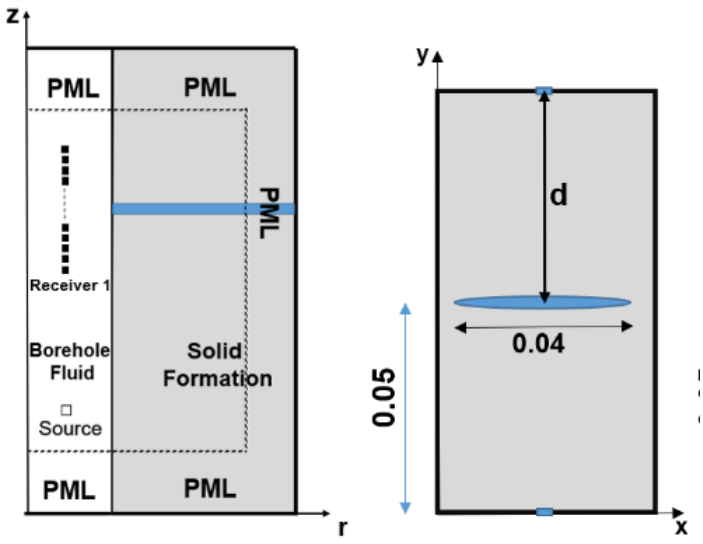

(a) **(b)**

Figure 36 (a) Borehole acoustic model with a horizontal fracture and (b) ultrasonic model with an elliptical fracture (Kareem, Khadijeh, & Maalouf, 2020)

b. Results

Figure 37 shows that the compressional velocity measured using ultrasonic measurement (V_p^u) is equal to the compressional velocity measured using borehole measurement (V_p^b) when the fracture is located at the center of the receiver array. Moreover, V_p^u does not depend on the fracture location in the core. Therefore, in a fractured medium, the location of horizontal fractures in a sample does not affect ultrasonic measurements but affects the borehole measurements.

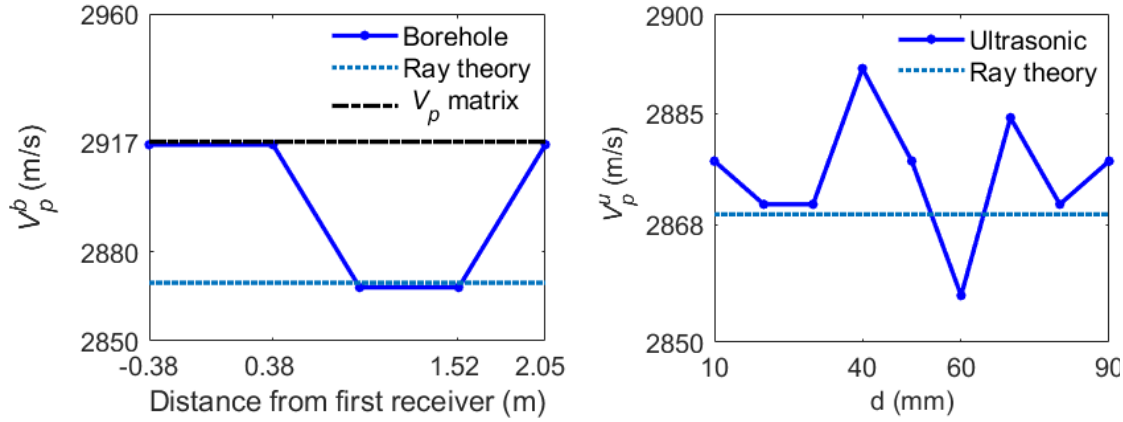

(a) **(b)**

Figure 37 (a) Compressional velocity simulated using borehole measurements (V_p^b) for various position of the fracture with respect to receiver 1 of the acoustic tool. (b) Compressional velocity simulated using ultrasonic measurements (V_p^u)(Kareem et al., 2020)

2. *Example 2: Effect of Fracture Layer Thickness in a VTI Medium on Ultrasonic and Borehole Compressional Velocity*

A periodically layered medium composed of two alternating isotropic fast layers: Layer 1 and Layer 2 (defined in Table 3) is considered to form a VTI medium. Figure 38 (a) describes the ultrasonic 3D layered rock with layers oriented at 0° and 90° degrees with respect to the horizontal x-axis; arrows indicate the directions of the wave propagation. The borehole model with multiple horizontal layers (VTI) is also shown in (Figure 38 (d)). The ultrasonic compressional and shear wave velocities $V_{p,0}^{u}$ and $V_{s,0}^{u}$ are obtained using a 2D model (Figure 38 (c)) while borehole velocities are obtained using a 2D axisymmetric model (Figure 38 (d)) excited with a monopole source.

a. <u>Model Geometry</u>

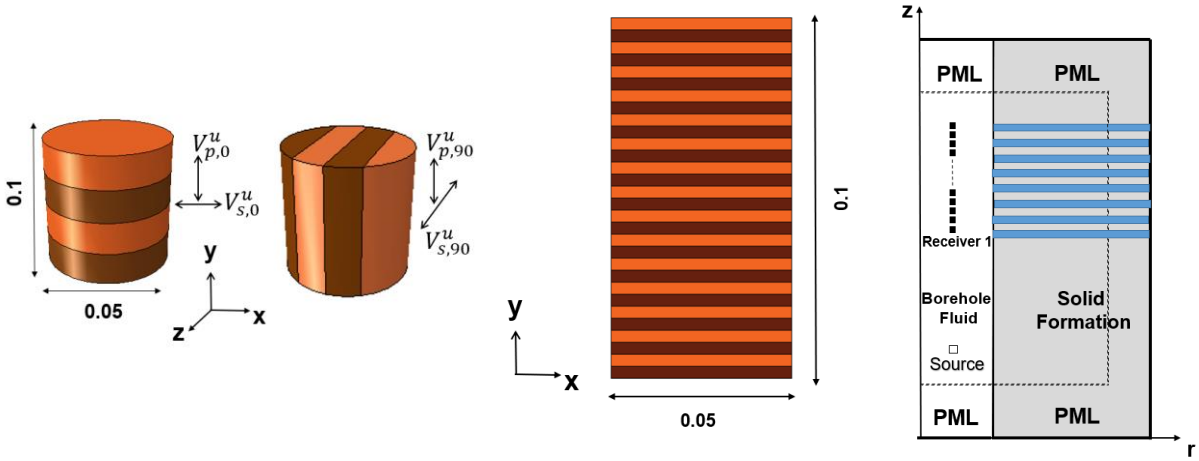

(a) **(b)** **(c)** **(d)**

Figure 38 Layered rock with (a) 0° and (b) 90° bedding planes. Black arrows indicate the direction of the wave propagation used for ultrasonic measurements. (c) 2D illustration of the core with horizontal layers. (d) Borehole 2D axisymmetric model with horizontal layers (VTI). Dimensions are in meter (Kareem et al., 2020)

b. Results

Figure 39 shows the c_{ij} obtained using ultrasonic and borehole measurements. We compare the measured dynamic elastic properties to the ones obtained by applying Backus average (Backus, 1962) (grey line) and the ones obtained using ray theory (RT) (red line) to Layers 1 and 2.

Figure 39 show that the dynamic elastic properties are obtained using RT (short wavelength approximation) for large thicknesses, and using the Backus average (long wavelength approximation) for small thicknesses (Marion et al., 1994; Liu and Schmitt, 2006). The transition from ray to effective medium theory occurs when the wavelength to layer thickness ratio (WTR) is 4<WTR<24 for the compressional mode, and 2<WTR<14 for the shear mode.

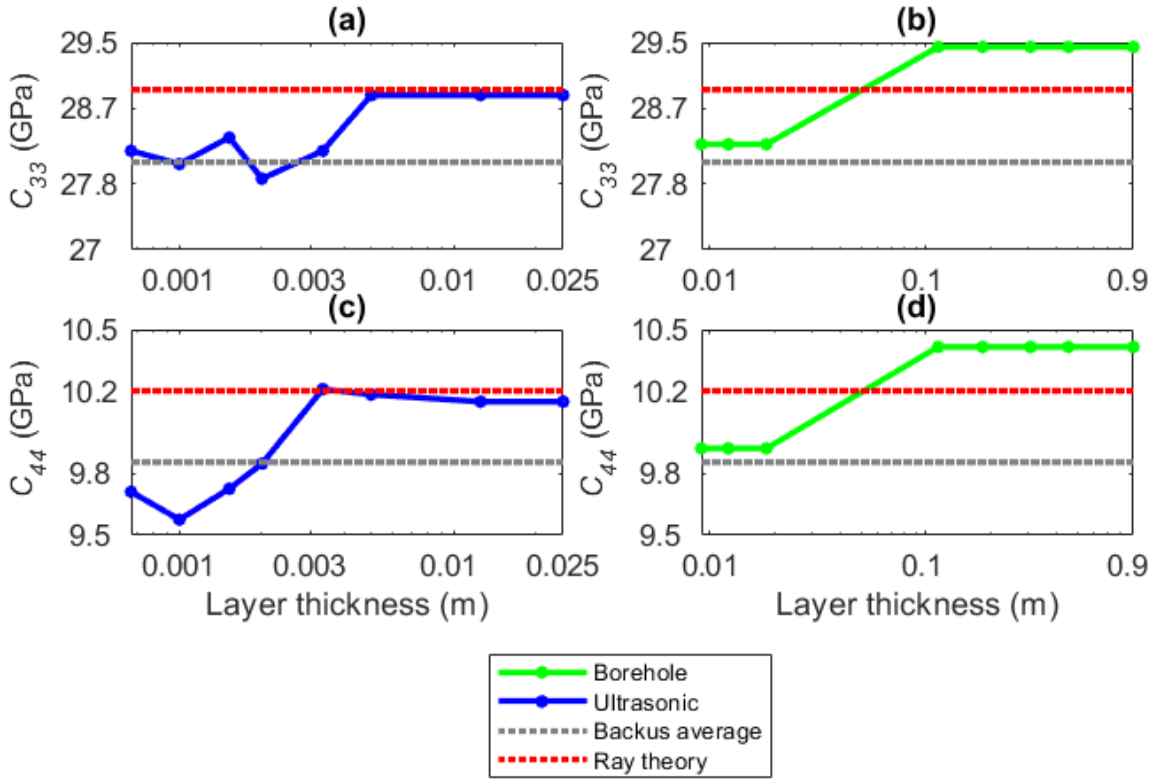

Figure 39 Stiffness coefficients of the layered formation of example 2 obtained using ultrasonic and borehole measurements (Kareem et al., 2020)

CHAPTER V

CONCLUSION

The range of applicability of different EMT models to estimate the dynamic elastic properties of fractured shale formations using the finite element method (FEM) is addressed. The elastic properties of the rock are calculated using ultrasonic measurements and are compared with three effective medium models: the Hudson 1st and 2nd orders, the self-consistent approximation (SCA) and the differential effective medium theory (DEM). The shale rock includes equidistant horizontal fractures modeled as ellipsoids and approximated as octahedrons. The fractured rock shows VTI symmetry and the fractures are either dry or filled with a calcite or a weak material, have an aspect ratio of 0.1 or 0.2 and a volume concentration that varies from 1% to 8% equivalent to a crack density up to 30%.

EMT models rely on ellipsoidal cracks estimations. However, ellipsoidal geometry is difficult to mesh in numerical simulations compared to other irregular shape such as octahedrons. We show that octahedrons can substitute ellipsoids in dynamic ultrasonic simulations. This enhances the simulation time and provide a better mesh quality.

Calcite filled fractures act as planes of weakness that can reactivate during hydraulic fracturing and provide a network of fractures connected to the wellbore. The effective compressional and shear wave velocities polarized parallel and perpendicular to the fracture plane of a fractured Barnet shale rock with calcite filled inclusions agree with the SCA and DEM theories up to a crack density of 16.4%. The S-wave velocities

are better approximated with EMTs compared to the P-wave velocities which might be related to using a higher central frequency for the source.

Barnet shale formations with dry filled fractures agree with Hudson 1st theory up to a very small crack density of 0.51%. Numerical modeling of dry fractures as void led to high RMS errors between ultrasonic and EMTs' values. The effects of picking the arrival time, using single or multiple sensors, normalizing the waveforms and using an automated time step are tested. Moreover, a smaller aspect ratio, higher central frequency and using alternating cracks are studied to evaluate the main cause of the discrepancy with EMT theories. The results are enhanced by 6.7% when the distribution of cracks was changed from regular to alternating.

Barnet shale formation with cracks filled with a slow material are modeled. The results using weak inclusions are similar to those obtained with the dry cracks. The shear wave velocity perpendicular to the fracture plane agrees well with Hudson theory up to a crack density of 11.6%. Above this threshold, the velocities diverge from Hudson estimates and agree with SCA at large crack densities of 30.8%. Crack-crack interactions cannot be neglected if the ratio is less than 5. In our case, for shear velocities computed at a central frequency of 400 kHz, this ratio decreases from 5.16 to 4.26 as crack density increases from 0 to 30.8% which indicates that crack-crack interactions are significant after a volume concentration of 1.56% or crack density of 5.8%.

The P-wave estimations deviate from EMTs at very small threshold compared to the S-wave threshold. The main reason might be related to the source central frequency and its effect on crack-crack interaction. A higher central frequency (e.g., [800-1000] kHz) must be tested to finalize our conclusions.

The applicability of the borehole measurements in identifying fractured and layered shale rocks and comparing them with ultrasonic simulations was manifested in the last section. For a Marcellus shale formation embedded with a water-filled fracture, the compressional velocity measured using ultrasonic measurement is shown to be equal to the compressional velocity measured using borehole measurement when the fracture is located at the center of the receiver array. A layered model composed of two alternating isotropic fast layers show that the dynamic elastic properties are obtained using RT (short wavelength approximation) for large thicknesses, and using the Backus average (long wavelength approximation) for small thicknesses.

We show that the finite element method in the time and frequency domains are stable and computationally efficient to model ultrasonic and borehole waves. Future work will investigate the effect of higher central frequencies, distance between cracks, fracture orientation and fracture distribution on the validity of EMTs. The models can be extended to cover the large scale well logging analysis and field data obtained using either small scale (ultrasonic) or large scale (well logging) will be used to verify our results and conclusions.

APPENDIX

Appendix A: Shape factor $\boldsymbol{Q_i}$

The geometric shape factor Q_i defined in Eq. 41 and Eq. 42 for a vertical transversely isotropic medium (VTI) embedded with spheroidal inclusions is given by

$$Q_i = [I + G_i C_{EM}(C_i - C_{EM})]^{-1}, \tag{44}$$

where

C_i: stiffness matrix of the inclusion phase,

I: Identity matrix $C_{EM} = C_{SCA}$ for SCA method and $C_{EM} = C_{DEM}$ for DEM method,

G_i: Fourth order rank tensor with coefficients given by (Eshelby, 1957; Mura, 1982) defined by

$$G_{ijkl} = \frac{1}{8\pi}[\bar{G}_{ikjl} + \bar{G}_{jkil}], \tag{45}$$

The non-zero coefficients of the G_{ijkl} matrix are given by (Mura, 1982)

$$\begin{aligned}
&\bar{G}_{1111} = \bar{G}_{2222} = \frac{\pi}{2}\int_0^1 \Delta(1-x^2)\{[f(1-x^2)+h\gamma^2x^2][(3e+d)(1-x^2)+4f\gamma^2x^2]-g^2\gamma^2x^2(1-x^2)\}dx,\\
&\bar{G}_{3333} = 4\pi\int_0^1 \Delta\gamma^2x^2[d(1-x^2)+f\gamma^2x^2][e(1-x^2)+f\gamma^2x^2]dx,\\
&\bar{G}_{1122} = \bar{G}_{2211} = \frac{\pi}{2}\int_0^1 \Delta(1-x^2)\{[f(1-x^2)+h\gamma^2x^2][(e+3d)(1-x^2)+4f\gamma^2x^2]-3g^2\gamma^2x^2(1-x^2)\}dx,\\
&\bar{G}_{1133} = \bar{G}_{2233} = 2\pi\int_0^1 \Delta\gamma^2x^2\{[(d+e)(1-x^2)+2f\gamma^2x^2][f(1-x^2)+h\gamma^2x^2]-g^2\gamma^2x^2(1-x^2)\}dx,\\
&\bar{G}_{3311} = \bar{G}_{3322} = 2\pi\int_0^1 \Delta(1-x^2)[d(1-x^2)+f\gamma^2x^2][e(1-x^2)+f\gamma^2x^2]dx,\\
&\bar{G}_{1122} = \frac{\pi}{2}\int_0^1 \Delta(1-x^2)\{g^2\gamma^2x^2-(d-e)[f(1-x^2)+h\gamma^2x^2]\}dx,\\
&\bar{G}_{1313} = \bar{G}_{2323} = -2\pi\int_0^1 \Delta g\gamma^2x^2(1-x^2)[e(1-x^2)+f\gamma^2x^2]dx,
\end{aligned} \tag{46}$$

where

$$\begin{cases} \Delta^{-1} = [e(1-x^2) + f\gamma^2x^2]\{[d(1-x^2) + f\gamma^2x^2][f(1-x^2) + h\gamma^2x^2] - g^2\gamma^2x^2(1-x^2)\}, \\ d = C_{11}, \\ e = (C_{11} - C_{12})/2, \\ f = C_{44}, \\ g = C_{13} + C_{44}, \\ h = C_{33}, \\ \gamma = \frac{\alpha_1}{\alpha_3}, \end{cases} \tag{47}$$

with

α_1: Semi-Major of the ellipsoid inclusion,

α_3: Semi-Minor of the ellipsoid inclusion.

The tensor **G** is therefore given in Kelvin's notation as

$$G_{ijkl} = \begin{bmatrix} G_{1111} & G_{1122} & G_{1133} & 0 & 0 & 0 \\ G_{1122} & G_{2222} & G_{1133} & 0 & 0 & 0 \\ G_{3311} & G_{3311} & G_{3333} & 0 & 0 & 0 \\ 0 & 0 & 0 & 2G_{1313} & 0 & 0 \\ 0 & 0 & 0 & 0 & 2G_{1313} & 0 \\ 0 & 0 & 0 & 0 & 0 & 2G_{1212} \end{bmatrix}, \tag{48}$$

REFERENCES

Abboud, N. N., Wojcik, G. L., Vaughan, D. K., Mould Jr, J., Powell, D. J., & Nikodym, L. (1998). *Finite element modeling for ultrasonic transducers.* Paper presented at the Medical Imaging 1998: Ultrasonic Transducer Engineering.

Andrews, D. (2014). Modelling of Ultrasonic Transducers and Ultrasonic Wave Propagation for Commercial Applications using Finite Elements with Experimental Visualization of Waves for Validation. *Proceedings of the 2014 COMSOL*.

Ass' Ad, J., McDonald, J., Tatham, R., & Kusky, T. (1996). Elastic wave propagation in a medium containing oriented inclusions with a changing aspect ratio: A physical model study. *Geophysical Journal International, 125*(1), 163-172.

Ass' ad, J., Tatham, R., McDonald, J., Kusky, T., & Jech, J. (1993). A physical model study of scattering of waves by aligned cracks: Comparison between experiment and theory 1. *Geophysical Prospecting, 41*(3), 323-339.

Ass' ad, J. M., Tatham, R. H., & McDonald, J. A. (1992). A physical model study of microcrack-induced anisotropy. *Geophysics, 57*(12), 1562-1570.

Backus, G. E. (1962). Long-wave elastic anisotropy produced by horizontal layering. *Journal of Geophysical Research, 67*(11), 4427-4440.

Bakulin, A., Grechka, V., & Tsvankin, I. (2000). Estimation of fracture parameters from reflection seismic data—Part I: HTI model due to a single fracture set. *Geophysics, 65*(6), 1788-1802.

Bandyopadhyay, K. (2009). *Seismic anisotropy: Geological causes and its implications to reservoir geophysics*: Stanford University.

Barati, R., & Liang, J. T. (2014). A review of fracturing fluid systems used for hydraulic fracturing of oil and gas wells. *Journal of Applied Polymer Science, 131*(16).

Barbosa, N. D., Caspari, E., Rubino, J. G., Greenwood, A., Baron, L., & Holliger, K. (2019). Estimation of fracture compliance from attenuation and velocity analysis of full-waveform sonic log data. *Journal of Geophysical Research: Solid Earth, 124*(3), 2738-2761.

Bayuk, I., Dubinya, N., Garagash, I., Tikhotskiy, S., & Tikhotskaya, O. (2019). *Multiscale rock-physics modeling of effective elastic properties of fractured reservoir rocks.* Paper presented at the 53rd US Rock Mechanics/Geomechanics Symposium.

Beran, M., & Molyneux, J. (1966). Use of classical variational principles to determine bounds for the effective bulk modulus in heterogeneous media. *Quarterly of Applied Mathematics, 24*(2), 107-118.

Berryman, J. G. (1980). Long-wavelength propagation in composite elastic media II. Ellipsoidal inclusions. *The Journal of the Acoustical Society of America, 68*(6), 1820-1831.

Berryman, J. G. (1992). Exact effective-stress rules in rock mechanics. *Physical review A, 46*(6), 3307.

Berryman, J. G. (1995). Mixture theories for rock properties. *Rock physics and phase relations: A handbook of physical constants, 3*, 205-228.

Boadu, F. K., & Long, L. T. (1996). Effects of fractures on seismic-wave velocity and attenuation. *Geophysical Journal International, 127*(1), 86-110.
Boak, J., & Kleinberg, R. (2020). Shale gas, tight oil, shale oil and hydraulic fracturing *Future Energy* (pp. 67-95): Elsevier.
Bristow, J. (1960). Microcracks, and the static and dynamic elastic constants of annealed and heavily cold-worked metals. *British Journal of Applied Physics, 11*(2), 81.
Bruggeman, V. D. (1935). Berechnung verschiedener physikalischer Konstanten von heterogenen Substanzen. I. Dielektrizitätskonstanten und Leitfähigkeiten der Mischkörper aus isotropen Substanzen. *Annalen der physik, 416*(7), 636-664.
Bu, A. (2016). Correlating Core Analysis and Well Logging: The Stezyca Oil and Gas Field. *Oil & Gas Research, 2*(2). doi:10.4172/2472-0518.1000113
Budiansky, B. (1965). On the elastic moduli of some heterogeneous materials. *Journal of the Mechanics and Physics of Solids, 13*(4), 223-227.
Budiansky, B., & O'connell, R. J. (1976). Elastic moduli of a cracked solid. *International journal of Solids and structures, 12*(2), 81-97.
Caspari, E., Barbosa, N., Novikov, M., Lisitsa, V., Hunziker, J., Quintal, B., . . . Holliger, K. (2019). *Seismic Attenuation Mechanisms in Fractured Fluid Saturated Media–Numerical and Field Examples.* Paper presented at the 81st EAGE Conference and Exhibition 2019 Workshop Programme.
Chen, X.-L., & Tang, X.-M. (2012). Numerical study on the characteristics of acoustic logging response in the fluid-filled borehole embedded in crack-porous medium. *Diqiu Wuli Xuebao, 55*(6), 2129-2140.
Chen, X.-L., Tang, X.-M., & Qian, Y.-P. (2014). Simulation of multipole acoustic logging in cracked porous formations. *Geophysics, 79*(1), D1-D10.
Cheng, C. (1993). Crack models for a transversely isotropic medium. *Journal of Geophysical Research: Solid Earth, 98*(B1), 675-684.
Cleary, M. P., Lee, S.-M., & Chen, I.-W. (1980). Self-consistent techniques for heterogeneous media. *Journal of the engineering mechanics division, 106*(5), 861-887.
Council, N. R. (1996). *Rock fractures and fluid flow: contemporary understanding and applications*: National Academies Press.
Crampin, S., & Zatsepin, S. V. (1997). Changes of strain before earthquakes: the possibility of routine monitoring of both long-term and short-term precursors. *Journal of Physics of the Earth, 45*(1), 41-66.
Dahm, T., & Becker, T. (1998). On the elastic and viscous properties of media containing strongly interacting in-plane cracks. *Pure and Applied Geophysics, 151*(1), 1-16.
Darling, T. (2005). *Well logging and formation evaluation*: Elsevier.
de la Puente, J., Dumbser, M., Käser, M., & Igel, H. (2008). Discontinuous Galerkin methods for wave propagation in poroelastic media. *Geophysics, 73*(5), T77-T97.
Ding, P., Wang, D., Di, G., & Li, X. (2019). Investigation of the effects of fracture orientation and saturation on the Vp/Vs ratio and their implications. *Rock Mechanics and Rock Engineering, 52*(9), 3293-3304.
Economides, M. J., & Nolte, K. G. (1989). *Reservoir stimulation* (Vol. 2): Prentice Hall Englewood Cliffs, NJ.

Ekstrom, M. P. (1996). *Dispersion estimation from borehole acoustic arrays using a modified matrix pencil algorithm.* Paper presented at the Conference Record of the Twenty-Ninth Asilomar Conference on Signals, Systems and Computers.
Eshelby, J. D. (1957). The determination of the elastic field of an ellipsoidal inclusion, and related problems. *Proceedings of the royal society of London. Series A. Mathematical and physical sciences, 241*(1226), 376-396.
Fei, W., Huiyuan, B., Jun, Y., & Yonghao, Z. (2016). Correlation of dynamic and static elastic parameters of rock. *Electron. J. Geotech. Eng, 21*, 1551-1560.
Fink, J. (2020). *Hydraulic fracturing chemicals and fluids technology*: Gulf Professional Publishing.
Fisher, M., Heinze, J., Harris, C., Davidson, B., Wright, C., & Dunn, K. (2004). *Optimizing horizontal completion techniques in the Barnett shale using microseismic fracture mapping.* Paper presented at the SPE Annual Technical Conference and Exhibition.
Frehner, M., & Schmalholz, S. M. (2010). Finite-element simulations of Stoneley guided-wave reflection and scattering at the tips of fluid-filled fractures. *Geophysics, 75*(2), T23-T36.
Gale, J. (2014). Natural Fractures in Shale Hydrocarbon Reservoirs. *AAPG Search and Discovery Article# 41487 (2014)*, 2013-2014.
Gale, J. F., Laubach, S. E., Olson, J. E., Eichhubl, P., & Fall, A. (2014). Natural fractures in shale: A review and new observations. *AAPG bulletin, 98*(11), 2165-2216.
Gale, J. F., Reed, R. M., & Holder, J. (2007). Natural fractures in the Barnett Shale and their importance for hydraulic fracture treatments. *AAPG bulletin, 91*(4), 603-622.
Glover, D. P. <THE SONIC OR ACOUSTIC LOG.PDF>. *Petrophysics MSc Course Notes*, 172 197.
Gottesman, T., & MA, B. (1980). Effective elastic moduli of cracked fiber composites.
Grechka, V. (2005). Penny-shaped fractures revisited. *Studia Geophysica et Geodaetica, 49*(3), 365-381.
Grechka, V., & Kachanov, M. (2006a). Effective elasticity of fractured rocks: A snapshot of the work in progress. *Geophysics, 71*(6), W45-W58.
Grechka, V., & Kachanov, M. (2006b). Effective elasticity of rocks with closely spaced and intersecting cracks. *Geophysics, 71*(3), D85-D91.
Grechka, V., & Kachanov, M. (2006c). Seismic characterization of multiple fracture sets: Does orthotropy suffice? *Geophysics, 71*(3), D93-D105.
Grechka, V., Vasconcelos, I., & Kachanov, M. (2006). The influence of crack shape on the effective elasticity of fractured rocks. *Geophysics, 71*(5), D153-D160.
Grenon, M., & Hadjigeorgiou, J. (2012). Applications of fracture system models (FSM) in mining and civil rock engineering design. *International Journal of Mining, Reclamation and Environment, 26*(1), 55-73.
Guo, J., Han, T., Fu, L. Y., Xu, D., & Fang, X. (2019). Effective elastic properties of rocks with transversely isotropic background permeated by aligned penny-shaped cracks. *Journal of Geophysical Research: Solid Earth, 124*(1), 400-424.
Guo, J., Shuai, D., Wei, J., Ding, P., & Gurevich, B. (2018). P-wave dispersion and attenuation due to scattering by aligned fluid saturated fractures with finite thickness: Theory and experiment. *Geophysical Journal International, 215*(3), 2114-2133.

Guo, Z., & Li, X.-Y. (2015). Rock physics model-based prediction of shear wave velocity in the Barnett Shale formation. *Journal of Geophysics and Engineering, 12*(3), 527-534.
Guo, Z., Li, X.-Y., Liu, C., Feng, X., & Shen, Y. (2013). A shale rock physics model for analysis of brittleness index, mineralogy and porosity in the Barnett Shale. *Journal of Geophysics and Engineering, 10*(2), 025006.
Heagy, L. J. (2018). *Electromagnetic methods for imaging subsurface injections.* University of British Columbia.
Hill, R. (1965). A self-consistent mechanics of composite materials. *Journal of the Mechanics and Physics of Solids, 13*(4), 213-222.
Hoenig, A. (1979). Elastic moduli of a non-randomly cracked body. *International Journal of Solids and Structures, 15*(2), 137-154.
Hornby, B. E., Schwartz, L. M., & Hudson, J. A. (1994). Anisotropic effective-medium modeling of the elastic properties of shales. *Geophysics, 59*(10), 1570-1583.
Hu, Y., & McMechan, G. A. (2010). Theoretical Elastic Stiffness Tensor at High Crack Density. *Journal of Seismic Exploration, 19*(1), 43-68.
Hudson, J. (1980). *Overall properties of a cracked solid.* Paper presented at the Mathematical Proceedings of the Cambridge Philosophical Society.
Hudson, J. A. (1981). Wave speeds and attenuation of elastic waves in material containing cracks. *Geophysical Journal International, 64*(1), 133-150.
Hudson, J. A., & Liu, E. (1999). Effective elastic properties of heavily faulted structures. *Geophysics, 64*(2), 479-485.
Jakobsen, M., Hudson, J. A., & Johansen, T. A. (2003). T-matrix approach to shale acoustics. *Geophysical Journal International, 154*(2), 533-558.
Jakobsen, M., Hudson, J. A., Minshull, T. A., & Singh, S. C. (2000). Elastic properties of hydrate-bearing sediments using effective medium theory. *Journal of Geophysical Research: Solid Earth, 105*(B1), 561-577.
Kachanov, M. (1980). Continuum model of medium with cracks. *Journal of the engineering mechanics division, 106*(5), 1039-1051.
Kachanov, M. (1992). Effective elastic properties of cracked solids: critical review of some basic concepts.
Kachanov, M., Tsukrov, I., & Shafiro, B. (1994). Effective moduli of solids with cavities of various shapes.
Kachanov, M. L., Shafiro, B., & Tsukrov, I. (2003). *Handbook of elasticity solutions*: Springer Science & Business Media.
Kareem, H., Khadijeh, M., & Maalouf, E. (2020). *Comparison of the Elastic Properties of Rocks Obtained Using Static, Borehole Acoustic, and Ultrasonic Measurements.* Paper presented at the 54th US Rock Mechanics/Geomechanics Symposium.
Kawahara, J., & Yamashita, T. (1992). Scattering of elastic waves by a fracture zone containing randomly distributed cracks. *Pure and Applied Geophysics, 139*(1), 121-144.
Kinoshita, N., & Mura, T. (1971). Elastic fields of inclusions in anisotropic media. *Physica status solidi (a), 5*(3), 759-768.
Kröner, E. (1958). Berechnung der elastischen Konstanten des Vielkristalls aus den Konstanten des Einkristalls. *Zeitschrift für Physik, 151*(4), 504-518.

Kumar, D. (2013). Applying Backus averaging for deriving seismic anisotropy of a long-wavelength equivalent medium from well-log data. *Journal of Geophysics and Engineering, 10*(5), 055001.
Kuster, G. T., & Toksöz, M. N. (1974). Velocity and attenuation of seismic waves in two-phase media: Part I. Theoretical formulations. *Geophysics, 39*(5), 587-606.
Laws, N., & Brockenbrough, J. (1987). The effect of micro-crack systems on the loss of stiffness of brittle solids. *International Journal of Solids and Structures, 23*(9), 1247-1268.
Li, A., Ding, W., Luo, K., Xiao, Z., Wang, R., Yin, S., . . . He, J. (2020). Application of R/S analysis in fracture identification of shale reservoir of the Lower Cambrian Niutitang Formation in northern Guizhou Province, South China. *Geological Journal, 55*(5), 4008-4020.
Li, T., Wang, Z., Gu, Y. J., Wang, R., & Wang, Y. (2019). Experimental study of fracture structure effects on acoustic logging data using a synthetic borehole model. *Journal of Petroleum Science and Engineering, 183*, 106433.
Liu, J., Yao, Y., Liu, D., & Elsworth, D. (2017). Experimental evaluation of CO2 enhanced recovery of adsorbed-gas from shale. *International Journal of Coal Geology, 179*, 211-218.
Maalouf, E., & Torres-Verdín, C. (2018). Interpretation of borehole flexural measurements in high-angle wells using 3D spatial sensitivity functions. *Geophysics, 83*(6), D217-D229.
Matuszyk, P., Demkowicz, L., & Torres-Verdín, C. (2012). Solution of coupled acoustic–elastic wave propagation problems with anelastic attenuation using automatic hp-adaptivity. *Computer Methods in Applied Mechanics and Engineering, 213*, 299-313.
Matuszyk, P. J., & Demkowicz, L. F. (2014). Solution of coupled poroelastic/acoustic/elastic wave propagation problems using automatic hp-adaptivity. *Computer Methods in Applied Mechanics and Engineering, 281*, 54-80.
Matuszyk, P. J., Torres-Verdín, C., & Pardo, D. (2013). Frequency-domain finite-element simulations of 2D sonic wireline borehole measurements acquired in fractured and thinly bedded formations. *Geophysics, 78*(4), D193-D207.
Mavko, G., Mukerji, T., & Dvorkin, J. (2020). *The rock physics handbook*: Cambridge university press.
Mohamed, A. K., & Kashlaf, A. (2016). Comparative study between well logging and core analysis of Hawaz reservoir in Murzuq Basin, Libya. *Egyptian Journal of Basic and Applied Sciences, 3*(3), 301-313.
Mukerji, T., Berryman, J., Mavko, G., & Berge, P. (1995). Differential effective medium modeling of rock elastic moduli with critical porosity constraints. *Geophysical Research Letters, 22*(5), 555-558.
Mura, T. (1982). *Micromechanics of defects in solids*: Springer Science & Business Media.
Mura, T. (2013). *Micromechanics of defects in solids*: Springer Science & Business Media.
Norris, A. N. (1985). A differential scheme for the effective moduli of composites. *Mechanics of materials, 4*(1), 1-16.
O'Connell, R. J., & Budiansky, B. (1974). Seismic velocities in dry and saturated cracked solids. *Journal of geophysical Research, 79*(35), 5412-5426.

O'Connell, R. J., & Budiansky, B. (1977). Viscoelastic properties of fluid-saturated cracked solids. *Journal of Geophysical Research, 82*(36), 5719-5735.
OILMAN. (2018). 10 Best Performing Tips for Successful Hydraulic Fracturing. *OILMAN MAGAZINE*.
Papazis, P. K. (2005). *Petrographic characterization of the Barnett Shale, Fort Worth Basin, Texas.* University of Texas at Austin.
Pérez, M. A., Grechka, V., & Michelena, R. J. (1999). Fracture detection in a carbonate reservoir using a variety of seismic methods. *Geophysics, 64*(4), 1266-1276.
Saenger, E. H., Gold, N., & Shapiro, S. A. (2000). Modeling the propagation of elastic waves using a modified finite-difference grid. *Wave motion, 31*(1), 77-92.
Saenger, E. H., Krüger, O. S., & Shapiro, S. A. (2004). Effective elastic properties of randomly fractured soils: 3D numerical experiments. *Geophysical Prospecting, 52*(3), 183-195.
Saenger, E. H., Krüger, O. S., & Shapiro, S. A. (2006). Effective elastic properties of fractured rocks: Dynamic vs. static considerations *SEG Technical Program Expanded Abstracts 2006* (pp. 1948-1952): Society of Exploration Geophysicists.
Saenger, E. H., & Shapiro, S. A. (2002). Effective velocities in fractured media: a numerical study using the rotated staggered finite-difference grid. *Geophysical Prospecting, 50*(2), 183-194.
Sarout, J., Cazes, E., Delle Piane, C., Arena, A., & Esteban, L. (2017). Stress-dependent permeability and wave dispersion in tight cracked rocks: Experimental validation of simple effective medium models. *Journal of Geophysical Research: Solid Earth, 122*(8), 6180-6201.
Sayar, P. M. (2015). *Development of effective medium models for quantification of elastic properties and modeling of velocity dispersion of saturated rocks.*
Schlumberger, t. o. LOGGING-WHILE-DRILLING SONICVISION* TOOL. *Division of Marine and Large Programs.Lamont-Doherty Earth Observatory.Columbia University*.
Schoenberg, M. (1980). Elastic wave behavior across linear slip interfaces. *The Journal of the Acoustical Society of America, 68*(5), 1516-1521.
Sevostianov, I., & Kachanov, M. (1999). Compliance tensors of ellipsoidal inclusions. *International Journal of Fracture, 96*(1), 3-7.
Shafiro, B., & Kachanov, M. (1997). Materials with fluid-filled pores of various shapes: effective elastic properties and fluid pressure polarization. *International Journal of Solids and Structures, 34*(27), 3517-3540.
Shuai, D., Wei, J., Di, B., Guo, J., Li, D., Gong, F., & Stovas, A. (2020). Experimental study of crack density influence on the accuracy of effective medium theory. *Geophysical Journal International, 220*(1), 352-369.
Smith, M. B., & Montgomery, C. (2015). *Hydraulic fracturing*: Crc Press.
Sowards, J. W., McCowan, C. N., & Drexler, E. S. (2012). Interpretation and significance of reverse chevron-shaped markings on fracture surfaces of API X100 pipeline steels. *Materials Science and Engineering: A, 551*, 140-148.
Tang, H., Killough, J. E., Heidari, Z., & Sun, Z. (2017). A new technique to characterize fracture density by use of neutron porosity logs enhanced by electrically transported contrast agents. *SPE Journal, 22*(04), 1034-1045.
Tang, X.-M., & Cheng, C. H. A. (2004). *Quantitative borehole acoustic methods* (Vol. 24): Elsevier.

Te Wu, T. (1966). The effect of inclusion shape on the elastic moduli of a two-phase material. *International Journal of Solids and Structures, 2*(1), 1-8.
Thomas W. Engler. <Sonic Logs Notes.pdf>. *PET 370 course*.
Tutuncu, A., & Sharma, M. (1992). *Relating static and ultrasonic laboratory measurements to acoustic log measurements in tight gas sands.* Paper presented at the SPE Annual Technical Conference and Exhibition.
Ubani, C., Adeboye, Y., & Oriji, A. (2012). ADVANCES IN CORING AND CORE ANALYSIS FOR RESERVOIR FORMATION EVALUATION. *Petroleum & Coal, 54*(1).
Van Pamel, A., Sha, G., Rokhlin, S., & Lowe, M. (2017). Finite-element modelling of elastic wave propagation and scattering within heterogeneous media. *Proceedings of the Royal Society A: Mathematical, Physical and Engineering Sciences, 473*(2197), 20160738.
Wang, B., Kuo, Z., Guo, T., He, L., & Zhang, X.-L. (2018). Acoustic reflection well logging modeling using the frequency-domain finite-element method with a hybrid PML. *Applied Geophysics, 15*(1), 35-45.
Warpinski, N., Kramm, R. C., Heinze, J. R., & Waltman, C. K. (2005). *Comparison of single-and dual-array microseismic mapping techniques in the Barnett shale.* Paper presented at the SPE Annual Technical Conference and Exhibition.
Warpinski, N., & Teufel, L. (1987). Influence of geologic discontinuities on hydraulic fracture propagation (includes associated papers 17011 and 17074). *Journal of Petroleum Technology, 39*(02), 209-220.
Williams, G., & Sharma, M. (1991). *Quantification of Log-Core Correlation Using the Formation Microscope.* Paper presented at the SPE Annual Technical Conference and Exhibition.
Wyllie, M. R. J., Gregory, A. R., & Gardner, L. W. (1956). Elastic wave velocities in heterogeneous and porous media. *Geophysics, 21*(1), 41-70.
Zeng, L., Lyu, W., Li, J., Zhu, L., Weng, J., Yue, F., & Zu, K. (2016). Natural fractures and their influence on shale gas enrichment in Sichuan Basin, China. *Journal of Natural Gas Science and Engineering, 30*, 1-9.
Zhang, H., Lin, W., & Wang, X. (2011). *Numerical Studies on the Acoustic Field Generated by a Dipole Source in Noncircular Pipes.* Paper presented at the AIP Conference Proceedings.
Zimmerman, R. (1984). *Elastic moduli of a solid with spherical pores: new self-consistent method.* Paper presented at the International Journal of Rock Mechanics and Mining Sciences & Geomechanics Abstracts.
Zimmerman, R. W. (1990). Compressibility of sandstones.
Zoback, M. D. (2010). *Reservoir geomechanics*: Cambridge University Press.